PREFACE

It is our pleasure to introduce the first issue of Eurasian Journal of Science Engineering and Technology (EJSET) which is a scientific journal publication of Kazakh Culture and Education, Application and Research Center (http://ohu.edu.tr/kazak) established at Niğde Ömer Halisdemir University (NOHU) in the scope of collaboration between Niğde Ömer Halisdemir University (NOHU), Niğde, Turkey and L.N. Gumilyov Eurasian National University (ENU), Nur-Sultan (Astana), Kazakhstan.

EJSET is a highly-selective journal, covering topics that appeal to a broad readership of various branches of engineering, science and related fields. EJSET as a publication specifically aims to contribute to scientific development and solidarity of Turkic World and provides a platform for scientists and engineers throughout the world to present the up-to-date research findings and ideas in the areas of Science, Engineering, and Technology.

Papers reporting original research or extended versions of already published conference papers are all welcome. Papers for publication are selected through peer review to ensure originality, relevance, and readability. For scientists and engineers involved in research to publish high quality and refereed papers are also included. The journal ensures a wide indexing policy to make published papers highly visible to the scientific community.

EJSET has many benefits all geared toward strengthening research skills and advancing academic careers. Journal publications are a vital part of academic career advancement. We help our authors in advance engineering research in different branches like Computer Science, Electronics & Communication, Electrical Engineering, Mechanical Engineering and Information Technology etc. and in science and technology fields by providing world-class information and innovative tools and knowledge that help them make critical decisions, enhance productivity and improve outcomes.

Engineering, science and technology are fields where lot of research and study is required. The EJSET primarily focuses on providing a platform to the researchers of various engineering, science and technology stream where high level of teaching and learning is required. Self-created theories, researches; practical/theoretical works, applications based on reports/studies are welcomed in order to add contribution to the better understanding of technical, engineering and science challenges.

The first issue of the journal is planned to be an important cornerstone to serve these goals and will continue to move forward confidently. In the first year of our journal, we would like to thank our friends, engineers, scientists, academicians and technicians who showed interest in the subject, all the teams and referees as well as editorial board who supported the publication process.

In our second year, we will continue to walk towards with greater goals. We hope to meet you in our next issues…

Prof. Dr. Murat Barut (NOHU)

Associate Prof. Dr. Recep Zan (NOHU)

DESIGN AND REAL-TIME IMPLEMENTATION OF EXTENDED EMF BASED POSITION-SENSORLESS DRIVE FOR SURFACE MOUNTED PERMANENT MAGNET SYNCHRONOUS MACHINES

Murat BARUT [1],* iD, Sung-Yoon JUNG [2] iD, Chris MI [3] iD

[1,] *Department of Electrical & Electronics Engineering, Faculty of Engineering, Nigde Omer Halisdemir University, 51240, Nigde, Turkey*
[2,] *Honeywell Aerospace, Torrance, CA 90504, USA*
[3] *The U. S. Department of Energy (DOE)'s Graduate Automotive Technology Education (GATE) Center for Electric Drive Transportation, San Diego State University, San Diego, CA 92182, USA*

ABSTRACT

This paper introduces position-sensorless speed control of surface mounted permanent magnet synchronous motors (SPMSMs) based on an extended electromotive force (EMF) and specifically focuses on performances at very low and medium speeds. According to Authors' best knowledge, Morimoto's extended EMF approach is firstly applied to SPMSM and its low speed operation is evaluated by computer simulations and real-time experiments in the scope of this paper. To show that Morimoto's extended EMF technique is suitable to SPMSMs, computer simulations are executed in MATLAB® Simulink. Later, real-time experiments are performed to confirm the effectiveness of the proposed position-sensorless control system embedded on dSPACE-DS1104 controller with the SPMSM of 0.0262 Vrms/rpm. The resulting performance reveals that the possible speed estimation and thus position-sensorless control can be realized down to 1.4286% of the rated speed.

Keywords: PMSM, Position estimation, Speed estimation, Sensorless control, Extended electromotive force

1. INTRODUCTION

Nowadays permanent magnet alternating current synchronous motors (PMSMs) becomes very good option due to their reduced weight and volume causing higher power density and higher efficiency at both low and high speed operations, while the competition between different types of electrical machines is still aggressive. Considering these noticeable advantages, PMSMs get more attractive [1, 2] in variable speed drive applications consisting of hybrid electric vehicles (HEV) and electrical vehicles (EVs), industrial apparatus, renewable power generation, and home appliances in order to recover energy and space.

Further, high performance control of PMSMs calls for an accurate knowledge of rotor mechanical position and speed. However, the use of electromechanical sensors such as resolvers, optical encoders, and hall-effect sensors for this purpose increases the cost, size, weight, and hardware wiring complexity together with reducing the drive reliability and mechanical robustness [3]. Thus, position-sensorless solutions are required to discard these sensors.

In the literature, the great efforts are shown for designing position-sensorless control of PMSMs and these remarkable methods are summarized as follows [3-12]:

i)   Extended EMF based methods or Back electromotive force (back-EMF).
ii)   State observers utilizing deterministic or stochastic models of PMSM.
iii) The methods using high-frequency (HF) signal injection.

Mostly, the HF signal injection based methods present a stable estimation performance at very low and zero speed; however, they need to be combined with the back EMF, the extended EMF or the state observer(s) in the range of medium and high speed operations. Also, the methods without utilizing the HF signal injection are still problematic and open to research specifically at very low and zero speeds. From this point of view, it is crucial to reveal how successful and stable the estimations can be executed by the introduced methods without inclusion of the HF signal injection as the rotor speed goes down to very low and zero speeds.

Considering the position-sensorless methods mentioned above, the extended EMF technique specifically presented in Ref. [13] does not need any HF signal injection and offers very straightforward design procedure. Also, it can be easily realized in or embedded on the low-cost hardware platforms. Because Ref. [13] exploit the extended EMF estimators in order to estimate the rotor position and speed, it is very clear that the performance of this estimator is deteriorated when the rotor speed becomes very low. Because of this reason, Ref. [14] utilizes the extended EMF method in Ref. [13] together with the methods including HF signal injection. However, no effort is shown in both Ref. [13] and Ref. [14] in order to report the limit of the stable low speed

M. Barut, S.-Y. Jung, C. Mi

estimation performance. Also, both studies [13, 14] use interior permanent magnet synchronous motors (IPMSMs) in real-time experiments to verify the proposed or implemented estimation algorithms. In addition, Ref. [13] declares that the proposed extended EMF approach is applicable to surface permanent magnet synchronous motors (SPMSMs) and the synchronous reluctance motors.

The main contribution of this paper is to implement the extended EMF based position-sensorless drive in both simulation and real time for the speed control of the SPMSM especially concentrating on very low and medium speeds. Thus, differently from the past studies [13, 14], this paper purposes

-To verify the possible limit of low speed estimation of the extended EMF method

-To validate the extended EMF method suitable to SPMSMs with the help of the challenging simulations and the real-time experiments. From this perspective, it is first known study in the literature and the extended version of the study in [15] which does not consist of the performance tests related to the simulations of the designed position-sensorless control system. The results obtained from simulation and real-time experiments proves the applicability and effectiveness of the developed position-sensorless drive system. Also, ıt is revealed that the stable low speed estimation and control can be executed till 1.4286 % of the rated speed for SPMSM with 0.0262 Vrms/rpm.

2. DEVELOPMENT OF SPEED AND POSITION ESTIMATORS BASED ON EXTENDED EMF FOR SPMSM

For this purpose, firstly the stator voltage equations [13, 14] of a PMSM in the rotating $dq-$axes can be given as:

$$v_{sd} = R_s i_{sd} + L_{sd} \frac{di_{sd}}{dt} - \omega L_{sq} i_{sq} \tag{1}$$

$$v_{sq} = R_s i_{sq} + L_{sq} \frac{di_{sq}}{dt} + \omega L_{sd} i_{sd} + \omega \psi_f \tag{2}$$

or

$$\begin{bmatrix} v_{sd} \\ v_{sq} \end{bmatrix} = \begin{bmatrix} R_s + pL_{sd} & -\omega L_{sq} \\ \omega L_{sd} & R_s + pL_{sq} \end{bmatrix} \begin{bmatrix} i_{sd} \\ i_{sq} \end{bmatrix} + \begin{bmatrix} 0 \\ \omega \psi_f \end{bmatrix} \tag{3}$$

Here, R_s is the stator resistance. L_{sd} and L_{sq} are d and q axis components of the stator inductances, respectively. i_{sd} and i_{sq} are d and q axis components of the stator inductances, respectively. ψ_f is the EMF constant. ω is the synchronous speed at which $dq-$frame rotates, as shown in Figure 1. p in (3) represents the differential operator.

Because the $dq-$model in (3) does not directly contain the rotor position, θ, it is decided to use the mathematical model represented in the estimated rotating axis named as $\gamma\delta-$frame, which lags $dq-$axes by θ_e shown in Figure 1, in Ref. [13]. Therefore, (3) is rewritten in $\gamma\delta-$frame as follows [16]:

$$\begin{bmatrix} v_\gamma \\ v_\delta \end{bmatrix} = \begin{bmatrix} R_s + pL_{sd} & -\omega L_{sq} \\ \omega L_{sq} & R_s + pL_{sd} \end{bmatrix} \begin{bmatrix} i_\gamma \\ i_\delta \end{bmatrix} + \begin{bmatrix} e_\gamma \\ e_\delta \end{bmatrix} \tag{4}$$

$$\begin{bmatrix} e_\gamma \\ e_\delta \end{bmatrix} \triangleq E_{ex} \begin{bmatrix} -\sin\theta_e \\ \cos\theta_e \end{bmatrix} + (\hat{\omega} - \omega) L_d \begin{bmatrix} -i_\delta \\ i_\gamma \end{bmatrix} \tag{5}$$

$$E_{ex} \triangleq \omega \left[(L_{sd} - L_{sq}) i_{sd} + \psi_f \right] - (L_{sd} - L_{sq}) p i_{sq} \tag{6}$$

Here e_γ and e_δ are named as γ and δ axis components of the extended EMF. Also, (4) is a general form applicable [13, 16] to

-SPMSM when $L_{sd} = L_{sq}$

-IPMSM when $L_{sd} < L_{sq}$

-Synchronous Reluctance Motors (SYNRMs) when $\psi_f = 0$

At this step, $\hat{e}_\gamma$ and $\hat{e}_\delta$ are firstly determined by exploiting the assumption of $L \triangleq L_{sd} = L_{sq}$ related to SPMSM in (4) – (6) as demonstrated in Figure 2.

DESIGN AND REAL-TIME IMPLEMENTATION OF EXTENDED EMF BASED POSITION-SENSORLESS DRIVE FOR SURFACE MOUNTED PERMANENT MAGNET SYNCHRONOUS MACHINES
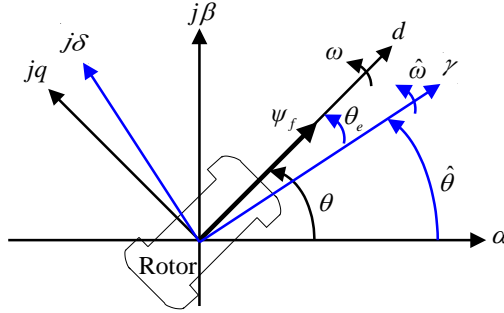

Figure 1. Positions of $\alpha\beta$ − stationary (stator-fixed) frame, dq − field frame rotating at ω , and $\gamma\delta$- estimated frame rotating at $\hat{\omega}$ for design of the extended EMF method.
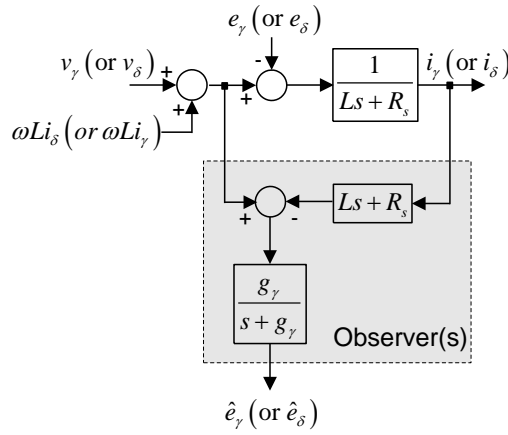

Figure 2. Least-order observer(s) for estimations of e_γ and e_δ .

Secondly, because the estimated rotor speed error, $\hat{\omega} - \omega \cong 0$, is small enough, the extended EMF can be also estimated from (5), as follows:

$$\begin{bmatrix} \hat{e}_\gamma \\ \hat{e}_\delta \end{bmatrix} = E_{ex} \begin{bmatrix} -\sin\theta_e \\ \cos\theta_e \end{bmatrix} \tag{7}$$

Finally, θ_e is estimated by

$$\hat{\theta}_e = \tan^{-1}\left(\frac{\hat{e}_\gamma}{\hat{e}_\delta}\right) \tag{8}$$

To make $\hat{\theta}_e$ equal to zero, the estimated speed ($\hat{\omega}$) and position ($\hat{\theta}$) need to be compensated by the equivalent close-loop system as shown in Figure 3. By utilizing the desired operating points related to the close-loop system, the proportional gain, K_p , and integral gain, K_i of the PI controller are obtained as:

$$K_p = 2\xi w_n, \ K_i = w_n^2 \tag{9}$$

Here, ξ and w_n are the damping ratio and the natural frequency of the desired response, respectively.
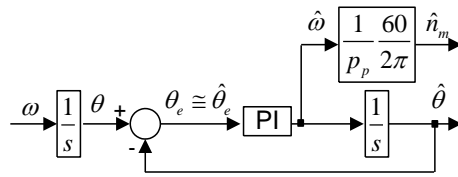
M. Barut, S.-Y. Jung, C. Mi

Figure 3. An equivalent close-loop system for the extended EMF based speed and position estimators

3. COMPUTER SIMULATIONS OF POSITION-SENSORLESS SPMSM DRIVE

The principle scheme of the position-sensorless SPMSM drive designed in MATLAB® Simulink is given in Figure 4. Here, the extended EMF based observer is built on Figure 3 utilizing the calculations of $\hat{e}_\gamma$ and $\hat{e}_\delta$ in Figure 2 and $\hat{\theta}_e$ in Eq. 8. In Figure 4, the speed and the current controllers are conventional PIs, and the rated parameters of the SPMSM are given in Table I. The sampling time, T, is 10μs.

Different scenarios are considered in computer simulations to show that the extended EMF based observer in this paper is applicable to SPMSMs in the design of position-sensorless drive. These scenarios focus on the performances at very low and medium speeds which are given in Figures 5 and 6. Analyzing the simulation results in Figures 5 and 6, the following observations are made:

- Transition to position-sensorless case occurs at 0.5s under *no-load* in Figure 5 and *rated-load* in Figure 6. It is observed that the transitions in both cases can be easily carried out without disturbing the desired behavior of the drive or control system.
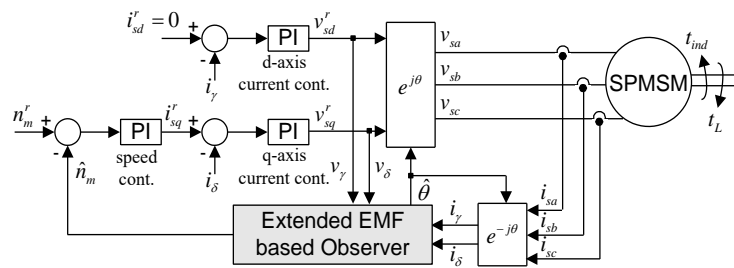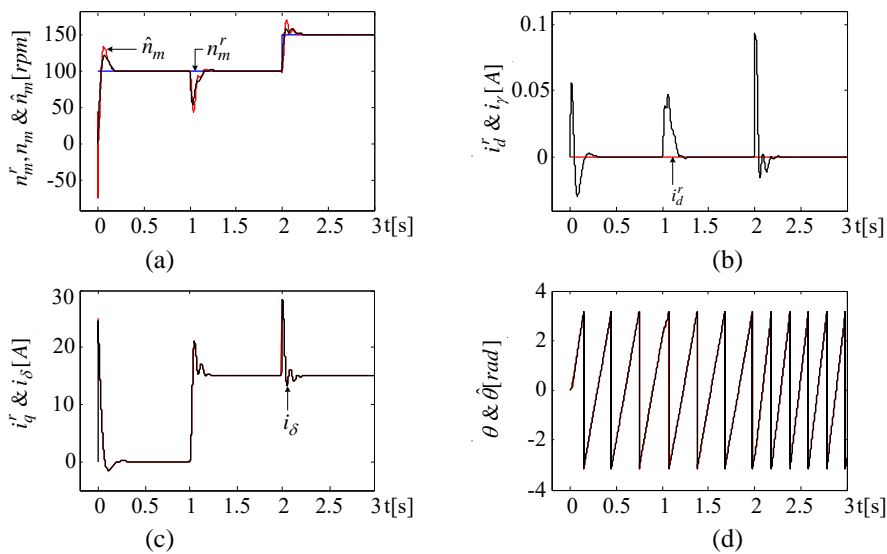

Figure 4. The principle scheme of the designed position-sensorless SPMSM drive in MATLAB® Simulink

DESIGN AND REAL-TIME IMPLEMENTATION OF EXTENDED EMF BASED POSITION-SENSORLESS DRIVE FOR SURFACE MOUNTED PERMANENT MAGNET SYNCHRONOUS MACHINES
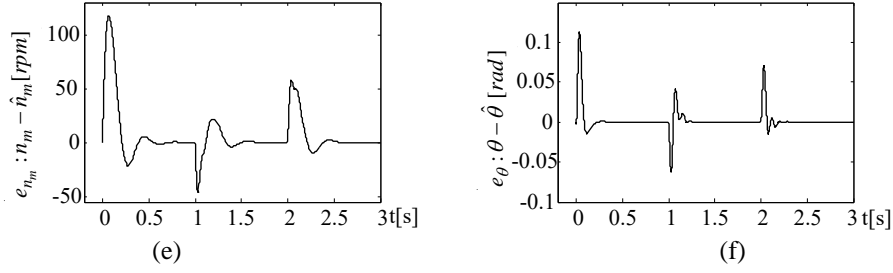

Figure 5. Simulation results at very low speeds. (a) Variations of n_m^r, n_m, and $\hat{n}_m$. (b) Variations of i_d^r and i_γ. (c) Variations of i_q^r and i_δ. (d) Variations of θ and $\hat{\theta}$. (e) Variation of $e_{n_m} = n_m - \hat{n}_m$. (f) Variation of $e_\theta = \theta - \hat{\theta}$.

Figure 6. Simulation results at low & medium speeds. (a) Variations of n_m^r, n_m, and $\hat{n}_m$. (b) Variations of i_d^r and i_γ. (c) Variations of i_q^r and i_δ. (d) Variations of θ and $\hat{\theta}$. (e) Variation of $e_{n_m} = n_m - \hat{n}_m$. (f) Variation of $e_\theta = \theta - \hat{\theta}$.
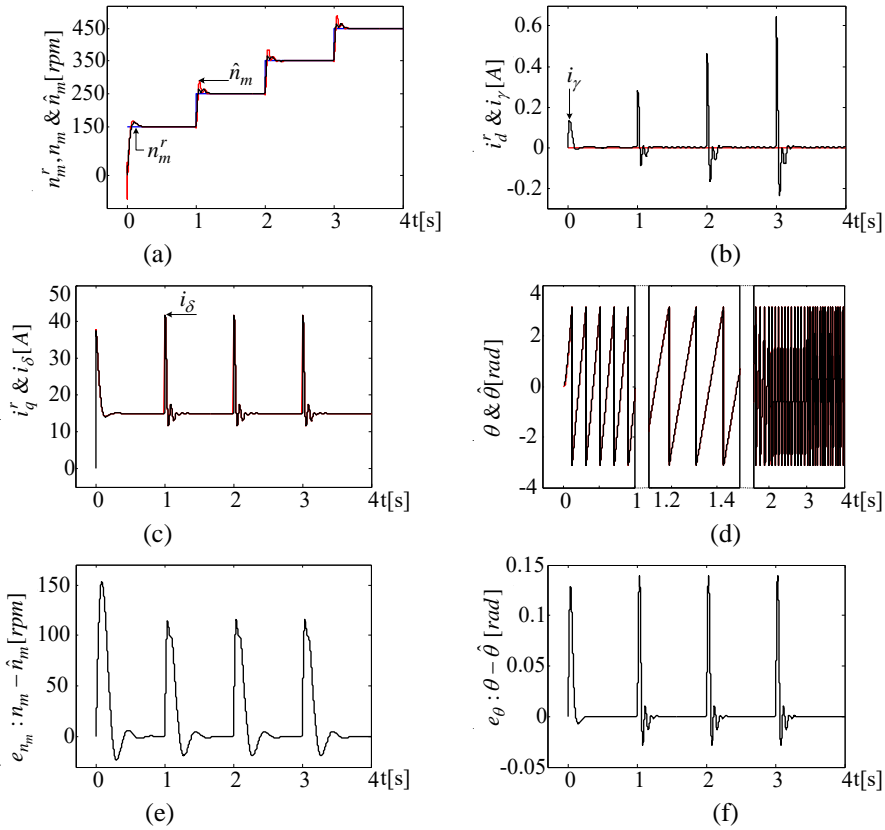
- Under step-like changes in speed reference, n_m^r, the extended EMF based observer and thus the position-sensorless SPMSM drive demonstrate quite acceptable tracking performance at very low speeds in Figure 5 and at low and medium speeds in Figure 6.

- Inspite of the challenging variations in n_m^r in Figures 5 and 6, the estimation performances of the extended EMF based observer are very good. In addition to these variations, the load torque, t_L, is abruptly increased from 0 N.m to the rated value of 4.61 N.m at 1 s in Figure 5, the estimated states, $\hat{n}_m$ and $\hat{\theta}$, closely follow real ones, n_m and θ, respectively. These realities can be discovered by inspecting the estimation errors, $e_{n_m} = n_m - \hat{n}_m$ and $e_\theta = \theta - \hat{\theta}$, converging to zero very quickly in Figure 5(e), Figure 5(f), Figure 6(e), and Figure 6(f).

From the computer simulations, it is concluded that the extended EMF based observer in this paper is capable to work under both no-load and rated load even at very low to medium speeds; therefore, it can be used for the design of position-sensorless SPMSMs drive.

M. Barut, S.-Y. Jung, C. Mi

4. EXPERIMENTAL SET-UP

The general view of the real-time test bench utilized to demonstrate performances of the extended EMF based speed and position estimators and thus position-sensorless drive including SPMSM is given in Figure 7, and Table I shows rated parameters of the SPMSM. The SPMSM is loaded by separately excited direct current machine. The designed position-sensorless control system based on extended EMF is embedded in the power PC-based DS1104 controller board processing floating-point operations at a rate of 250 MHz. The incremental encoder of 2048 lines/rev is only utilized to correct position and speed estimations.

The schematic view of the implemented position-sensorless SPMSM control system is also presented in Figure 8. Here, SV-PWM denotes space vector-pulse with modulation technique. As can be seen from Figure 8, the extended EMF based estimator exploits only the stator phase currents, i_γ and i_δ, as measured variables. The required voltage signals, v_γ and v_δ, are directly achieved from the outputs of d- and q-axis current controllers.
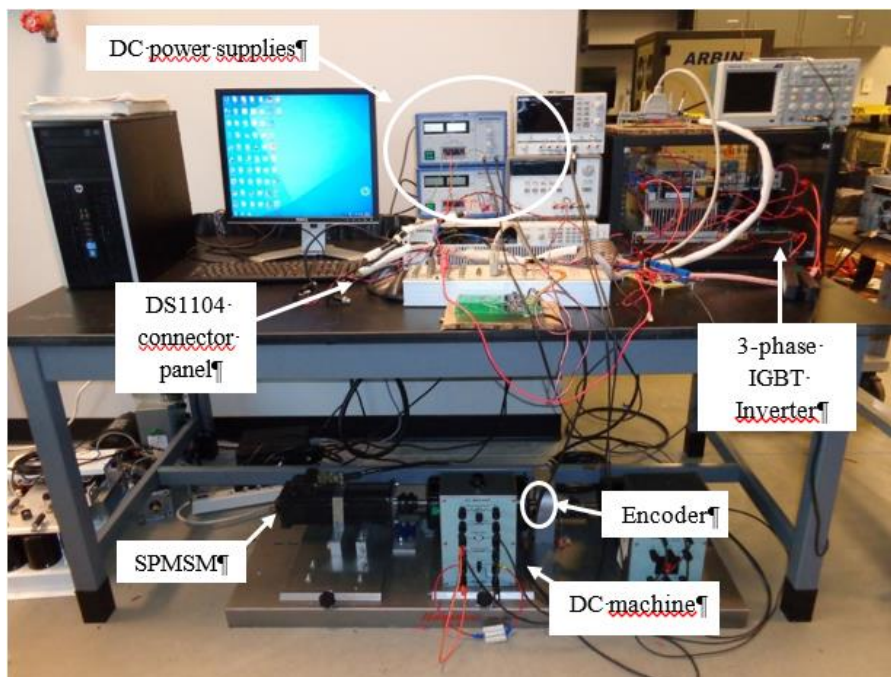

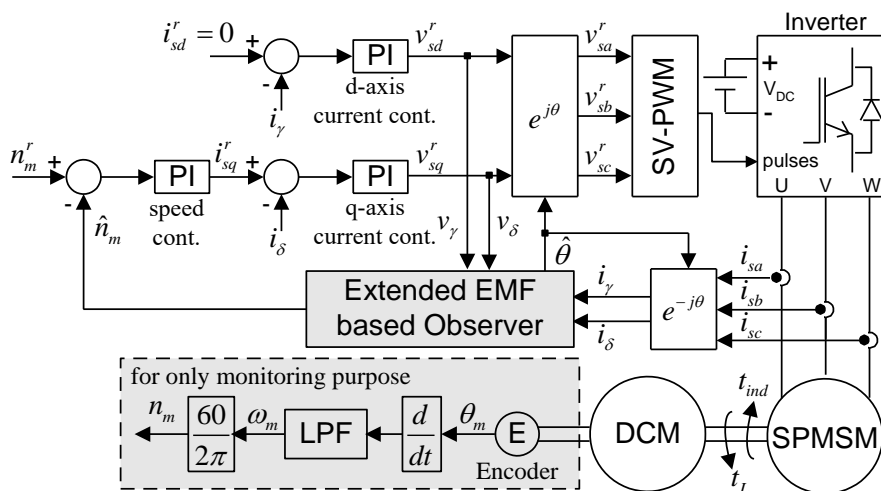**Figure 7.** General view of the real-time test bench.

Figure 8. The principle scheme of the designed position-sensorless SPMSM drive.

6

DESIGN AND REAL-TIME IMPLEMENTATION OF EXTENDED EMF BASED POSITION-SENSORLESS DRIVE FOR SURFACE MOUNTED PERMANENT MAGNET SYNCHRONOUS MACHINES

5. REAL-TIME EXPERIMENTAL RESULTS

In order to evaluate the performance of the extended EMF based position-sensorless SPMSM drive in the real-time experiments with the sampling time, T, of 1/(8kHz), three scenarios are generated for the different speed operations as follows:
-Very low speed operation
-Very low and medium speed operations
-High speed operation

5.1. Performance at very low speed operation (Figure 9)

In this section, it is desired to show the lowest possible speed control limit which can be performed by the extended EMF based position-sensorless SPMSM drive. For this aim, n_m^r is instantly increased to 150 rpm at 2.7 s and decreased to 100 rpm at 7.5 s speed while the SPMSM rotates at 100 rpm. The resulting performance is presented in Figure 9. As demonstrated in Figure 9(a) and (e), $\hat{n}_m$ closely tracks n_m. The speed and current controllers also show satisfactory tracking performance in Figure 9(a), (b), and (c). Moreover, inspecting Figure 9(d) and (f), it can be seen that the average value of $e_\theta = \theta - \hat{\theta}$ is about 0.6480[rad] (37.12 Deg). As n_m^r (or n_m) approaches to zero, $e_\theta = \theta - \hat{\theta}$ gets increased since the extended EMF term is deteriorated with the increasing noise on the measured i_γ and i_δ and finally vanishes. For the SPMSM with 0.0262 Vrms/rpm, it is observed that the acceptable position-sensorless close-loop speed control can be performed down to 100 [rpm] which is equal to 1.4286 % of the rated speed.
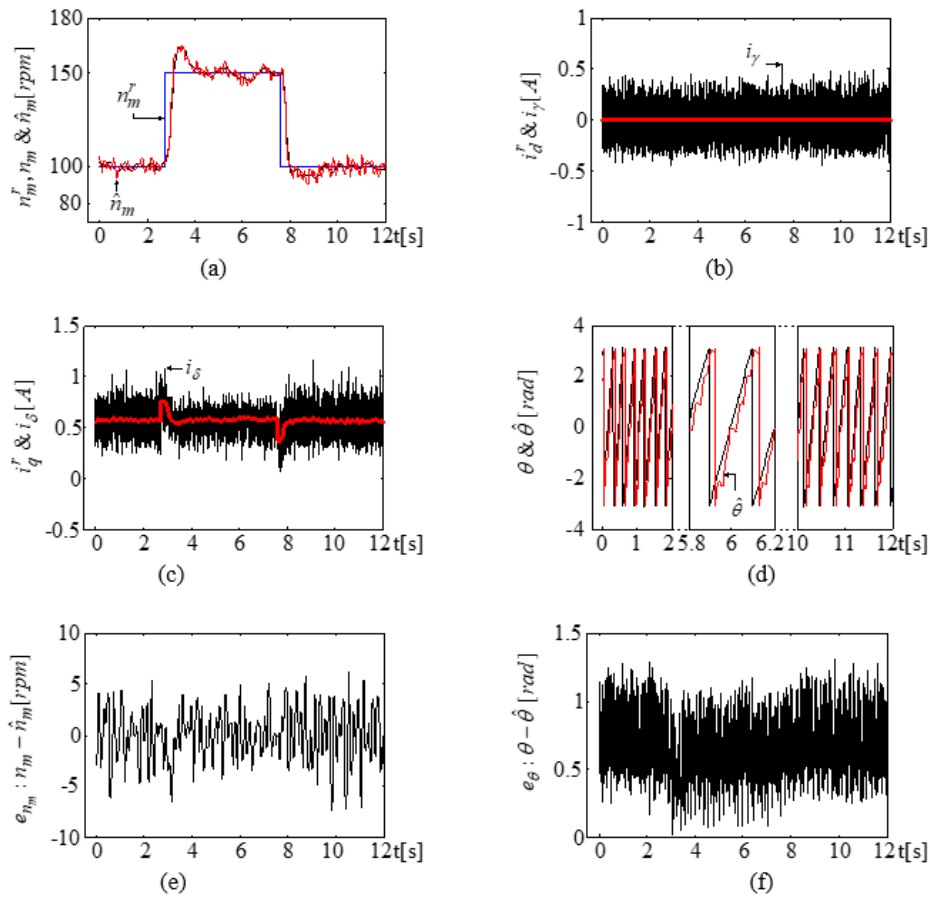

Figure 9. Real-time results at very low speeds. (a) Variations of n_m^r, n_m, and $\hat{n}_m$. (b) Variations of i_d^r and i_γ. (c) Variations of i_q^r and i_δ. (d) Variations of θ and $\hat{\theta}$. (e) Variation of $e_{n_m} = n_m - \hat{n}_m$. (f) Variation of $e_\theta = \theta - \hat{\theta}$.

M. Barut, S.-Y. Jung, C. Mi

5.2. Performance at very low and medium speed operations (Figure 10)

This scenario aims to illustrate the transition performance of the position-sensorless drive from the very low speeds to medium speeds. Therefore, the increased step-like variations of 150 [rpm] are given to n_m^r from [150] rpm to 600 [rpm], and the obtained results are given in Figure 10. Figures 10(a), (b), and (c) validate the successful control performances of the speed and current controllers while Figures 10(d) and (e) verify the very good estimation performances of the speed and position. Further, as can be seen from Figure 10(d) and (e), after the step change in n_m^r at 2 s, $e_\theta = \theta - \hat{\theta}$ suddenly decreases to very small values. Namely, $e_\theta = \theta - \hat{\theta}$ becomes smaller when n_m^r (or n_m) raises, as expected.
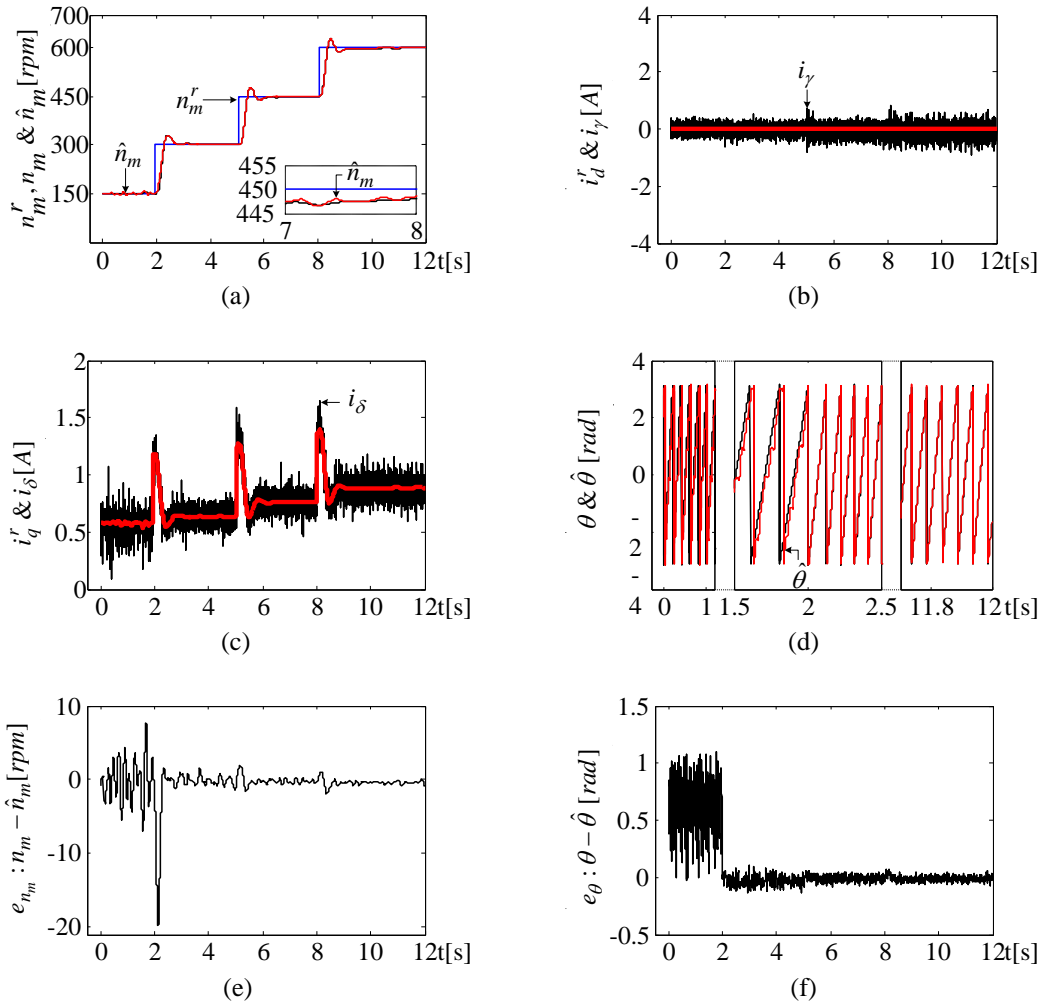

Figure 10. Real-time results at low & medium speeds. (a) Variations of n_m^r, n_m, and $\hat{n}_m$. (b) Variations of i_d^r and i_γ. (c) Variations of i_q^r and i_δ. (d) Variations of θ and $\hat{\theta}$. (e) Variation of $e_{n_m} = n_m - \hat{n}_m$. (f) Variation of $e_\theta = \theta - \hat{\theta}$.

5.3. Performance at high speed operation (Figure 11)

In this scenario, it is also aimed to show the high speed control and estimation performances of the developed position sensorless SPMSM drive. For this pupose, n_m^r is stepped down to 1250 [rpm] at 1.8 s, 1100 [rpm] at 4.9 s, and 950 [rpm] at 7.9 s, respectively while the SPMSM revolves at 1400 [rpm]. The results given in Figure 11 for this scenario confirm the perfect tracking and estimation abilities of the designed extended EMF based position-sensorless SPMSM drive.

DESIGN AND REAL-TIME IMPLEMENTATION OF EXTENDED EMF BASED POSITION-SENSORLESS DRIVE
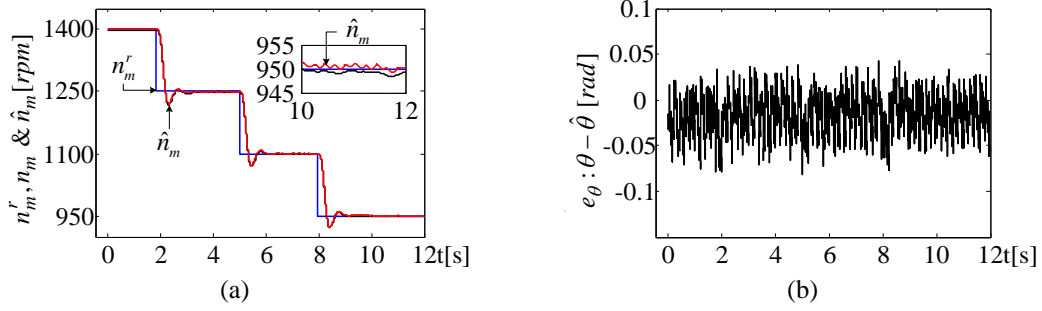*FOR SURFACE MOUNTED PERMANENT MAGNET SYNCHRONOUS MACHINES*

Figure 11. Real-time results at high speeds. (a) Variations of n_m^r, n_m, and $\hat{n}_m$. (f) Variation of $e_\theta = \theta - \hat{\theta}$.

6. CONCLUSION

In this paper, an extended EMF based position-sensorless control system has been developed for the speed control of SPMSM and realized in simulations and real-time experiments in order to reveal that the extended EMF method proposed in Ref. [13] including IPMSM is also suitable to SPMSMs. For this purpose, the computer simulations are firstly executed to demonstrate that the extended EMF based observer is capable to serve for the design of the position-sensorless SPMSM drive. Later, the real-time experiments are performed to show achievements of the extended EMF based position-sensorless drive at very low, medium, and high speeds. Both the computer simulations and real-time experimental results have validated the feasibility and effectiveness of the proposed position-sensorless drive in this paper. Moreover, differently from Refs. [13] and [14], this study has specifically concentrated on the performance at very low speeds. As a result, the low speed operation by the developed position-sensorless close-loop speed control system including the EMF approach in Ref. [13] is possible till 100 rpm (1.4286 % of the rated speed) for the SPMSM with 0.0262 Vrms/rpm. These efforts are firstly introduced to the current literature in the scope of this paper.

ACKNOWLEDGEMENT

APPENDIX

The rated parameters of the SPMSM are given in Table I.

Table 1. Rated parameters of the SPMSM used in real-time experiments

Parameter	Symbol	Value	Unit	Parameter	Symbol	Value	Unit
Pole pair	p_p	2	-	Rated speed	n_m	7000	Rpm
Rotor pole flux	ψ_f	0.10214	V.s	Rated torque	t_L	4.61	Nm
d-inductance	L_{sd}	0.01	H	Rated phase current	I_s	15	Arms
q-inductance	L_{sq}	0.01	H	Rated L-L Voltage	V_s	230	Vrms
Stator resistance	R_s	0.19	Ω	Rated power	P	4.5	kW

M. Barut, S.-Y. Jung, C. Mi

REFERENCES

[1] K. T. Chau, C. C. Chan, and C. Liu, "Overview of permanent-magnet brushless drives for electric and hybrid electric vehicles," *IEEE Transaction on Industrial Electronics*. vol. 55, no. 6, pp. 2246-2257, 2008.

[2] R. Bojoi, M. Pastorelli, J. Bottomley, P. Giangrande, and C. Gerada, "Sensorless control of PM motor drives — A technology status review," 2013 IEEE Workshop on Electrical Machines Design Control and Diagnosis (WEMDCD) Paris, France, 2013, pp. 168-182.

[3] Y. Zhao, W. Qiao, and L. Wu, "An Adaptive Quasi Sliding-Mode Rotor Position Observer-Based Sensorless Control for Interior Permanent Magnet Synchronous Machines," *IEEE Transactions on Power Electronics*, vol. 28, no.12, pp. 5618-5629, 2013.

[4] G.Wang, M. Valla, and J. Solsona, "Position Sensorless Permanent Magnet Synchronous Machine Drives—A Review," *IEEE Transaction on Industrial Electronics*. vol. 67, no. 7, pp. 5830-5842, 2020.

[5] C. Gong, Y. Hu, J. Gao, Y. Wang, and L. Yan, "An Improved Delay-Suppressed Sliding-Mode Observer for Sensorless Vector-Controlled PMSM," *IEEE Transaction on Industrial Electronics*. vol. 67, no. 7, pp. 5913-5923, 2020.

[6] C. Lascu and G.-D.Andreescu, "PLL Position and Speed Observer With Integrated Current Observer for Sensorless PMSM Drives," *IEEE Transaction on Industrial Electronics*. vol. 67, no. 7, pp. 5990-5999, 2020.

[7] C. M. Verrelli, S. Bifaretti, E. Carfagna, A. Lidozzi, L. Solero, F. Crescimbini, and M. D. Benedetto, "Speed Sensor Fault Tolerant PMSM Machines: From Position-Sensorless to Sensorless Control," *IEEE Transactions on Industry Applications*, vol. 55, no. 4, pp. 3946-3954, 2019.

[8] M. Boussak, "Implementation and experimental investigation of sensorless speed control with initial rotor position estimation for interior permanent magnet synchronous motor drive," *Transactions on Power Electronics*, vol. 20, no. 6, pp. 1413-1422, 2005.

[9] O. Benjak and D. Gerling, "Review of position estimation methods for IPMSM drives without a position sensor part I: Nonadaptive methods," 2010 XIX Int. Conf. on Electrical Machines (ICEM) Rome, Italy, 2010, on CD.

[10] O. Benjak and D. Gerling, "Review of position estimation methods for IPMSM drives without a position sensor part II: Adaptive methods", 2010 XIX Int. Conf. on Electrical Machines (ICEM) Rome, Italy, 2010, on CD.

[11] A. Sarikhani and O.A. Mohammed, "Sensorless control of PM synchronous machines by physics-based EMF observer," *IEEE Transaction on Energy Conversion*. vol. 27 no. 4, pp. 1009-1017, 2012.

[12] Y. Zhao, Z. Zhang; W. Qiao, and L. Wu, "An extended flux model-based rotor position estimator for sensorless control of salient-pole permanent-magnet synchronous machines," *IEEE Transactions on Power Electronics*, vol. 30, no.8, pp. 4412-4422, 2015.

[13] S. Morimoto, K. Kawamoto, M. Sanada, and Y. Takeda, "Sensorless control strategy for salient-pole PMSM based on extended EMF in rotating reference frame," *IEEE Transactions on Industry Applications*, vol. 38, no. 4, pp. 1054-1061, 2002.

[14] J. Hong, S. -Y, Jung, and K. Nam, "An incorporation method of sensorless algorithms: Signal injection and back EMF based methods," 2010 Int. Power Electron. Conf. (IPEC) Sapporo, Japan, 2010, pp. 2743-2747.

[15] M. Barut, S.-Y. Jung, and C. Mi, "Real-time performance evaluation of extended EMF based sensorless drive for SPMSMs," 2014 XXIth Int. Conf. on Electrical Machines (ICEM) Berlin, Germany, 2014, pp. 884-889.

[16] Z. Chen, M. Tomita, S. Ichikawa, S. Doki, and S. Okuma, "Sensorless control of interior permanent magnet synchronous motor by estimation of an extended electromotive force,"2000 IEEE- Ind. App. Conf., Rome, Italy, 2000, pp. 1814-1819.

DETERMINATION of STABILITY MARGINS in SINGLE AREA LOAD FREQUENCY CONTROL SYSTEM HAVING INCOMMENSURATE COMMUNICATION DELAYS DUE TO PLUG-IN ELECTRIC VEHICLES

Ausnain NAVEED[1] iD , Şahin SÖNMEZ[2,*] iD , Saffet AYASUN[3] iD

[1] *Niğde Ömer Halisdemir University, Department of Electrical and Electronics Engineering, 51240, Niğde, Turkey*
[2] *Malatya Turgut Özal University, Department of Electronic and Automation, Malatya, Turkey*
[3] *Gazi University, Department of Electrical and Electronics Engineering, 06570 Maltepe/Ankara, Turkey*

ABSTRACT

This work investigates the impact of time delays on the stability of a single-area load frequency control (LFC) system that includes plug-in multiple electric vehicles (EVs) aggregators to regulate the system frequency. Communication delays are caused by open communication networks used to transceive control signals. These delays can degrade the performance of the controller leading to undesired system frequency oscillations and may even cause instability if they exceed an upper bound limit known as stability margin. These delays can be commensurate or incommensurate depending upon the nature of the communication network. Hence, it is important to determine stability margins of the single-area LFC system with plug-in EVs aggregators to ensure the stable operation under both types of delays. This study determines the stability margins for extensive proportional-integral (PI) controller gains of the single-area LFC system with plug-in EVs by implementing a simulation approach. The knowledge of stability delay margins makes it possible to appropriately tune the PI controller gains that ensure a stable operation of the LFC system even in the presence of inevitable communication delays.

Keywords: Load frequency control, Electric vehicles, Communication delays, Stability margins

1. INTRODUCTION

Renewable energy (RE) resources have been highly regarded in the power generation due to increasing environmental concerns. However, such a power generation supplies variable electric power output and may cause irregularities in the desired system frequency. Although, Energy Storage System (ESS) of batteries can be utilized as an alternate to obtain constant power output, but, it is an expensive power source. Interestingly, EVs batteries can be used for large-scale energy storage in the power system. EVs have become perceptible in frequency regulation of independently controlled interconnected systems [1]. Their batteries can decrease or increase power output faster than traditional generation sources. This attribute of EVs enables the LFC system to improve its dynamic performance. EVs are capable of reducing fluctuations to improve frequency response because they can be utilized as generators and loads [2]-[3]. An entity known as aggregator is required by EVs to practically participate in frequency regulation market. The entity aggregates and controls a large fleet of EVs [4]-[7]. The prime objective of an aggregator is to transceive information regarding the status of EVs to/from LFC controller and rearrange the control command for dispersing EVs. Figure.1 shows a schematic of EVs plugged into the grid as a power source using vehicle-to-grid (V2G) technique.

EVs need some kind of communication network to transceive control signals to and from the LFC system controller. In general, open distributed network is used for this communication. But, such networks are susceptible to communication delays [6], [8]-[9]. These delays can result into an unstable LFC system in spite of an expectation that EVs are capable of improving the dynamic system performance. Thus, it is necessary to analyze delay-dependent system stability improved by EVs. Also, it is important to determine the stability margins which is defined as the admissible upper bound limit of the communication delay [8].

A number of approaches are discussed in the existing literature to identify the stability margins of dynamical systems experiencing communication delays. The approaches can be classified as: a) time-domain approaches and b) frequency-domain direct methods. The latter intends to compute complex roots of the characteristic polynomial of the system on the imaginary axis. This group is comprised of approaches like; removal of transcendental terms in the characteristic polynomial [10], the contour integral (or, argument principle) method [11], delay space re-scaling approach [12], Schur-Cohn method [13] and Rekasius

A. Naveed, Ş. Sönmez, S. Ayasun

substitution [14] - [15]. This group of methods is able to calculate exact stability margins. But, the basic shortcoming of these approaches is that they cannot compute delay margins for the case of time-varying communication delays.

A comprehensive literature review on the stability margin estimation methods for linear continuous time-invariant systems experiencing constant communication delays is presented in [16]. Among those approaches, the direct method depending upon the elimination of transcendental terms [10] is effectively implemented in [17] to identify stability margins for time-delayed LFC systems. The Rekasius substitution method is employed for computing stability margins for single-area LFC system with plug-in EVs aggregator [18]. The delay space re-scaling approach presented in [12] is employed for determining the stability margins of hybrid ESS having hierarchical DC micro-grids control and experiencing multiple communication delays. The latter group of methods uses linear matrix inequalities (LMIs) method together with Lyapunov stability theory. These methods are presented in [8], [19] to compute the stability margins of LFC systems and in [20] to calculate the stability margins of micro-grid. Both constant and time-varying delay problems can be addressed using this group of indirect methods, but, they provide more conservative stability margins when compared with the previously discussed group of direct methods [17].

This work is the extended version of the paper titled, *Stability Analysis of a Single-Area Load Frequency Control System with Electric Vehicles Group and Communication Time Delays* [21]. The reported work presented only the effect of commensurate delays on LFC system with plug-in EVs. However, this work implements time-domain simulations [22] based approach for determining stability margins in single-area LFC system with multiple plug-in EVs aggregators while considering both commensurate and incommensurate delay scenarios. Since, each EVs aggregator may have different communication delays depending upon the technical specifications of communication technologies and networks, it is more practical to compute stability margins for both commensurate and incommensurate communication delays. Consequently, the impact of EVs participation ratio on the stability margins and the changes in stability margins relating to controller gains is also examined. The use of this approach allows to obtain exact values of stability margins.
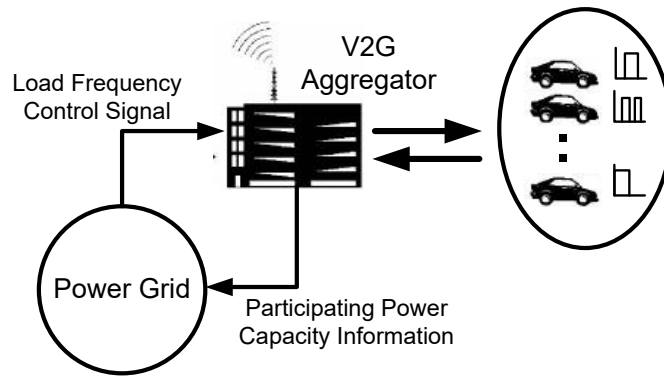

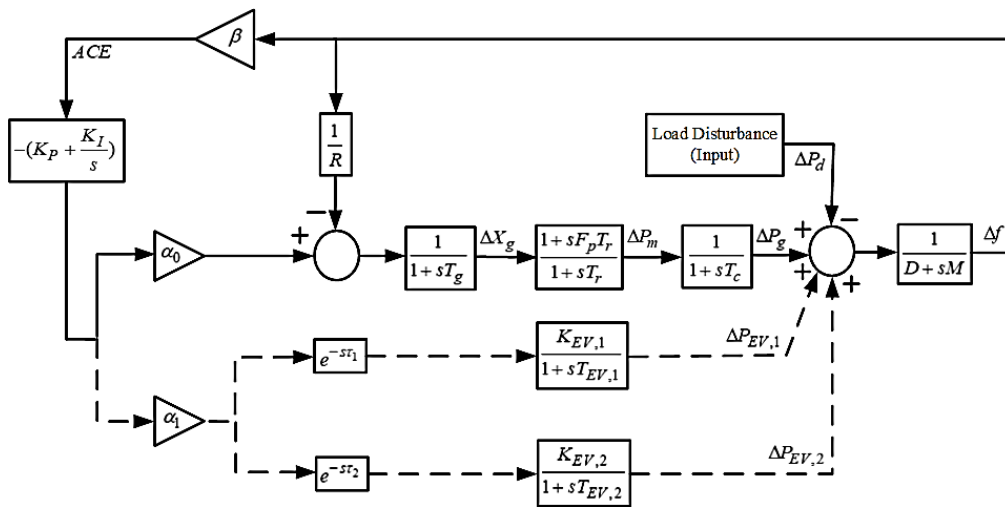**Figure 1.** EVs participation in frequency regulation service.

Figure 2. Dynamic model of single-area LFC system with EVs and communication delays.

DETERMINATION OF STABILITY MARGINS IN SINGLE AREA LOAD FREQUENCY CONTROL SYSTEM HAVING INCOMMENSURATE COMMUNICATİON DELAYS DUE TO PLUG-IN ELECTRIC VEHICLES

2. TIME-DELAYED SINGLE AREA LFC SYSTEM DUE TO THE PARTICIPATION OF EVs

A single-area LFC system with two plug-in EVs aggregators is shown in Figure 2. The EVs batteries model is defined by a first-order transfer function as follows [8]:

$$G_{EV,i}(s) = \frac{K_{EV,i}}{1 + sT_{EV,i}} \tag{1}$$

where $T_{EV,i}$ and $K_{EV,i}$ denote the time constant and gain of the EVs battery system when $(i = 1, 2)$.

In Figure 2, Δf and ΔP_d denote the frequency deviation and the load disturbance. Moreover, ΔP_g, ΔP_m, ΔX_g, ΔP_{EV1} and ΔP_{EV2} represent the generator power output, mechanical power output, the valve position and the power output of both the EVs aggregators, respectively. Furthermore, D, R, β, F_P, T_c, T_r, T_g and M denote the damping coefficient, speed regulation, frequency bias factor, fraction of the turbine power, time constants of the turbine, reheat, governor and inertia constant of generator, respectively. Whereas, K_P and K_I represent PI controller gains and the area control error is symbolized by ACE.

ACE is transmitted to PI controller as a control signal whenever there is any sudden change in the load demand. The PI controller sends the signal to EVs aggregators or reheat steam turbine depending on their participation ratios α_1 and α_0 to regulate the system frequency. The control signal received by the EVs aggregators over some kind of communication network allows them to participate in frequency regulation. It should be noticed that the communication delays from LFC controller to the first EVs aggregator (τ_1) and from LFC controller to the second EVs aggregator (τ_2) are considered as commensurate (integral multiple of each other or equal to each other) in the first scenario and incommensurate in the other scenario. These communication delays are modelled by the exponential functions of $e^{-s\tau_1}$ and $e^{-s\tau_2}$ in Figure 2. It should be emphasized here that the incommensurate delay case is the most realistic one since EVs aggregators might have different communication infrastructures that result in incommensurate (not integer multiple of each other) communication time delays [8].

It is to be mentioned here that due to the self-deployment of communication links by the Independent System Operator (ISO) and the open communication links used between EVs aggregator and EVs, only communication delays from EVs aggregators to EVs are considered in this study as the delays observed in the transmission of regulation signal from ISO to the conventional generation are less significant [23], [24].

3. IDENTIFICATION OF STABILITY MARGINS

The prime objective of stability analysis is to investigate the delay-dependent or delay-independent stability of time-delayed systems. The system will be stable for all the finite time delay values in delay-independent stability case. Whereas, in case of delay-dependent stability, the system will be stable when $\tau < \tau^*$ where τ and τ^* denote communication delay and stability margin, respectively. However, the system would be unstable as the delay values go beyond the stability margin $\tau > \tau^*$. The stability margin is the deciding factor in estimation of LFC system stability. The stability delay margin represents the maximum value of the time delay such that the LFC system will be at least marginally stable [17, 19]. For LFC system to be stable, the total communication time delay must be less than the stability delay margin. The information of stability margins for wide-ranging parameters is necessary to examine stability of the system.

Theoretically, all the roots of the characteristic polynomial of the single-area LFC system with plug-in EVs aggregators must be lying on left half of the $s-$plane to satisfy the required condition of asymptotic stability. Taking both the delays into account, the stability margin problem is all about finding value of τ^* for which the characteristic polynomial will have roots (if there exist any) on the $j\omega-$axis. Hence, time-domain simulations are executed for finding this boundary beyond which the system shows an unstable response.

4. SELECTION OF COMMUNICATION DELAYS

The communication delays τ_1 and τ_2 are expressed in polar coordinates $(|\tau|, \theta)$ as reported in [25]. All points are defined as $T(\tau_1, \tau_2)$ on a boundary relying on $(|\tau|, \theta)$ in $(\tau_1, \tau_2)-$space. Magnitude $|\tau|$ is defined as $|\tau| = \sqrt{\tau_1^2 + \tau_2^2}$ and angle θ as $\theta = \tan^{-1}(\tau_2/\tau_1)$. This polar coordinate representation of the communication delays enables us to examine the impact of

A. Naveed, Ş. Sönmez, S. Ayasun

commensurate communication delays on the stability margin by keeping the angle $\theta = 45^0$ fixed for the given values of magnitude $|\tau|$. However, any other θ value enables the user to investigate incommensurate communication delays like; $\theta = 60^0$ discussed in this study. $\theta = 60^0$ corresponds to the scenario when the communication delay between the LFC controller and second EVs aggregator is greater than the communication delay between the LFC controller and first EVs aggregator $(\tau_2 > \tau_1)$.

5. RESULTS AND DISCUSSIONS

Results of Stability margin computed by time-domain simulations for the single-area LFC system with plug-in EVs aggregators are presented in this section. For (i= 1, 2) the system parameters are given as [8]:

$$D = 1, \; R = 1/11, \; F_P = 1/6, \; \beta = 21, \; M = 8.8, \; T_g = 0.2 \; s,$$
$$T_c = 0.3 \; s, \; T_r = 12 \; s, \; T_{EV,i} = 0.1 \; s, \; K_{EV,i} = 1 \tag{2}$$

5.1. Commensurate Communication Delays

The selection of multiple delays (τ_1, τ_2) is done by using the polar coordinates and specifying the values of (τ_1, τ_2) by choosing $|\tau*|$ and θ. In order to analyze the effect of various commensurate delay values on stability margins, the angle is fixed at $\theta = 45^0$. It should be noticed that the angle $\theta = 45^0$ corresponds to the scenario in which the delay from both the EVs aggregators to the EVs is same $\tau_1 = \tau_2$. The values of the corresponding stability margin magnitude $|\tau*|$ for this case are presented in Table 1. Whereas, the time-domain simulation results are shown in Figure. 3. It can be clearly observed from the dashed line in Figure 4 that the oscillations in the frequency response of LFC-EVs system damped out showing stable operation of the system for the given parameters of PI controller $(K_P = 0.6, \; K_I = 0.8)$ and the stability delay margin magnitude $|\tau| = 0.97 \; \sec$. However, sustained oscillations in the frequency response represented by solid line in Figure 3 show that the system is marginally stable for $(K_P = 0.6, \; K_I = 0.8)$ and $|\tau| = 0.9804 \; \sec$. Even a slight change beyond this stability margin value will make the system unstable. As shown by dotted line in Figure 3, the oscillations in the frequency response of LFC-EVs system are increasing for $(K_P = 0.6, \; K_I = 0.8)$ and $|\tau| = 0.99 \; \sec$ showing an unstable operation of the system.

Moreover, the stability margin reduces with an increment in K_I for all K_P values. However, the stability margin values at first increase and then start to decrease after a specific point with an increase in K_P when K_I is fixed. These variations in the stability delay margins against the PI controller gain values for $(\alpha_1 = 0.2)$ are shown in Figure 4.

It is also imperative to examine the impact of EVs participation in the LFC system. Figure 5 shows the variation in the stability margins when the participation of EVs aggregator gradually increases. For $(K_P = 0.6, \; K_I = 0.8)$, it can be observed that the stability margin values of the system show a smooth decrement while the participation factor of EVs increases from 10% to 50%.

Table 1. Stability margins for commensurate delays $(\tau_1 = \tau_2)$

$|\tau*|$	K_I				
K_P	0.2	0.4	0.6	0.8	1.0
0.2	2.7840	1.1770	0.6511	0.3929	0.2416
0.4	3.1198	1.6890	1.0795	0.7463	0.5385
0.6	2.7470	1.8295	1.3081	**0.9804**	0.7582
0.8	2.2529	1.7302	1.3575	1.0875	0.8872
1.0	1.8377	1.5418	1.2962	1.0965	0.9354

DETERMINATION OF STABILITY MARGINS IN SINGLE AREA LOAD FREQUENCY CONTROL SYSTEM HAVING INCOMMENSURATE COMMUNICATİON DELAYS DUE TO PLUG-IN ELECTRIC VEHICLES
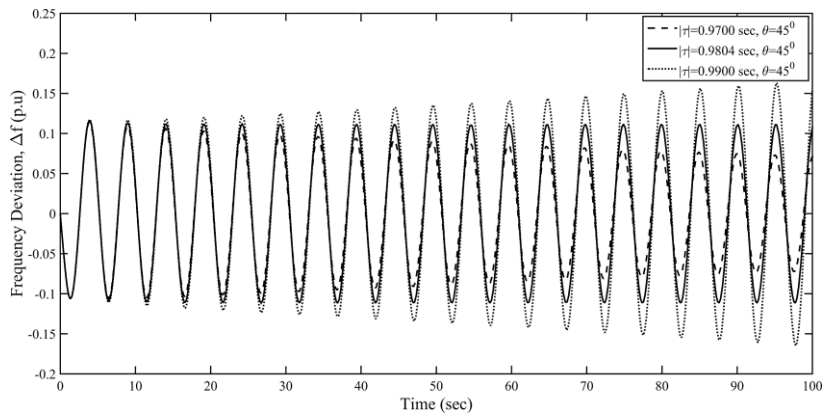

Figure 3. Frequency deviations for commensurate delays case when $(K_P = 0.6, \ K_I = 0.8)$.
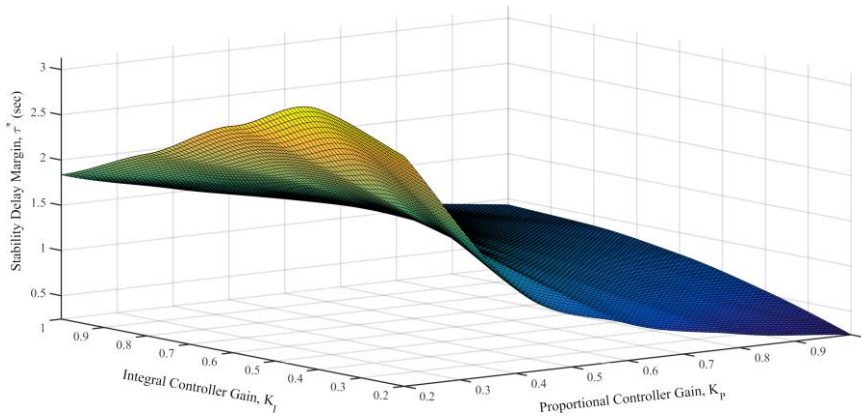

Figure 4. Variation of stability margins with respect to controller gains for $\theta = 60^0$.
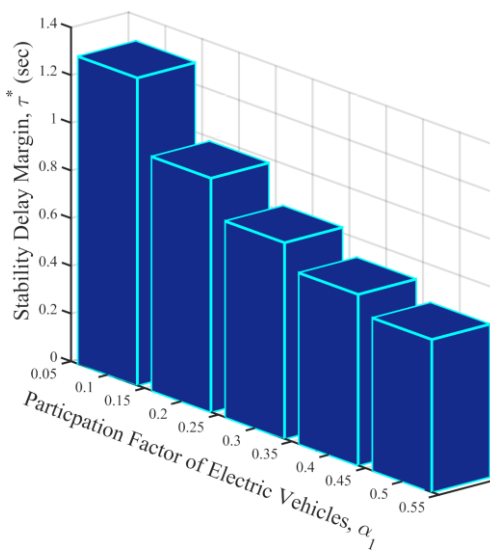

Figure 5. Variation of stability margins with respect to participation of EVs for $\theta = 45^0$.

15

5.2. Incommensurate communication delays

The impact of different incommensurate delay values (τ_1, τ_2) on stability margins is investigated by fixing the angle at $\theta = 60^0$. This corresponds to the scenario when $(\tau_2 \neq \tau_1)$. The values of the corresponding stability delay margin magnitude $|\tau|$ for this case are presented in Table 2 and the time-domain simulation results are shown in Figure 6. For a given set of PI controller gains $(K_P = 0.6, K_I = 0.6)$ and the stability margin magnitude $|\tau| = 1.35$ sec, the dashed line illustrates that oscillations in the frequency response of LFC system with plug-in EVs aggregators damped out showing stable operation of the system. However, sustained oscillations in the frequency response represented by solid line show that the system is marginally stable for $(K_P = 0.6, K_I = 0.6)$ when $|\tau| = 1.3833$ sec. Likewise, a slight change beyond this stability margin value will make the system unstable. As shown by the dotted line in Figure 6, the oscillations in the frequency response of LFC-EVs system are increasing for $(K_P = 0.6, K_I = 0.6)$ when $|\tau| = 1.40$ sec.

Similar to the commensurate delays scenario, the stability margin decreases with an increase in K_I for all values of K_I. Also, these values show a same trend by initially increasing and then decreasing after a specific point with an increase in K_P when K_I is fixed. These variations in the stability delay margins against the PI controller gain values for $(\alpha_1 = 0.2)$ are shown in Figure 7.

The impact of the participation of EVs in the LFC system is also studied for commensurate delays case. Figure 8 shows the variation in the stability margins when the participation of EVs gradually increases. For $(K_P = 0.6, K_I = 0.6)$, it can be observed that the delay margin values of the system show a sudden initial decrease and keeps on decreasing when the participation factor of EVs increases.

Table 2. Stability margins for incommensurate delays $(\tau_1 \neq \tau_2)$

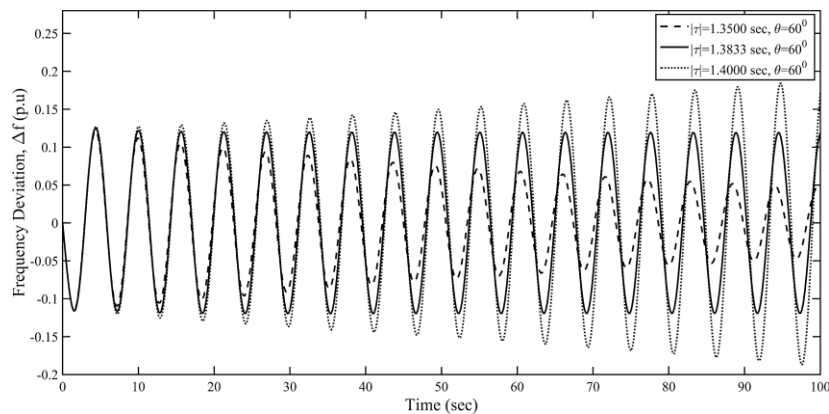| $|\tau*|$	K_I				
K_P	0.2	0.4	0.6	0.8	1.0
0.2	2.9954	1.2274	0.6751	0.4068	0.2504
0.4	3.5050	1.7890	1.1285	0.7761	0.5592
0.6	3.1845	1.9775	**1.3833**	1.0266	0.7898
0.8	2.6490	1.9089	1.4562	1.1505	0.9315
1.0	2.1595	1.7244	1.4092	1.1733	0.9900

Figure 6. Frequency deviations for incommensurate delays case when $(K_P = 0.6, K_I = 0.6)$.

DETERMINATION OF STABILITY MARGINS IN SINGLE AREA LOAD FREQUENCY CONTROL SYSTEM HAVING INCOMMENSURATE COMMUNICATİON DELAYS DUE TO PLUG-IN ELECTRIC VEHICLES
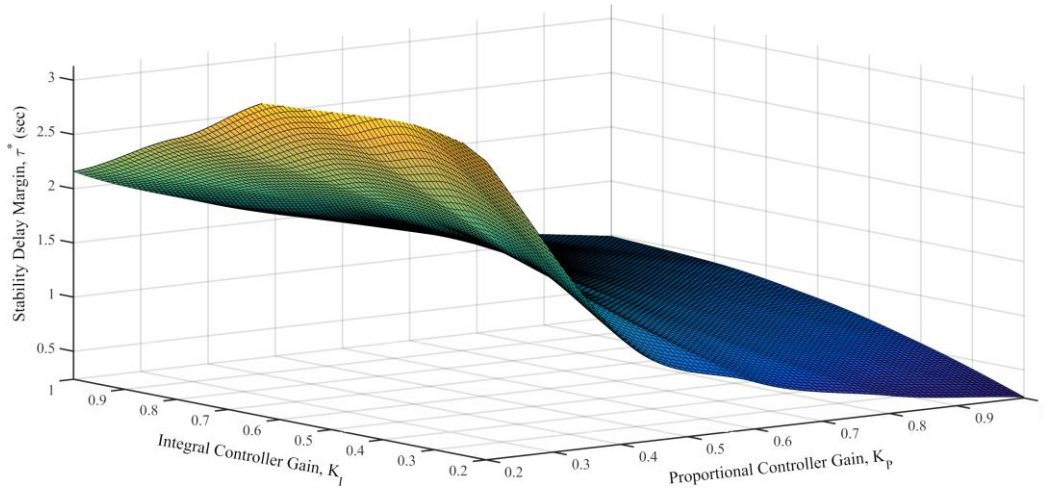

Figure 7. Variation of stability margins with respect to controller gains for $\theta = 60^0$.
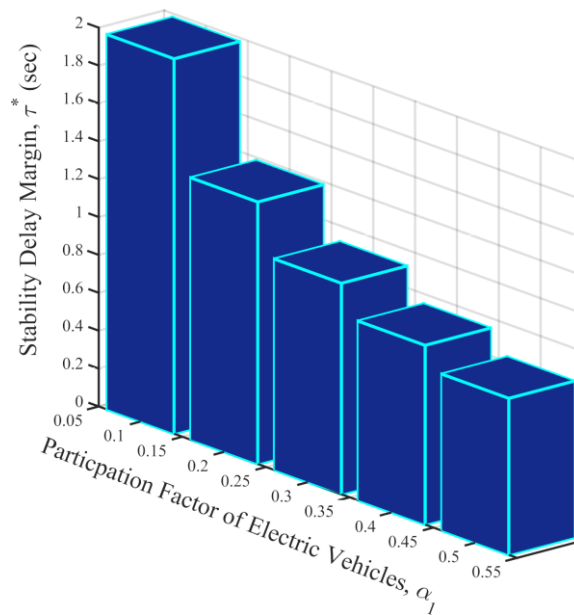

Figure 8. Variation of stability margins with respect to participation of EVs for $\theta = 60^0$.

6. CONCLUSION

A simulation based approach is presented in this work to identify stability margins over an extensive range of PI controller gains in the single-area LFC system with plug-in EVs and multiple communication delays. The technique is effectively implemented for both commensurate and incommensurate time delays. It is observed that communication delays arise due to the integration of EVs into the LFC system that leads to the destabilization of the system when the delay value exceeds the stability margin. It can be seen from the table that for a fixed K_P value, stability margin is decreasing with an increase in K_I values. Also, the delay margins initially increase and then start to decrease with an increase in K_P value when K_I is fixed. Moreover, the stability margin decrease when the participation of EVs increases. For future studies, this delay dependent stability analysis would be extended to multi-area LFC-EVs system considering uncertainties in the system parameters.

A. Naveed, Ş. Sönmez, S. Ayasun

ACKNOWLEDGEMENT

REFERENCES

[1]   W. Kempton and S. Letendre, "Electric vehicles as a new power source for electric utilities," *Transportation Research Part D.*, vol. 2, Sep., pp.157-175, 1997.

[2]   J. Pillai and B. Bak-Jensen, "Integration of vehicle-to-grid in the western Danish power system," *IEEE Transactions on Sustainable Energy*, vol. 2, Jan., pp. 12-19, 2011.

[3]   Y. Mu, J. Wu, J. Ekanayake, N. Jenkins, and H. Jia, "Primary frequency response from electric vehicles in the Great Britain power system," *IEEE Transactions on Smart Grid*, vol. 4, Jun., pp. 1142-1150, 2013.

[4]   C. Guille and G. Gross, "A conceptual framework for the vehicle-to-grid (V2G) implementation," *Energy Policy*, vol. 37, Nov., pp. 4379-4390, 2009.

[5]   S. Han, S. Han, and K. Sezaki, "Development of an optimal vehicle-to-grid aggregator for frequency regulation," *IEEE Transactions on Smart Grid*, vol. 1, Jun., pp. 65-72, 2010.

[6]   H. Jia, X. Lia, Y. Mu, C. Xu, Y. Jiang, X. Yu, J. Wu, and C. Dong, "Coordinated control for EV aggregators and power plants in frequency regulation considering time-varying delays," *Applied Energy*, vol. 210, Jan., pp. 1363-1376, 2018.

[7]   R. J. Bessa and M. A. Matos, "The role of an aggregator agent for EV in the electrical market," in Proc. 7th MedPower Conf., Nov., pp. 1-9, 2010.

[8]   K. S. Ko and D. K. Sung, "The effect of EV aggregators with time-varying delays on the stability of a load frequency control system," *IEEE Transactions on Power Systems*, vol. 33, Jan., pp. 669 - 680, 2018.

[9]   T. N. Pham, H. Trinh, and L. V. Hien, "Load frequency control for power systems with electric vehicles and diverse transmission links using distributed functional observers," *IEEE Transactions on Smart Grid*, vol. 7, Jan., pp. 238-252, 2016.

[10]   K. E. Walton and J. E. Marshall, "Direct method for TDS stability analysis," IEE Proceeding Part D, vol. 134, Mar., pp. 101–107, 1987.

[11]   Q. Xu, G. Stépán, and Z. Wang, "Delay-dependent stability analysis by using delay-independent integral evaluation," *Automatica*, vol. 70, Aug., pp. 153–157, 2016.

[12]   C. Dong, H. Jia, Q. Xu, J. Xiao, Y. Xu, P. Tu, P. Lin, X. Li, and P. Wang, "Time-delay stability analysis for hybrid energy storage system with hierarchical control in DC micro-grids," *IEEE Transactions on Smart Grid*, vol. 9, Jun., pp. 6633-6645, 2017.

[13]   J. Chen, G. Gu, and C. N. Nett, "A new method for computing delay margins for stability of linear delay systems," *System and Control Letters*, vol. 26, Sep., pp. 107-117, 1995.

[14]   Z. V. Rekasius, "A stability test for systems with delays," Proc. Joint Automatic Control Conference, San Francisco, CA, USA, Paper No. TP9-A, Aug., pp. 13-15, 1980.

[15]   N. Olgaç and R. Sipahi, "An exact method for the stability analysis of time-delayed linear time-invariant (LTI) systems," *IEEE Transactions on Automatic Control*, vol. 47, May, pp. 793-797, 2002.

[16]   L. Pekař and Q. Gao, "Spectrum analysis of LTI continuous-time systems with constant delays: A literature overview of some recent results," *IEEE Access*, vol. 6, Jul., pp. 35457–35491, 2018.

[17]   Ş. Sönmez, S. Ayasun, and C. O. Nwankpa, "An exact method for computing delay margin for stability of load frequency control systems with constant communication delays," *IEEE Transactions on Power Systems*, vol. 31, Jan., pp. 370-377, 2016.

[18]   A. Naveed, Ş. Sönmez and S. Ayasun, "Identification of Stability Delay Margin for Load Frequency Control System with Electric Vehicles Aggregator using Rekasius Substitution," 2019 *IEEE Milan PowerTech*, Milan, Italy, Jun., pp. 1-6. 2019.

[19]   L. Jiang, W. Yao, Q. H. Wu, J. Y. Wen, and S. J. Cheng, "Delay-dependent stability for load frequency control with constant and time-varying delays," *IEEE Transactions on Power Systems*, vol. 27, May, pp. 932–941, 2012.

[20]   J. M. Thangaiah and R. Parthasarathy, "Delay-dependent stability analysis of microgrid with constant and time-varying communication delays," *Electric Power Components and Systems*, vol. 44, Jun., pp. 1441–1452, 2016.

[21]   A. Naveed, Ş. Sönmez and S. Ayasun, "Stability Analysis of a Single-Area Load Frequency Control System with Electric Vehicles Group and Communication Time Delays," International Turkic World Congress on Science and Engineering (UTUFEM), Nigde, Turkey, Jun., pp.897-996, 2019.

[22]   Simulink, Model-Based and System-Based Design, Using Simulink. Natick: MathWorks, 2000.

DETERMINATION OF STABILITY MARGINS IN SINGLE AREA LOAD FREQUENCY CONTROL SYSTEM HAVING INCOMMENSURATE COMMUNICATİON DELAYS DUE TO PLUG-IN ELECTRIC VEHICLES

[23] K. Ko and D. K. Sung, "The Effect of cellular network-based communication delays in an EV aggregator's domain on frequency regulation service," *IEEE Transactions on Smart Grid*, vol. 10, no. 1, Jan., pp. 65-73, 2019.

[24] E. Yao, V. W. Wong and R. Schober, "Robust frequency regulation capacity scheduling algorithm for electric vehicles," *IEEE Transactions on Smart Grid*, vol. 8, no. 2, Mar., pp. 984–997, 2017.

[25] A. Naveed, Ş. Sönmez and S. Ayasun, "Stability Regions in the Parameter Space of PI Controller for LFC System with EVs Aggregator and Incommensurate Time Delays," 2019 1st Global Power, Energy and Communication Conference (IEEE-GPECOM), Nevsehir, Turkey, Jun., pp. 461-466, 2019.

LabVIEW BASED TEMPERATURE CONTROL SYSTEM FOR NEONATAL INCUBATOR

Zaid H. Al-Sawaff[1,2,*] iD, **Yahya Zakariya Yahya[3]** iD, **Fatma Kandemirli[4]** iD

[1] Department of Materials Science and Engineering, Faculty of Engineering and Architecture, Kastamonu University, Kastamonu, Turkey.
[2] Department of Medical Instrumentation Technology, Technical Engineering College, Northern Technical University, Mosul, Iraq.
[3] Auckland Bioengineering Institute, The University of Auckland, Auckland, New Zealand.
[4] Biomedical Engineering Department, Faculty of Engineering and Architecture, Kastamonu University, Kastamonu, Turkey.

ABSTRACT

This system used to monitor and control the sudden change in temperature in neonatal incubator depending on two parts: first is the microcontroller which is a compact integrated circuit designed to run a specific operation in an embedded system, and LabVIEW which is engineering software used for applications that require test, measurement, and control with rapid access to hardware and data insights. those two important parts along with other components (heaters, fans, data acquisition cards) will be used to design the desired system.

This system has the properties of being cheap, easy to use, able to deal with many units as possible at the same time and finally can be operated automatically or by one person. this system will give a temporary solution for a period of time till the responsible person would fix the main problem.

Keywords: Neonatal incubator; LabVIEW; Microcontroller; Temperature control system; Embedded system

1. INTRODUCTION

According to the WHO report in 20216 [1], The first 28 days of their life is the most in danger time for a child's survival, which called the neonatal period, where globally almost 2.6 million children die in the first month of life, with roughly 7,000 newborns dying daily, most occur within the first week of their life.

In developing countries, because the economic situation is very low; the cost of medical devices should be kept low. so there is a need to develop low-cost incubators with monitoring and control which provides the facilities required for the infants[2].

Al-Sawaff Z. H. et al [3] designed a fully automated monitoring system for neonatal incubators by using a new generation of microcontrollers and GSM systems for pre-warning the change of temperature at a fixed setpoint using the (LT35) thermos sensor [4]-[5].

Mathew et al. [6] described the design and implementation of a fully digital and programmable temperature system for the Baby Incubator. The transmitter circuits were also designed and implemented for all the variables of the incubator that are used as control signals like the air temperature sensor (thermistor), baby skin temperature sensor (probe) [7]-[8].

The neonatal incubator is a piece of equipment commonly used in pediatric hospitals, birthing centers, and neonatal intensive care units. although the unit may serve several specific functions, it is generally used to provide a safe and stable environment for newborn infants, especially for those who were born prematurely or with an illness or disability that makes them especially vulnerable for the first several months of their life [9].

The main process of the incubator is to produce healthful micro-environment in order to reduce newborn's (heat loss, humidity, and oxygen levels) by controlling the temperature inside the incubator with other important parameters like humidity and oxygen levels [10]. Temperature is one of the most important factors which needed to be maintained with minimum changes. But only temperature control is not enough to provide a comfortable decision about the environment [11].

A neonatal incubator Fig. 1, consists of a rigid box built-in fiber and steel, where an infant may be kept in a controlled environment for medical care.

The device includes an AC-powered heater, an electrical motor fan to circulate the warmed air, a water container to add humidity, a mechanical filter through which the oxygen flows, and an access port for nursing care; The electric motor allows the air to circulate into the neonatal incubator through an air inlet at the bottom of the equipment [12].

Z. H. Al-Sawaff, Y. Z. Yahya, F. Kandemirli

Figure 1. Infant Incubator

The microcontroller is considered as a free hardware platform consisting of an integrated circuit through which instructions can be recorded, where these instructions are written with a special programming language that allows the user to set programs that interact with electronic circuits [13].

The Arduino is an open-source board that has all the elements used to connect peripherals to the inputs and outputs of the microcontroller. as in Fig. (2) [13].
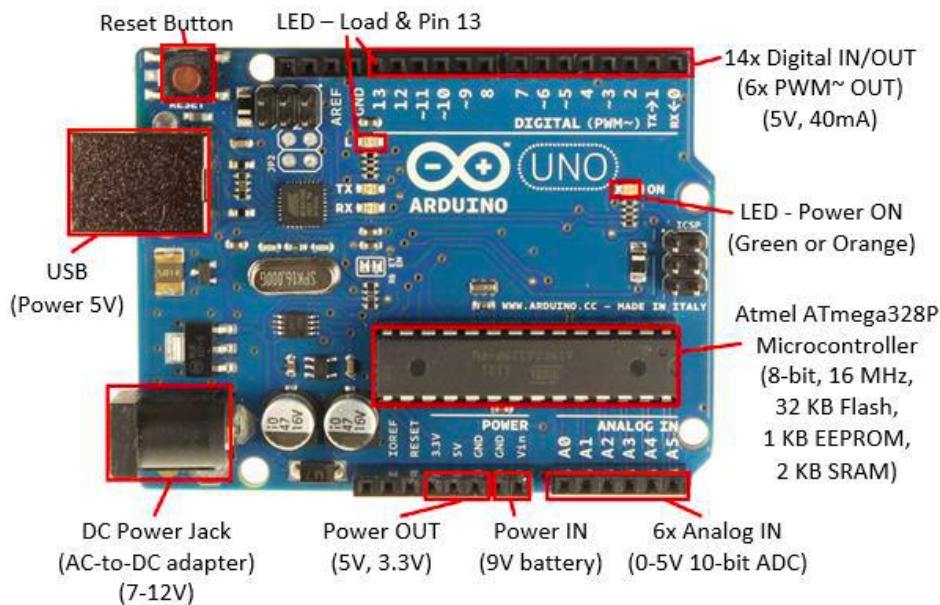

Figure 2. Arduino Uno Schematic [13]

LabVIEW is a graphical programming language that uses icons instead of lines of text to create applications. In contrast to text-based programming languages, where instructions determine program execution, LabVIEW uses dataflow programming, where the flow of data determines execution [14]. LabVIEW can build a user interface program with a set of tools and objects. The user interface program is known as the front panel. then adding codes using graphical representations of functions to control the front panel objects [15].

LabVIEW [16], which is stands for Laboratory Virtual Instrumentation Engineering Workbench, is a graphical computing environment for instrumentation, system design, and signal processing. LabVIEW is a development environment that has been

LabVIEW BASED TEMPERATURE CONTROL SYSTEM FOR NEONATAL INCUBATOR

built specifically for engineers and scientists with the intent of making them more productive and ensuring that they have all the tools they need to prototype, design, and build their applications. LabVIEW makes users more productive because it provides all the tools engineers need in a single environment and ensures that they all work and can be used together. The key is guaranteed compatibility between engineering tools.
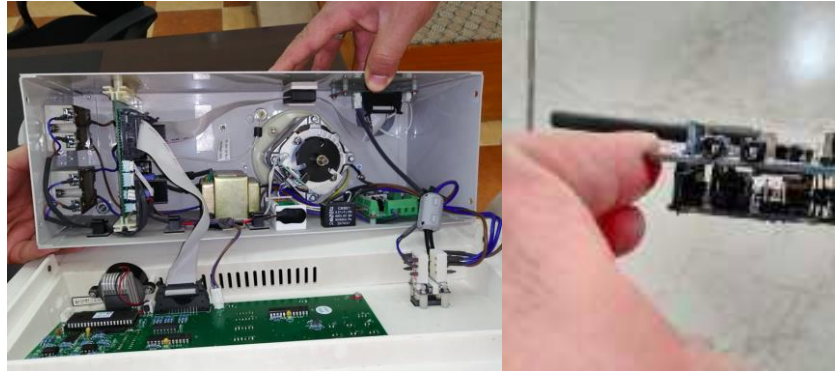

Figure 3. System electronic parts of the tested incubator along with the microcontroller

Fig. (3) shows the electronic parts of the tested neonatal incubator along with the microcontroller attached to it, where the figure shows the location of the microcontroller would be added inside the incubator.

The use of a microcontroller with the help of the LabView program made the monitoring and controlling very easy and fast in comparison with the ordinary method using only the control system already came with the incubator, and could be considered as a second control unit for more safety.

The layout and also the execution approach defines the procedure's ingredients of the mooted system along with the interactions between these ingredients. The circuit diagram representation of the developed model is shown in Fig. 4. The scope of normal values is set before the system starts taking any readings, where all the ingredients required to take the readings of the temperature are initialized, then the monitoring system now starts its work in an unending loop until it is manually halted. The mooted system will read the temperature in analog data, then the analog to digital converter (ADC) will convert these data to digital format, then converted format will be compared to the present values [17].

If the read value is within the present scope the value will be transmitted to the local server where it will be displayed in tabular format and display results. If the read value is outside the scope, a warning is sent to the doctor and the nurses, with sound alarm in the incubator [18].

At the same time, a warning signal will be sent to the LabView control system, this system will check the change of the temperature according to the set point which already been adjusted; the program will decide if there was a decrease or increase of the temperature then it will give the suitable order to start the fan or the heater till the temperature reaches to the same value of the set point [19].

The LabView program will give the right solution which will help to minimize the risk on the infant until the in-charge person fixes the whole problem.
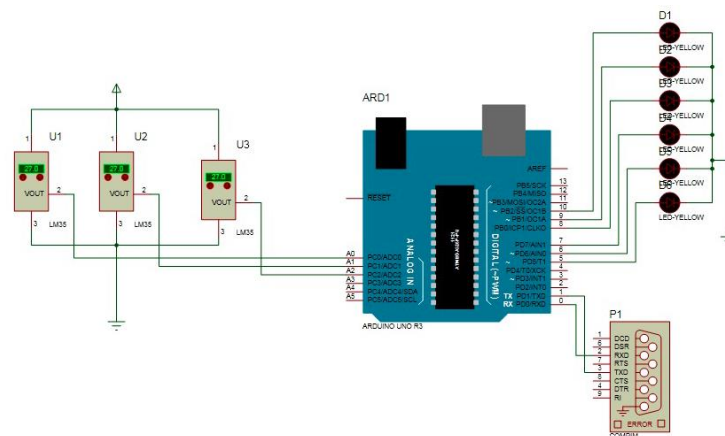

Figure 4. Microcontroller system block diagram

Z. H. Al-Sawaff, Y. Z. Yahya, F. Kandemirli

After completion of signals acquisition and comparison with preset values, the microcontroller then constructs the SMS messages as well as emails and packs the data samples in these messages to the desired length, it then communicates with the mobile phone using at-commands on its serial port to send the message(s). The device records temperature data continuously. When a temperature reading exceeds the present values, an alarm is triggered, and an email and an SMS message was sent to the in-charge doctor, then, the measured values are sent to the local web server and displayed on the website of the hospital in a tabular format; this assists the doctor(s) in taking correct decisions based on the accurate data; as shown in the flowchart below (Fig. 5). the connection between the Arduino monitoring system and LabView controlling system will be done in wireless connection mode, this mode will give many advantages for the system like less wiring and fast response.
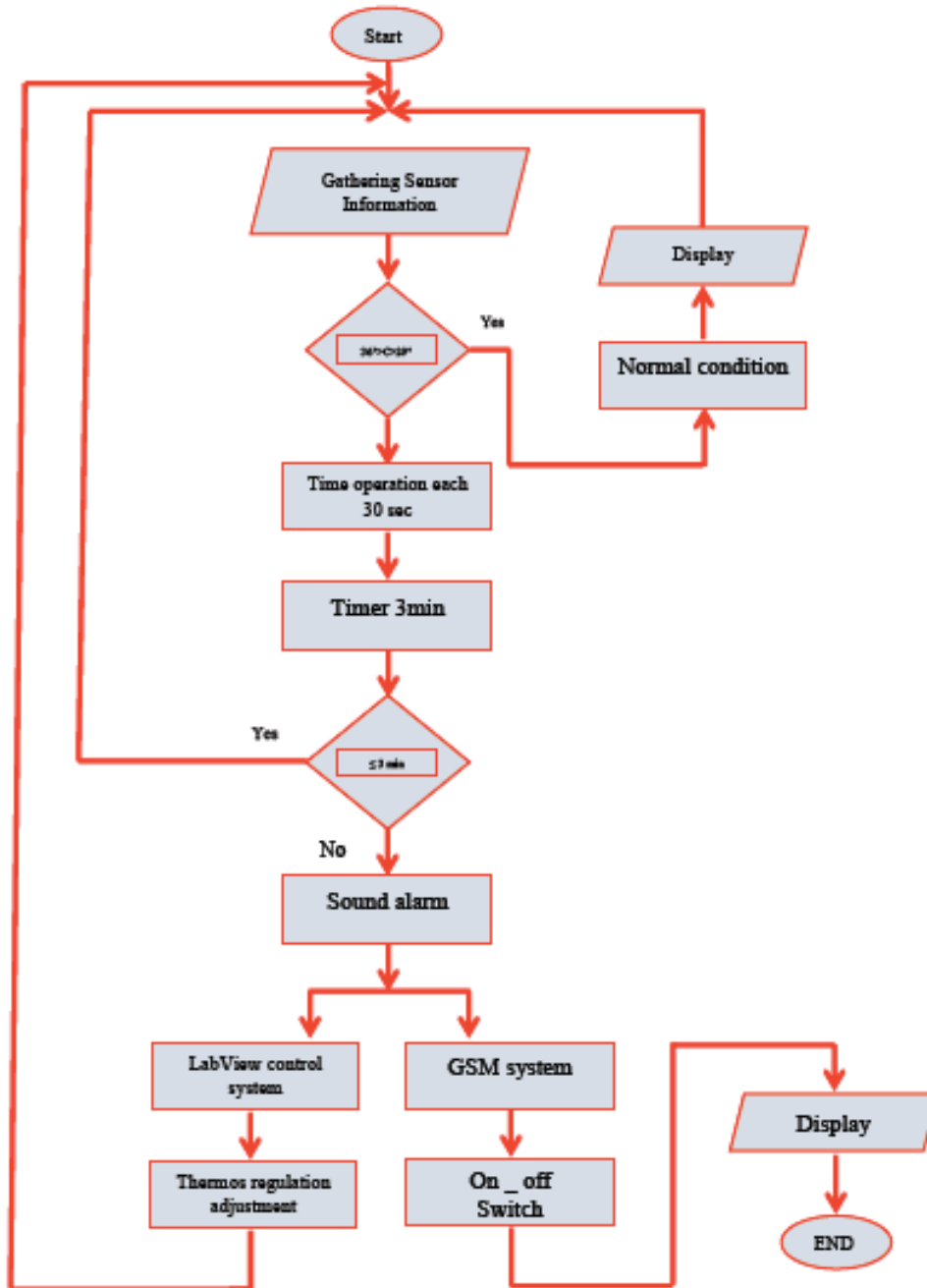

Figure 5. System flowchart

LabVIEW BASED TEMPERATURE CONTROL SYSTEM FOR NEONATAL INCUBATOR

2. RESULTS AND CONCLUSIONS

The results obtained were tested and confirmed under normal temperature and dustless environment and agreed with the expected results which were displayed on the (LCD) attached with the controlling system.

The results obtained were compared and tabulated as shown in Table 1. which shows the results taken by using the original monitoring system found in the incubator and compared with the results and readings taken from the tested control system established by the microcontroller and the LabView programming system.

From the result, it was seen that there was little or no variation in the patient's readings from the clinical thermometer and all monitored units.

The system was designed to deal with only three units of neonatal incubators, the tests were done for seven samples (Table 1) under normal conditions (samples: A, B, D, and I) and different conditions (Samples: C, E, and F) to see the speed or the fast response of the alarm system along with the new tested device.

From these 7 samples, only three ideal results were taken (Samples A, B, and D) to make the final system

It's worth mentioning that the results obtained from the incubator were done under normal conditions and with the help of a dummy patient which provided with the needed tools and sensors for temperature under the same conditions of the actual patients.

Table 1. Readings results comparison between the incubator thermos sensor and the microcontroller sensor

Subject	Readings from Clinical Thermometer (C°)	Readings from infant body using microcontroller sensor (C°)
Sample A	33.6	34.1
Sample B	36.5	37.5
Sample C	35.6	35.4
Sample D	37.1	37.9
Sample E	38	37.6
Sample F	34.4	33
Sample I	39.2	36.8

A controlling system using the microcontroller and LabView system were used to ease the work of doctors in hospitals suffering from less number of staff, and in remote areas. The designed system was capable of helping the medical staff to make the right decision at the right time. The system is also appropriate for the monitoring of day-to-day activities in places like server rooms, hospital rooms, etc.

From the results were taken practically from different patients, the accuracy of the designed system was acceptable and the efficiency of the system was very high.

The designed system is very easy to use and manufacture, and the cost of manufacturing is rather reasonable, on the other hand, the size of the designed system is small and can be reduced to a minimum size depending on the size of the microcontroller used.

This system was designed to monitor and control more than one infant incubator at the same time (in our case three infant incubators were used), the total number we can control using this system can be increased till 10 units all controlled with the same LabView program as in Fig.5 and Fig.6.
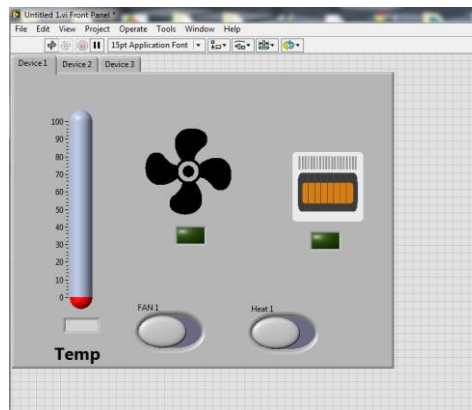

Figure 5. LabView system control panel

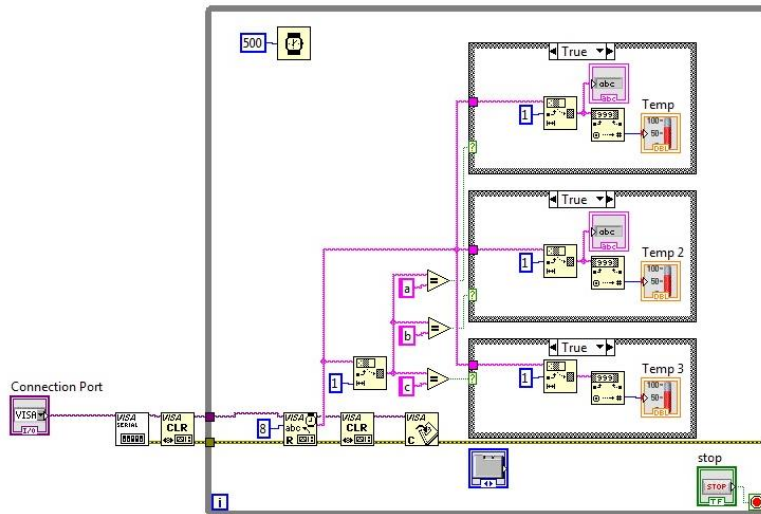*Z. H. Al-Sawaff, Y. Z. Yahya, F. Kandemirli*

Figure 6. 3-units control system

As a future scope, different types of sensors can be added to monitor and control other variables like Humidity, oxygen levels, and Atmospheric pressure values, which are very easy and suitable for the microcontroller used in this system due to the presence of suitable sensors with less error.

REFERENCES

[1] M. O. F. Health, "Ministry of Health Neonatal Care Clinical Guidelines," 2018.

[2] P. McDougall and R. Hunt, "Neonatal Conditions," Paediatr. Handb. Eighth Ed., pp. 431–451, 2009.

[3] Z. H. Al-Sawaff, Y. Z. Yahya, and F. Kandemirli, "Neonatal Incubator Embedded Temperature Observation and Monitoring Using GSM," *J. Eng. Res. Reports*, vol. 4, no. 1, pp. 1–9, 2019.

[4] O. H. Jimmoh, S. Adedayo, O. S. Enemakwu, and I. N. Ajibola, "Microcontroller-Based Remote Temperature Monitoring System," *IOSR J. Comput. Eng.*, vol. 18, no. 04, pp. 68–72, 2016.

[5] F. Peeters, M. Peetermans, and L. Indesteege, "Temperature Sensors," Mod. Sensors Handb., pp. 347–393, 2010.

[6] H. B. D. L. Mathew, Ashish Gupta, "Controlling of Temperature and Humidity for an Infant Incubator Using Microcontroller," *Int. J. Adv. Res. Electr. Electron. Instrum. Eng.*, vol. 04, no. 06, pp. 4975–4982, 2015.

[7] T. A. Tisa, Z. A. Nisha, and M. A. Kiber, "Design of an Enhanced Temperature Control System for Neonatal Incubator," *Bangladesh J. Med. Phys.*, vol. 5, no. 1, pp. 53–61, 2013.

[8] Manual, U. (2011). User Manual. Springer Reference, (320999).

[9] H. B. D. L. Mathew, Ashish Gupta, "Controlling of Temperature and Humidity for an Infant Incubator Using Microcontroller," *Int. J. Adv. Res. Electr. Electron. Instrum. Eng.*, vol. 04, no. 06, pp. 4975–4982, 2015.

[10] N. Elsheikh and B. Mohammed, "Design and Development of Microcontroller Based Temperature and Humidity Controller for Infant Incubator OK," vol. 2, no. July, pp. 78–89, 2011.

[11] T. K. Ferris and M. M. Shepley, "The design of neonatal incubators: A systems-oriented, human-centered approach," J. Perinatol., vol. 33, no. SUPPL. 1, pp. S24–S31, 2013.

[12] D. Ibrahim, "Introduction to Microcontrollers and Display Systems," Using LEDs, LCDs GLCDs Microcontroller Proj., no. July 2017, pp. 1–16, 2012.

[13] M. M. Mijwel, "What is Arduino Programming," no. March, 2018.

[14] A. Nayyar, "An Encyclopedia Coverage of Compiler's, Programmer's & Simulator's for 8051, PIC, AVR, ARM, Arduino Embedded Technologies," *Int. J. Reconfigurable Embed. Syst.*, vol. 5, no. 1, p. 18, 2016.

[15] M. L. Higa, D. M. Tawy, and S. M. Lord, "An introduction to labview exercise for an electronics class," Proc. - Front. Educ. Conf., vol. 1, no. February 2002, 2002.

[16] J. Kang, F. She, F. Yang, and T. Wang, "Design of instrument control system based on LabView," Proc. - 2011 7th Int. Conf. Comput. Intell. Secur. CIS 2011, vol. 11, no. 6, pp. 1479–1483, 2011.

[17] B. Oyebola, "Development of a Microcontroller Based Temperature and Humidity Controller for Infant Incubator," *J. Ind. Technol.*, vol. 2, no. January, pp. 78–89, 2017.

LabVIEW BASED TEMPERATURE CONTROL SYSTEM FOR NEONATAL INCUBATOR

[18] M. Suruthi and S. Suma, "Microcontroller Based Baby Incubator Using Sensors," pp. 12037–12044, 2015.

[19] T. Murugan, A. Periasamy, and S. Muruganand, "Embedded based Industrial Temperature Monitoring Systems using GSM," *Int. J. Comput. Appl.*, vol. 58, no. 19, pp. 6–11, 2012.

4-NAPHTHYL-3-THIOSEMICARBAZIDE as CORROSION INHIBITOR for COPPER in SEA WATER (3.5% SODIUM CHLORIDE)

Mothana Ghazi Kadhim ALFALAH [1,2,*] iD **, Mohammed ABDULRAZZAQ** [2] iD **,**
Murat SARAÇOĞLU [3] iD **, Fatma KANDEMIRLI** [4] iD

[1] *Metallurgy and Materials Engineering, Faculty of Engineering and Architecture, Kastamonu University, 37150, Kastamonu, Turkey*
[2] *Materials of Engineering Department, College of Engineering, University of Al-Qadissyah, 54004, Iraq*
[3] *Erciyes University, Faculty of Education, 38039 Kayseri, Turkey*
[4] *Department of Biomedical Engineering, Faculty of Engineering and Architecture, Kastamonu University, 37150, Kastamonu, Turkey*

ABSTRACT

The effects of 4-NaTh-3-Thıosemicarbazide on the corrosion of Copper immersed in sea water has been evaluated. The inhibitor efficiency was determined by using three electrochemical techniques, Potential dynamic polarization (PDP), Impedance spectroscopy (EIS), and Open Circuite Potential (OCP) by using Potentiostat Instrument type compact stat (IVIUM) after immersion in sea water contain 3.5% Sodium chloride with presence and without corrosion inhibitor. A good inhibition efficiency is noticed which increases with an increase in corrosion inhibitor concentration. It was obtained that the inhibitor efficiency reached around 95% at 0,001 M from corrosion inhibitor. Both the cathodic and anodic curves are changed markedly in the presence of 4-NaTh-3-Thıosemıcarbazide. The mechanism of inhibition was proposed along the basis of the adsorption of the inhibitor molecules on the copper surface.

1. INTRODUCTION

Copper and its alloys are commonly used in manufacturing applications owing to its perfect properties, such as higher electrical conductivity and high thermal conductivity, mechanical strength and durability [1]-[2]. It is understood that the application of copper in a corroded atmosphere induces its corrosion and disintegration [3]-[4]. The investigation, which is the most suitable solution to protecting copper from degradation, also sets that as a concern. Given the past work carried out by various authors, the use of organic compounds is the most competent and financial tool for this reason [5]-[6]. These days' organic compounds are being investigated in different reactive applications as metal corrosion inhibitors [7]-[8]. Many of them are nevertheless toxic and harmful for the environment. Global work is undertaken to find a successful source of corrosion that is biodegradable and non-toxic to the ecosystem. In recent years, the use semicarbazide products (semicarbazones and thiosemicarbazones) are known to have an activity of antiviral, anti-infective and antineoplastic through binding to copper or iron in cells. Semicarbazide is used in preparing pharmaceuticals including nitrofuran antibacterial (furazolidone, nitrofurazone, nitrofurantoin) and related compounds. Thiosemicarbazide and its derivatives are used as corrosion inhibitors for different metallic substrates [9]. Corrosion inhibitors are chemical agents that are commonly used in corrosion systems to guard against degradation of materials. By forming a protective film on the copper surface and reducing the entry of aggressive ions into the concrete matrix, corrosion inhibitors offer protection. Throughout the following sequence are the inhibition capacity of homologous series of organic compounds, including different heteroatoms; P > Se > S > N > O [10]. Potential targets were identified to be other amides and derivatives such as urea (U), thiourea (TU), thioacetamide (TA), and thiosemicarbazide (TSC).

Thiosemicarbazide has been observed to be a potential inhibitor for different metals among various nitrogen and sulphur containing compounds. It has also been confirmed that its inhibitive performance can be significantly enhanced by its derivatives' (Fig.1) with certain aromatic compounds [11]. The very comportment of thiosemicarbazide and its derivatives products has opened a new avenue to examine the applicability for aqueous chloride systems of such compounds as corrosion inhibitors for copper.

The goal of this research was to investigate 4-Naphthyl-3-Thiosemicarbazide in sodium chloride solution as a corrosion inhibitor for copper by using electrochemical techniques of impedance spectroscopy, potentiodynamic polarization, and open circuit potential. All electrochemical techniques were used to calculate the inhibition efficiency of the inhibitors.

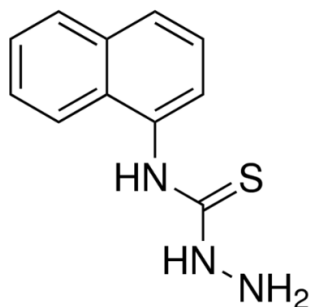*M. G. K. Alfalah, M. Abdulrazzaq, M. Saraçoğlu, F. Kandemirli*

Figure.1 Structure of 4-Naphthyl-3-Thiosemıcarbazide

2. MATERIAL AND METHOD

Cylindrical specimens with a diameter of 0.75 cm were prepared from electrolytic copper (99.9 per cent) and used in the absence and presence of corrosion inhibitors to investigate copper corrosion. The specimens were bound by copper wire from the back, after which they were mounted in epoxy resin with an exposed surface of 0.44 cm^2 (Fig.2). Specimens have been polished using silicon carbide paper successively starting from 600 to 2400 grits to obtain a mirror like a finish. After polishing, the specimens were washed thoroughly with distilled water and dried with hot air.

4-NaTh-3-thiosemcarbazied has been selected and tested as a corrosion inhibitor. The chemically pure compound has been purchased from the Sigma Aldrich Company.

All electrochemical measurements were carried out using a COMPACTSTAT (IVIUM) type electrochemical analyzer instrument, as shown in Figure 3. For performing electrochemical tests three electrode corrosion cells made from 100 mL beaker glass size were used. The working electrode was the copper sample with 0.44 cm^2, a platinum wire was used as the counter electrode, while silver chloride (Ag / AgCl) was used as the reference electrode. All plots have been fitted to 1 cm^2.

Potentiodynamic polarization Copper sample measurements submerged in 3.5 per cent NaCl solution without and inside corrosion inhibitors were performed at a scan rate of 60 mV / min at room temperature. The potential started from a cathodic potential (-0.465 V) against corrosion potential (E_{corr}) and was allowed to sweep in anodic direction up to (0.035) volt above the E_{corr} and the potential scan was reversed to a potential E_{corr} equals. Corrosion parameters: corrosion current (I_{corr}), corrosion potential (E_{corr}) and corrosion rate (CR) were derived from the analysis of polarization plots using the IVIUM software.

The technique of **electrochemical spectroscopy (EIS)** was used to measure the corrosion activity of the copper samples without and inside corrosion inhibitors. Experiments were conducted at room temperature between 10 mHz and 65000 Hz at open-circuit potential over the frequency range. The voltage signal amplitude was 10 mV.
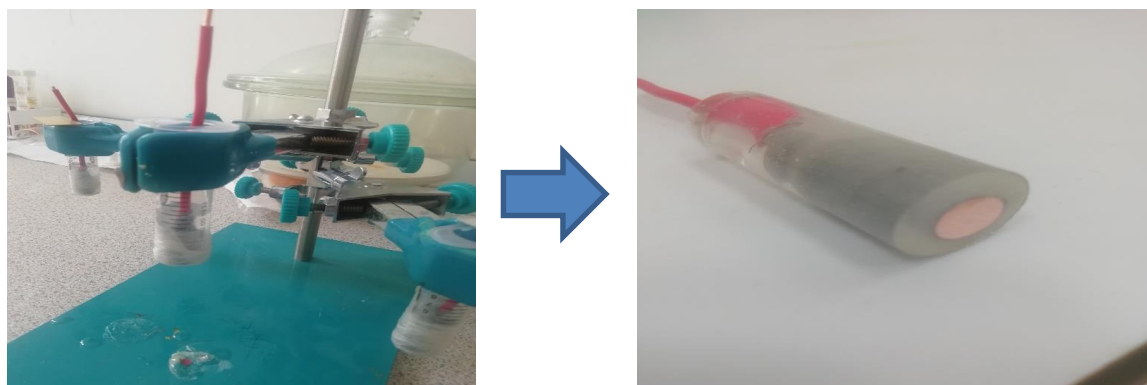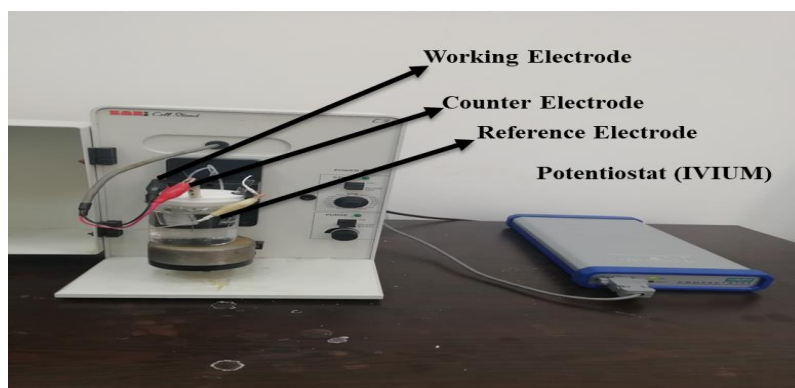

Figure 2. Sample preparation

4-NAPHTHYL-3-THIOSEMICARBAZIDE as CORROSION INHIBITOR for COPPER in SEA WATER (3.5% SODIUM CHLORIDE)

Figure 3. Potentiostat (IVIUM) and Electrochemical cell

3. RESULTS AND DISCUSSION

Fig.4 showed the open circuit potential for copper in 3.5 per cent NaCl, with and without inhibitor concentration. From figure (4) it can be seen that at the beginning of immersion time the value of the open circuit potential is shifted towards less negative meaning, which is believed to be the oxide layer due to figuration. After that, as the duration of immersion increases the value of the open-circuit potential decreases due to the breakdown of copper oxide by reaction as seen below and the creation of CuCl [12].

$$Cu + Cl^- \longrightarrow CuCl_{ads} + e^- \tag{1}$$

In addition, it can be seen from Figure (3) that the existence of an inhibitor changed the open-circuit potential to less negative at the end of the experiment due to adsorption molecules on the active part of copper that contribute to the defense of the copper surface at the ingress of Cl-ion.

$$M \longrightarrow M^{+2} + 2e \tag{2}$$

$$M + Inh_{ads} \longrightarrow [M - Inh]_{ads}^{2+} \tag{3}$$

Experiments of potentiodynamics polarization were used after the open circuit potential measurements were done. Potential for corrosion (E_{corr}), anodic (ba) and cathodic (bc) Tafel slopes, existing corrosion density ($I_{cor.}$) and inhibition capacity (IE%) were all measured and described in Table (1).

From Fig.5, it can be observed that when the concentration of inhibitors increased, the current density is reduced due to adsorption of inhibitor molecules on the copper surface. The adsorption of inhibitor molecules on the surface makes physical barrier to the mass and charge transfer, giving a high level of protection to the copper surface by hindering the active sites on the copper [13]. In addition, corrosion of potential marginally modified to less negative due to influence of inhibitor concentration and expected adsorption of the inhibitor molecules on the copper surface. It can also be seen from Fig.5 that both anodic and catholic curves shift dramatically with the inhibitor presence. The corrosion inhibitor can be classified as mixed type inhibitor due to shift E_{Corr} to lower than 0.085 V. The maximum displacement in the E_{Corr} with presence inhibitor was 0.04 V [14],[15],[16].

Nyquist and Bode graphs are seen from electrochemical impedance spectroscopy in figure (6), figure (7) respectively. It can be noticed from Fig.6 Nyquist curve for copper without inhibitor contain fading semicircular in the high frequency which is refer to the rudeness and inhomogeneity of electrode [17], while at low frequency the shape of plot is changed to straight line due to the diffusion of soluble copper species from copper surface to bulk solution [17]. Besides Fig.6 the diameter of the semicircle becomes larger with the presence of corrosion inhibitor due to the protection of the surface by corrosion inhibitor molecules can be noticed. From Fig.7 displays Bode graph, the phase angle can be seen increasing with a rise in the inhibitor concentration.

M. G. K. Alfalah, M. Abdulrazzaq, M. Saraçoğlu, F. Kandemirli
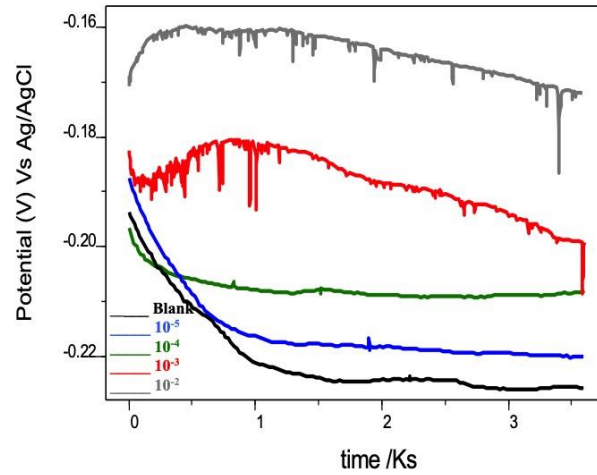
Figure 4. The open circuit potential of copper in 3.5% NaCl solution without and with the addition of different concentrations 4- NaTh-3-TSC

Table 1. Electrochemical parameters of copper corrosion in 3.5% NaCl without and with the addition of different concentrations of 4- NaTh-3-TSC

Conc.Inh.(M)	$E_{corr, V vs Ag/AgCl}$	j_{corr}, $\mu A/cm2$	ba, V/dec	bc,V/dec	$CR_{(mm/year)}$	EI%
Blank	-0.250	8.5	0.068	0.27	0.11	----
10^{-5}	-0.245	6.8	0.047	0.289	0.085	20
10^{-4}	-0.232	1.8	0.065	0.258	0.02	78.8
10^{-3}	-0.224	1.1	0.072	0.298	0.01	87
10^{-2}	-0.210	0.817	0.091	0.295	0.009	90.3
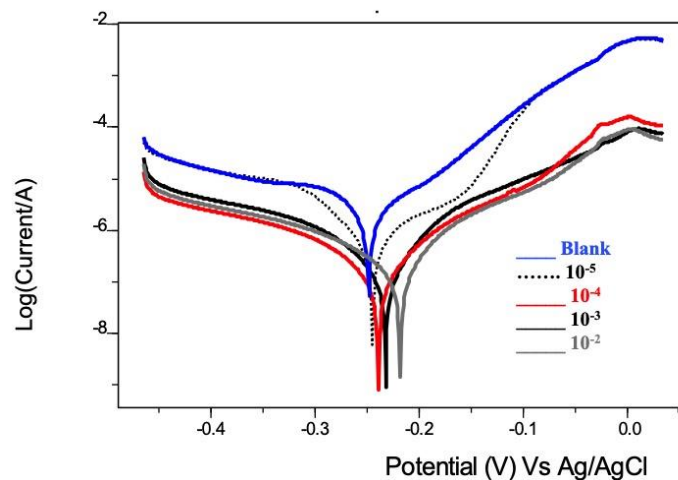
Figure 5. Potentiodynamic polarization curves of copper in 3.5% NaCl   solution without and with the addition of different concentrations of 4- NaTh-3-TSC

4-NAPHTHYL-3-THIOSEMICARBAZIDE as CORROSION INHIBITOR for COPPER in SEA WATER (3.5% SODIUM CHLORIDE)

Figure 6. EIS diagrams for copper in 3.5% NaCl in the presence of different concentrations of 4-NaTh-3-TSC Nyquist plots

Figure 7. EIS diagrams for copper in 3.5% NaCl in the presence of different concentrations of 4-NaTh-3-TSC Bode phase angle and Bode modules.

Figure 8. Equivalent circuit corresponding to fitted Electrochemical Impedance Spectroscopy data.

M. G. K. Alfalah, M. Abdulrazzaq, M. Saraçoğlu, F. Kandemirli

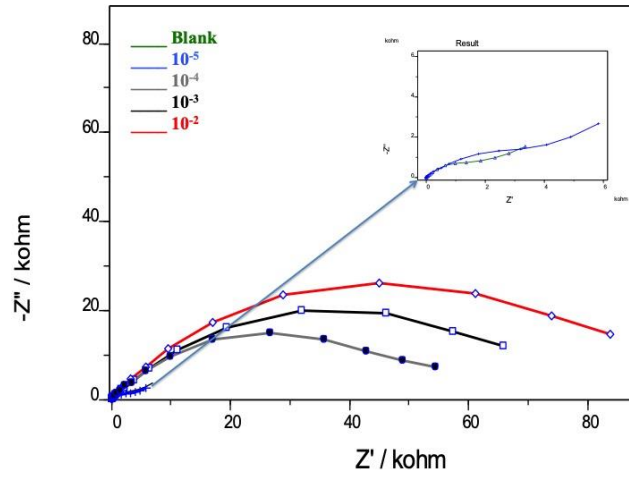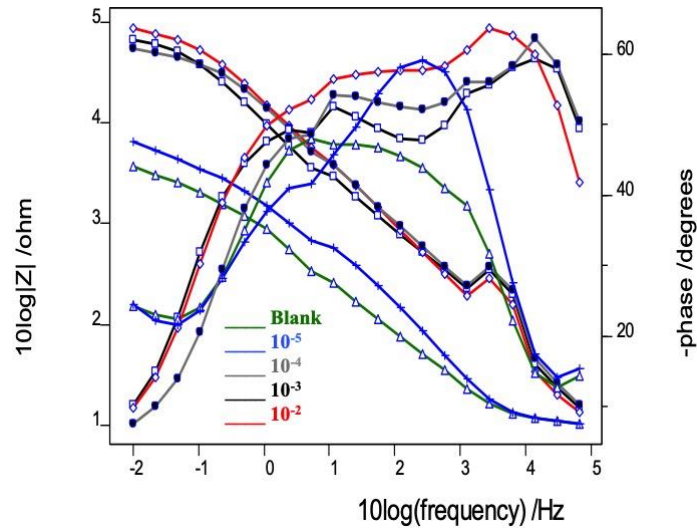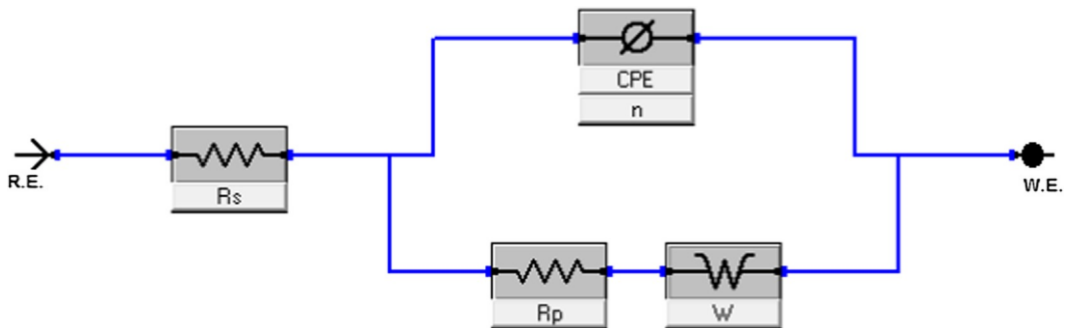**Table 2**. Electrochemical impedance spectroscopy parameters for copper in 3.5% NaCl solution without and within the addition of different concentration of 4- NaTh-3-TSC

Conc. Inh.	R_S, Ω cm2	R_P, Ω cm2	W, Ω−1 cm−2 s0.5	CPE	n	IE%
Blank	5.757E+01	3.866E+03	1.128E-03	1.25E-04	0.77	-------
10^{-5}	5.499E+01	4.254E+03	7.689E-04	1.08E-04	0.86	9
10^{-4}	3.277E+02	5.262E+04	1.064E-03	1.47E-05	0.80	92.6
10^{-3}	4.943E+02	7.231E+04	6.379E+01	2.23E-05	0.89	94.6
10^{-2}	3.300E+02	8.995E+04	1.757E-03	1.49E-05	0.82	95.7

The parameters determined from equivalent circuit fitting for electrochemical impedance spectroscopy (Fig.8) and described in table (2). The efficiency of the corrosion inhibitor was calculated using equation, as shown below:

$$\% IE = [(R_p - R_P^O) / R_p]. \ 100 \qquad (4)$$

The overall polarization resistance is R_p, R_P^O for copper electrode in the presence of a corrosion inhibitor and without the existence of corrosion, respectively. Table 2 indicates that the efficacy of the corrosion inhibitor has improved with an increase in the concentration of the inhibitor and increased the resistance of the protective inhibitor layer (R_P).

The most significant concept in the consumption inhibition cycle is the adsorption of the studied precursor to the metal surface. Diverse adsorption isotherms, including Langmuir, Frumkin, Freundlich, are frequently used to depict the inhibitor adsorption component.
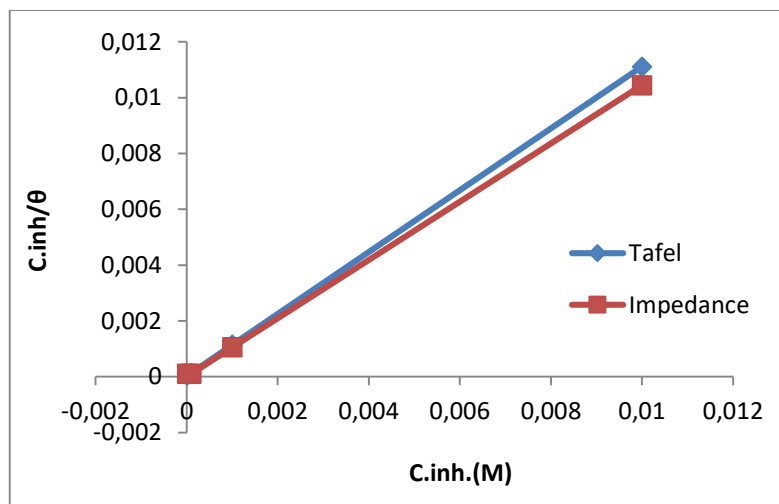
Figure 9. Langmuir adsorption isotherm of 4- NaTh-3-TSC on the copper surface.

Table 3. Langmuir adsorption parameters of 4- NaTh-3-TSC on copper surface in 3.5% NaCl solution

Method	K_{ads}	R^2	−ΔGads,kJ/mol
EIS	25000	0.99999	35.049
PDP	33333	1	35.762

4-NAPHTHYL-3-THIOSEMICARBAZIDE as CORROSION INHIBITOR for COPPER in SEA WATER (3.5% SODIUM CHLORIDE)

In this work, the Langmuir adsorption isotherm, displayed by equation as shown below, was found to be the most suitable to fit the thread-effects of potentiodynamic polarization and estimates of electrochemical impedance [18].

$$C_{inh}/\theta = (1/K_{ads}) + C_{inh} \qquad (5)$$

where C_{inh} is the concentration of inhibitor, θ is the level of surface inclusion by inhibitor and K is the equilibrium constant of adsorptive.

The got plot of C_{inh}/θ versus inhibitor fixation (C_{inh}), (Fig.9) is straight showing that the Langmuir adsorption isotherms material to portray the adsorption of 4- NaTh-TSC. Likewise, the interaction coefficient (R2) calculation states that the 4- NaTh-TSC adsorption pursues the isotherm Langmuir. Additionally, this R2 estimate demonstrates that the 4-NaTh-TSC atoms on the terminal surface shaped a monomolecular layer [19]. Furthermore, as shown below, the free adsorption vitality of the Gibbs is determined by the equation:

$$-\Delta G_{ads} = [\ln (55.55 \, K_{ads})] \times R \times T \qquad (6)$$

Where ΔG_{ads} is Gibbs free energy of adsorption, R is the molar gas constant, T the absolute temperature and 55.55 the molar concentration of water.

Table 3. Shows the value of ΔG_{ads}. The Gibbs free energy of adsorption (ΔG_{ads}) was -35.049 kJ mol^{-1} in case (EIS), while in case (PDP) Standard free energy of adsorption (ΔG^o) was -35.762 kJ mol^{-1}. The negative value of ΔG^o indicates the spontaneity of the adsorption reaction of the inhibitors on the copper surface. This also refers to chemisorption occurring in inhibitor interaction and copper surface where the exchange or move of load from the inhibitor molecules to the copper surface creates a coordinate kind of bond [20].

4. CONCLUSION

Potentiodynamic polarization, open-circuit potential and electrochemical impedance spectroscopy have been approved to use 4-NaTh-thiosemicarbazide as an effective copper corrosion inhibitor in solution comprising 3.5 % NaCl. The mechanism of the corrosion inhibitor is collected by adsorption on the copper surface and followed by the Langmuir adsorption isotherm. The higher efficacy of the corrosion inhibitor is nearly 95 % with a concentration of 10^{-2} of 4-NaTh-3-Thiosemicarbazide.

ACKNOWLEDGEMENT

REFERENCES

[1] A. Lalitha, S. Ramesh, S. Rajeswari, "Surface protection of copper in acid medium by azoles and surfactants,"*Electrochimica Acta*, vol.51, no.1, pp.47–55, (2005).

[2] A. Khiati, M. Sanchez-Moreno, M. Bernard, S. Joiret, "Corrosion inhibition of copper in neutral chloride media by a novel derivative of 1,2,4-triazole," *Corrosion Science*, vol.53, no.10, pp.3092–3099, (2011).

[3] Y.H.Wang, J.B. He, "Corrosion inhibition of copper by sodium phytate in NaOH solution:cyclic voltabsorptometry for in situ monitoring of soluble corrosion products," *Electrochimica Acta*, vol.66, pp.45–51, (2012).

[4] M. Petrovic Mihajlovic, M. Radovanovic, Z. Tasic, M. Antonijevic, "Imidazole based compounds as copper corrosion inhibitors in seawater," *Journal of Molecular Liquid*, vol.225, pp.127–136, (2017).

[5] S.K. Shukla, M.A. Quraishi, R. Prakash, "A self-doped conducting polymer "polyanthranilic acid": an efficient corrosion inhibitor for mild steel in acidic solution", *Corrosion Science*, vol.50, no.10, pp. 2867–2872, (2008).

[6] M. Lashgar, A.M. Malek, "Fundamental studies of aluminum corrosion in acidic and basic environments: theoretical predictions and experimental observations," *Electrochimica Acta*, vol.55, no.18, pp. 5253–5257, (2010).

[7] M.M. Antonijevic, S.M. Milic, M.D. Dimitrijevic,M.B. Petrovic, M.B. Radovanovic, A.T. Stamenkovic, "The influence of pH and chloride ions on the electrochemical behavior of copper in the presence of benzotriazole,"*International Journal Electrochemical Science*, vol.7, pp.962–979, (2009).

[8] M.B. Radovanović, M.M. Antonijević, "Protection of copper surface in acidic chloride solution by non-toxic thiadiazol Derivative," *Journal of Adhesion Science and Technology*, vol.31, no.4, pp 369–387, (2016).

[9] A. Lalitha, S. Ramesh and S. Rajeswari, "Surface protection of copper in acid medium by azoles and Surfactants," *Electrochimica Acta*, vol.51, no.1, pp.47-55, (2005).

[10] Gürten, A. A., Kayakırılmaz, K., & Erbil, M, "The effect of thiosemicarbazide on corrosion resistance of steel reinforcement in concrete," *Construction and Building Materials,* vol. *21, no.3, pp. 669–676,* (2007).

[11] M. M. Singh, R. B. Rastogi, B. N. Upadhyay, and M. Yadav, "Thiosemicarbazide, phenyl isothiocyanate and their condensation product as corrosion inhibitors of copper in aqueous chloride solutions," *Materials Chemistry and Physics, vol. 80, no. 1. pp. 283–293, 2003.*

[12] Y. Santana Jiménez, M. Tejera Gil,M. Torrado Guerra, L.S. Baltes, J.C. Mirza Rosca, "Interpretation of open circuit potential of two titanium alloys for a long-time immersion in physiological fluid," *Bulletin of the Transylvania University of Brasov*, vol.2, no. 51, pp.97–204, (2009).

[13] T. Ramde, S. Rossi, and C. Zanella, "Inhibition of the Cu65/Zn35 brass corrosion by natural extract of Camellia sinensis," Appl. Surf. Sci., vol. 307, pp. 209–216, 2014.

[14] E.E. Oguzie, Y. Li, F.H. Wang, "Effect of 2-amino-3-mercaptopropanoic acid (cysteine) on the Corrosion behavior of low carbon steel in sulphuric acid," *Electrochimica Acta*, vol.53, no.2, pp. 909– 914, (2007).

[15] A. Fiala, W. Boukhedena, S. E. Lemallem, H. Brahim Ladouani, and H. Allal, "Inhibition of Carbon Steel Corrosion.in HCl and H2SO4 Solutions by Ethyl 2-Cyano-2-(1,3-dithian-2-ylidene) Acetate," *J. Bio- Tribo- Corrosion*, vol. 5, no. 2, pp. 20–22, 2019.

[16] C. B. P. Kumar, K. N. Mohana, and H. B. Muralidhara, "Electrochemical and thermodynamic studies to evaluate the inhibition effect of synthesized piperidine derivatives on the corrosion of mild steel in acidic medium," Ionics (Kiel)., vol. 21, no. 1, pp. 263–281, 2015

[17] S. Hong, W. Chen, H.Q. Luo, N.B. Li, "Inhibition effect of 4-amino-antipyrine on the corrosion of copper in 3wt.% NaCl solution," *Corrosion Science*, vol.57, pp. 270–278, (2012).

[18] D. Daoud, T. Douadi, H. Hamani, S. Chafaa, M. Al-Noaimi, "Corrosion inhibition of mild steel by two new S-heterocyclic compounds in 1 M HCl: experimental and computational study," *Corrosion Science,* vol.94, pp. 21–37, (2015).

[19] L. Guo, S. Zhu, S. Zhang, "Experimental and theoretical studies of benzalkonium chloride as an inhibitor for carbon steel corrosion in sulfuric acid," *Journal of Industrial Engineering Chemistry*, vol.24, pp. 174–180, (2015).

[20] R. Karthikaiselvi, S. Subhashini, "Study of adsorption properties and inhibition of mild steel corrosion in hydrochloric acid media by water soluble composite poly (vinyl alcohol-o-methoxy aniline)," J. *Assoc. Arab Univ. Basic Appl. Sci.*, vol.16, pp.74–82, (2014).

SYNTHESIS AND SPECTROSCOPIC CHARACTERIZATION OF BIDENTATE SCHIFF BASE AND ZINC(II) COMPLEX

Selma YILDIRIM UÇAN[1,*] iD

[1]Nigde Omer Halisdemir University, Chemistry Department, 51240, Nigde, Turkey

ABSTRACT

A new asymmetric bidentate Schiff base ligand was synthesized from 4-Methoxysalicylaldehyde. The complex was prepared by adding Zn(II) acetate salt dissolved in methanol to the Schiff base ligand. The ligand and its metal complex were characterized by FT-IR, UV-Vis spectroscopy, ^{1}H NMR, TG/DTG, SEM, magnetic susceptibility, conductometric measurements and elemental analysis (CHN), The spectroscopic data reveals that the Zn(II) atom in center of the complex is four-coordinated by two phenolic oxygen atoms and two azomethine nitrogen atoms of two Schiff base ligands. The Zn(II) complex is diamagnetic as expected for d^{10} metal ions in a tetrahedral geometry. The Zn(II) complex is soluble in dimethylformamide and dimethylsulfoxide and is insoluble in acetone, chloroform, ethanol and methanol. The conductance data indicate that the complex is non-electrolytes.

Keywords: Schiff base, Zinc(II) complexes, IR analysis, Thermogravimetric analysis

1. INTRODUCTION

This is the extended version of the paper titled "Synthesis of Complex of Schiff Base Containing 4-Methoxysalicylaldehyde". Azomethine group (C=N), well-known as Schiff bases are synthesized by the condensation reaction of primary amines with aldehyde or ketone [1]. The transition metal complexes of Salen ligands have contributed importantly to the development of coordination chemistry. Schiff base complexes are a substantial field of work for research pharmacy and medicine because of their perfect properties such as anticancer [2], antimicrobial [3] and antioxidant activity [4]. Zinc is an essential trace element in biological systems and has been found to play a substantial role in the survival and functioning of whole living organisms. Zinc has a considerable role in many biological activities and Zn(II) complexes are extensively researched because of their structural diversity and thermal stability [5]. Zinc complexes are well-known for implementations in luminescent materials, biosensors, and medicaments [6].

This work describes the preparation and structure of zinc(II) complex synthesized from 4-Methoxysalicylaldehyde and aniline. The synthesized Zn(II) complex was characterized, using several techniques. Among them were elemental analysis, molar conductivity, magnetic susceptibility, melting point, FT-IR, ^{1}H NMR, UV-Vis, SEM and thermal analysis.

2. MATERIAL AND METHOD

2.1. Materials and physical measurements

The chemicals and solvents were purchased from Sigma-Aldrich and Merck. All the chemicals and solvents were of analytical grade. The ligand and zinc(II) complex were synthesized by the condensation reaction method. Elemental analysis (C, N and H) was performed on a Carlo Erba 1106 type elemental analysis. Magnetic moment of metal complex was determined using a Sheerwood Scientific MX Gouy magnetic moment apparatus and magnetic measurement was carried out using the Gouy method with Hg[Co(SCN)$_4$] as calibrant. The IR spectra of the compounds were recorded by FT-IR (ATR sampling accessory) Perkin Elmer Spectrum BX-II spectrophotometer in the 4000-400 cm^{-1}. The ^{1}H NMR spectra in CDCl$_3$ or d$_6$-DMSO solution were recorded at room temperature with a Bruker 200 MHz spectrometer. UV-Visible spectra were recorded on a Shimadzu UV-160 spectrophotometer in the wavelength of 200-800 nm. Molar conductivity was carried out with a WTW LF model 330 conductivity meters, utilizing the prepared solution of the complex in DMF. Thermal gravimetric analysis was conducted on a TGA SHIMADZU model 50 thermal gravimetric analyzer. The SEM images of the complexes were analysed by using ZEISS EVO 40 attached with EDX Unit.

2.2. Synthesis of Schiff base ligand

The Schiff base ligand was prepared by modifying the method in the literature [7]. Aniline (0.931 g, 10 mmol) was dissolved in methanol (10 mL) and added to a solution of 4-methoxysalicylaldehyde (1.521 g, 10 mmol) in methanol (20 mL). The reaction was stirred for 3 h and leave overnight at 25 ºC. The orange color precipitate was filtered and washed with methanol. The ligand was recrystallized from dichloromethane, dried in a vacuum desiccator and the purity was controlled by TLC. Yield; 1,63 g, %72, m. p. 89 ºC. IR spectrum, ν, cm^{-1}: 3400 (OH), 3080 (C–H_{arom}), 1620 (C=N), 1155 (C–O). ^{1}H NMR spectrum (DMSO-d_6), δ, ppm: 12.44 s (1H, O–H), 8.92 s (1H, HC=N), 7.48-6.89 m (8H, C–H_{arom}), 3,74 s (3H, O-CH_3). Calculated for $C_{14}H_{13}NO_2$ (%): C 73.99; H 5.77; N 6.16. Found, %: C 73.88; H 5.62; N 6.09.

2.3. Synthesis of Zinc(II) Complex

The synthesis of the zinc(II) complex is given in scheme 1. The Zinc(II) complex was prepared by modifying the method available in the literature [8]. A solution of ligand (0.454 g, 2 mmol) in methanol (30 mL) was added to a solution of zinc(II) acetate (0,219 g, 1 mmol) in methanol (10 mL). The reaction mixture was stirred and refluxed for 5 h at 60 ºC. The yellow colour precipitate was filtered, washed several times with ether, ethanol and recrystallized of dichloromethane/methanol dried in vacuum. Yield; 0.36 g, 70%, m.p. 221 ºC. IR spectrum, ν, cm^{-1}: 1602 (C=N), 1143 (C–O), 487 (M–N), 475 (M–O). ^{1}H NMR spectrum (DMSO-d_6), δ, ppm: 8.77 s (2H, HC=N), 7.36-6.68 m (16H, C–H_{arom}), 3,70 s (6H, O–CH_3). Calculated for $C_{28}H_{24}N_2O_4Zn$ (%): C 64.94; H 4.67; N 5.41. Found, %: C 64.78; H 4.51; N 5.25.
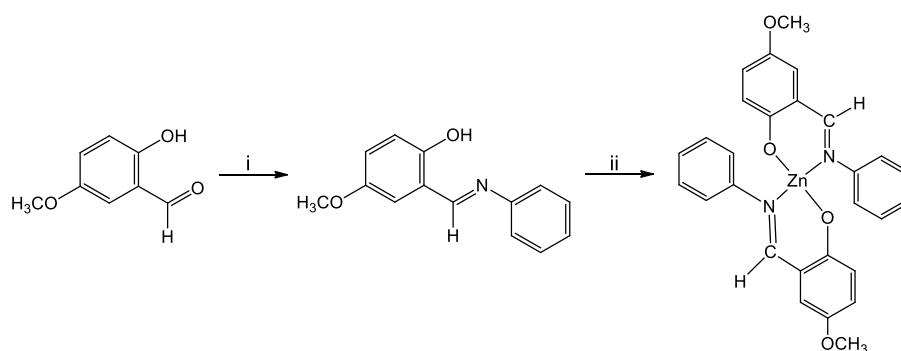
Scheme 1. Synthesis of of Zn(II) complex (i: $C_6H_5NH_2$, CH_3OH; ii: $Zn(CH_3COO)_2.2H_2O$, CH_3OH, 60 ºC).

3. RESULTS AND DISCUSSION

The solubility of these two new compounds was checked in various solvents. The Schiff base is soluble in ethanol, methanol, dichloromethane and diethyl ether. The Zn(II) complex is soluble in dimethylformamide and dimethylsulfoxide, but insoluble in ethanol, chloroform and acetone. The elemental analyses data of the Schiff base ligand and Zn(II) complex are consistent with those calculated from the empirical formulas for each compound. The Zn(II) complex was obtained as yellow crystalline solid in high yield of about 70% and high purity.

3.1. IR Spectra

The IR spectrum of the ligand indicated a band at 1620 cm^{-1}. This peak was assigned to the stretching frequency of the azomethine (CH=N) group. This peak is shifted to lower frequencies in the complex, indicating that the nitrogen atom of the azomethine group is coordinated to the metal ion [5]. The OH peak of the ligand was seen as a broad band at 3400 cm^{-1}. This peak, which is not seen in the complex, indicates that the metal ion is coordinated over oxygen. The IR spectrum of the metal complex indicated new peaks in the 487 and 475 cm^{-1} regions because of the constitution of the M-O and M-N peaks, respectively [9]. The IR spectra of the Shiff base ligand and the Zn(II) complex are showed in Figure 1.

SYNTHESIS AND SPECTROSCOPIC CHARACTERIZATION OF BIDENTATE SCHIFF BASE AND ZINC(II) COMPLEX
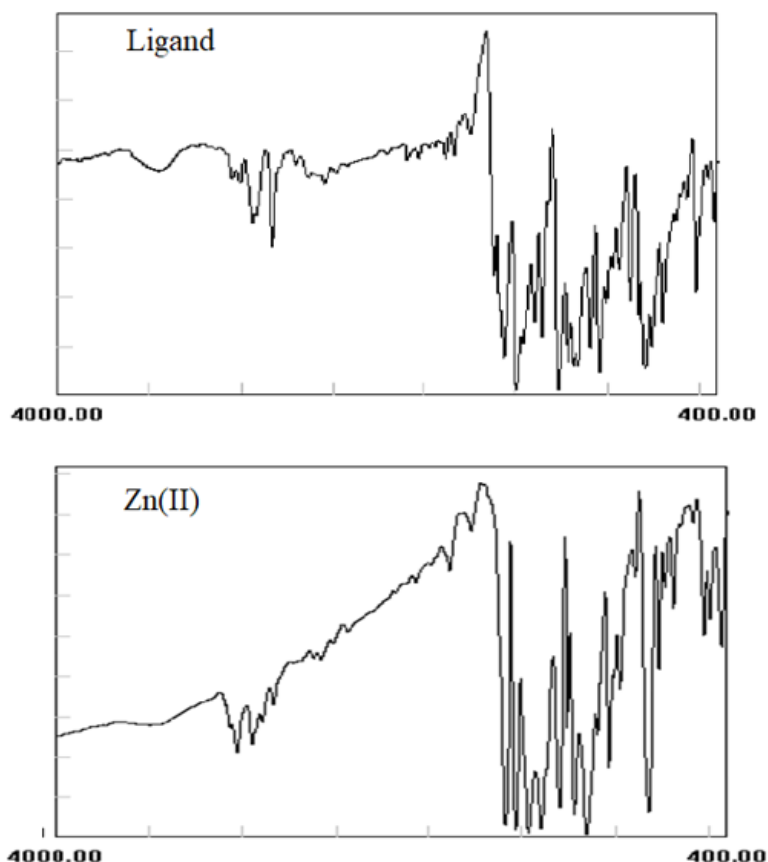

Figure 1. IR spectra of ligand and Zn(II) complex

3.2. UV Spectra and magnetic susceptibility

The electronic spectra of the ligand and zinc(II) complex were recorded for their solutions of concentration 10^{-3} M done in DMF solution in the wavelength range from 200 to 800 nm. The spectra displayed a sharp band at 277 nm which is attributed to $\pi-\pi^*$ transition within the benzene ring of the Schiff base ligand. Also, the two bands observed at 340 and 368 nm in the free ligand are reasonably accounted for $\pi-\pi^*$ and $n-\pi^*$ transitions for the phenolic-OH and azomethine moieties [10]. The magnetic moment value observed for zinc(II) was found to be zero at room temperature. The Zn(II) complex is diamagnetic as it is d^{10} system [8].

3.3. ^{1}H NMR Spectra

The ^{1}H NMR spectra of the Shiff base ligand and Zn(II) complex were carried out in DMSO-d_6. The ^{1}H NMR spectra of the Shiff base ligand and the complex are demonstrated in Figure 2. A peak of the phenolic-OH group is observed as a singlet at 12.44 ppm [11]. The azomethine proton (CH=N) in the Shiff base ligand appears as a singlet at 8.92 ppm, while the azomethine proton of the complex appears as a singlet at 8.77 ppm. The aromatic ring protons are observed in the 7.48-6.89 ppm range as expected. In the spectrum of the Shiff base ligand, the singlet at 3.74 ppm can be attributed to the -OCH$_3$ protons [12].
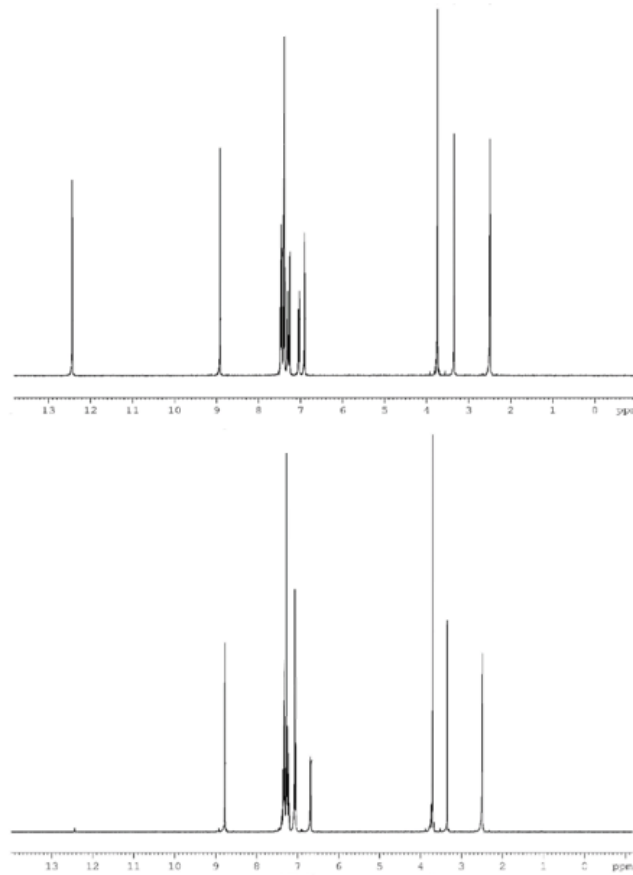
Figure 2. ^{1}H NMR spectrum of Schiff Base ligand and Zn(II) complex.

3.4. Thermal analysis

The weight losses for the complex was calculated within the corresponding temperature ranges (Figure 3). Thermal behavior of the complex was studied utilizing thermogravimetric analysis from 50 °C to 1000 °C in a nitrogen atmosphere. Zinc(II) complex decomposed in two steps. The first step was observed in the range 50-550 °C with a weight loss of 55.40 %, which was assigned to partial elimination of a $C_{20}H_{17}NO$ fragment. The second step corresponded to removal of $C_8H_7NO_2$ molecule with a weight loss of 29.10 %. The final weight of the residue corresponds to zinc oxide [13].

Figure 3. TG/DTA curves of Zinc(II) complex

SYNTHESIS AND SPECTROSCOPIC CHARACTERIZATION OF BIDENTATE SCHIFF BASE AND ZINC(II) COMPLEX

3.5. Conductance measurement

The complex was dissolved in DMF and the molar conductivity of 10^{-3} M of its solution at 25 °C was measured. It is concluded from the result that the complex is found to have molar conductance value of 1.4 $\Omega^{-1}cm^2\,mol^{-1}$ indicating that this complex is non-electrolytes [14].

3.6. SEM analysis

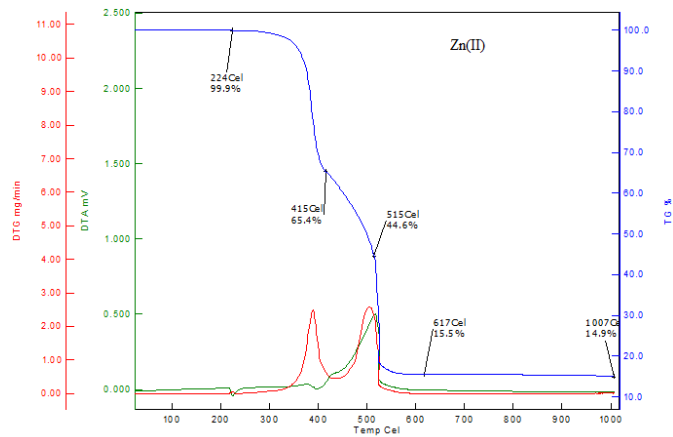SEM technique has been utilized to determine the morphology of ligand and zinc(II) complex. The SEM images of compounds have displayed distinct images as in Figure 4. The Ligand shows the ice mass structure was existing. The SEM image of the Zn(II) complex has looked like as crushed ice pieces shape. Ligand and Zn(II) complex have different typical surface images [15].
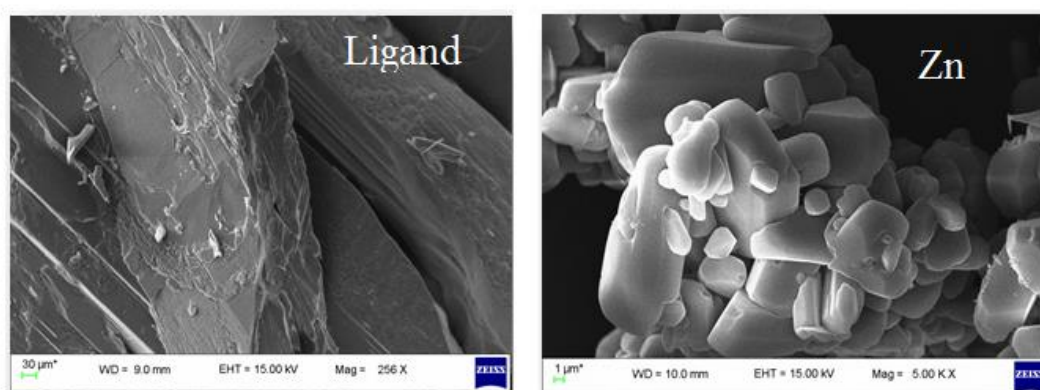
Figure 4. SEM morphologies of Schiff Base ligand and Zinc(II) complex.

4. CONCLUSION

Thus, the following conclusions can be made. The new transition metal complex derived from a bidentate Schiff base was synthesized. Schiff base ligand and Zn(II) complex were characterized by spectral and analytical data. The analytical data show the compound of the zinc(II) complex to be [ML$_2$], where L is the Schiff base ligand. The ^{1}H NMR and IR spectrum demonstrated that the ligand coordinated with metal ion through two phenolic oxygen atoms and two azomethine nitrogen atoms. The electronic spectral data show that Zinc(II) complex has tetrahedral geometry. The Thermal stability of the complex was investigated and evaluated individually by utilizing TG/DTA.

ACKNOWLEDGEMENT

REFERENCES

[1] H. Schiff, "Untersuchungen über salicinderivate," *Annalen der Chem.* Vol. 150, no. 2, Feb., pp. 193-200, 1869.

[2] J. Y. Al-Humaidi, "In situ alkaline media: Synthesis, spectroscopic, morphology and anticancer assignments of some transition metal ion complexes of 1-((2-aminophenylimino) methyl) naphthalen-2-ol Schiff base," *Journal of Molecular Structure*, vol. 1183, May., pp. 190-201, 2019.

[3]   R. Reddy, Trivedi, B. S. Kumar, K. Sirisha, A.V. Sarma, B. Sridhar, and R. S. Prakasham, "Synthesis, characterization and antimicrobial activity of novel Schiff base tethered boronate esters of 1,2-*O*-isopropylidene-α-D-xylofuranose," *Bioorg. Med. Chem. Lett*. Vol. 26, no.15, Aug., pp. 3447-3452, 2016.

[4]   I. Gönül, M. Köse, G. Ceyhan, and S. Serin, "Methoxy group containing bidentate Schiff base ligands and their transition metal complexes: Synthesis, structural characterization, photoluminescence, antioxidant capacity and superoxide dismutase activity studies," *Inorganica Chimica Acta*, vol. 453, Nov., pp. 522-530, 2016.

[5]   M. Mokhles, "Spectroscopic Characterization of Some Tetradentate Schiff Bases and Their Complexes with Nickel, Copper and Zinc," *Journal of the Chinese Chemical Society,* vol. 48, no. 2, Apr., pp. 153-158, 2001.

[6]   M. Kumar, S. Roy, M. S. H. Faizi, S. Kumar, M. K. Singh, S. Kishor, S. C. Peter, and R. P. John, "Synthesis, crystal structure and luminescence properties of acenaphthene benzohydrazide based ligand and its zinc (II) complex." *Journal of Molecular Structure*, vol. 1128, Jan., pp. 195-204, 2017.

[7]   S. Ucan, A. Öztürk, N. Sarıkavaklı, and T. Hökelek, "4-Methoxy-2-[(E)-(phenylimino) methyl] phenol. *Acta Crystallographica Section E: Structure Reports Online*, vol. 64, no. 9, Sep., pp. o1818-o1819, 2008.

[8]   S. Y. Ucan, "Synthesis, spectral, thermal, and magnetic studies of cobalt (II), nickel (II), copper (II), zinc (II), and cadmium (II) complexes with N_2O_2 donor groups," *Russian Journal of General Chemistry*, vol. 84, no. 9, Oct., pp. 1819-1824, 2014.

[9]   A. Kakanejadifard, F. Esna-ashari, P. Hashemi, and A. Zabardasti, "Synthesis and characterization of an azo dibenzoic acid Schiff base and its Ni (II), Pb (II), Zn (II) and Cd (II) complexes," *Spectrochimica Acta Part A: Molecular and Biomolecular Spectroscopy,* vol. 106, Apr., pp. 80-85, 2013.

[10] M. Khorshidifard, H. Amirirudbari, B. Banafshe Askari, M. Mehdisahihi, M. Riahifarsani, F. Faribajalilian, and G. Giuseppebruno, "Cobalt(II), Copper(II), Zinc(II) and Palladium(II) Schiff Base Complexes: Synthesis, Characterization and Catalytic Performance in Selective Oxidation of Sulfides Using Hydrogen Peroxide under Solvent-Free Conditions," *Polyhedron*, vol. 95, Apr., pp. 1-13, 2015.

[11] M. Mohammadikish, "Green synthesis and growth mechanism of new nanomaterial: Zn(salen) nano-complex," *Journal of Crystal Growth*, vol. 431, Dec., pp. 39-48, 2015.

[12] J. C. Pessoa, and I. Correia, "Salan vs. salen metal complexes in catalysis and medicinal applications: Virtues and pitfalls," *Coordination Chemistry Reviews,* vol. 388, Jun., pp. 227-247, 2019.

[13] B. Hamide, Gr. Gholamhossein, E. Vaclav, D. Michal, and D. K. Aliakbar, "Copper (II), nickel (II), zinc (II) and vanadium (IV) Schiff base complexes: Synthesis, characterization, crystal structure determination, and thermal studies," *Polyhedron*, vol. 146, May., pp. 19-25, 2018.

[14] T. N. Rahmouni, N. H. Bensiradj, S. A. Megatli, S. Djebbar, and O. B. Baitich, "New mixed amino acids complexes of iron (III) and zinc (II) with isonitrosoacetophenone: Synthesis, spectral characterization, DFT study and anticancer activity," *Spectrochimica Acta Part A: Molecular and Biomolecular Spectroscopy*, vol. 213, Apr., pp. 235-248, 2019.

[15] B. Mohan, A. Jana, N. Das, S. Bharti, and M. Choudhary, "Syntheses, crystal structures, antioxidant SOD-like properties and in-vitro antimicrobial studies of Cu (II) and Ni (II) complexes with 2-((E)-(4-bromo-2-chloro-phenylimino) methyl)-6-bromo-4-nitrophenol and (E)-1-(3,5-dichloro-2-hydroxybenzylidene)-4, 4-dimethylthiosemi-carbazide, "*Journal of Molecular Structure*, vol. 1171, Nov., pp. 94-109, 2018.

ON THE STABILITY OF A PARTIALLY IONIZED PLASMA

Pardeep KUMAR[1,*] , Hari MOHAN[2]

[1,2]*Department of Mathematics, ICDEOL, Himachal Pradesh University, Summerhill, Shimla-171005, INDIA.*

ABSTRACT

The Rayleigh-Taylor instability of an infinitely conducting plasma of variable density in the presence of a horizontal magnetic field is considered when the effects of finite ion Larmor radius (FLR) and collisions with neutral atoms simultaneously present. Here we considered the perturbations propagating along the ambient magnetic field. It is observed that, real part of n is negative, where n is the growth rate of disturbance, so that instability does not arise in the form of increasing amplitude, i.e. overstability. To obtain an approximate solution of the problem, a variational principle is used. The case of two semi-infinitely extending plasmas of constant densities separated by a horizontal interface is also considered, where it is found that the system is stable (for some wave numbers) for potentially stable configuration and unstable (for other wave numbers) for potentially unstable configuration even if there are collisions with dust particles. Also it is observed that the criteria determining stability and instability are independent of FLR effects.

Keywords: Rayleigh-Taylor instability, Conducting plasma, Horizontal magnetic field

1. INTRODUCTION

The instability of the plane interface separating two fluids when one is accelerated towards the other or when one is superposed over the other has been studied by several authors and Chandrasekhar [1] has given a detailed account of these investigations together with the possible extensions in various domains of interest. The stabilizing influence of finite Larmor radius effects has individually been shown on thermal instability, thermosolutal instability, gravitational instability and Rayleigh-Taylor instability, by several authors [2-6].

Quite often the plasma is not fully ionized and is, instead, partially ionized. Partially ionized plasma represents a state which often exists in the Universe and there are several situations when the interaction between the ionized and neutral gas components becomes important in cosmic physics. The study of partially ionized plasmas has become a hot topic because solar structures such as spicules, prominences, as well as layers of the solar atmosphere (photosphere and chromosphere), are made of partially ionized plasmas. On the other hand, considerable developments have taken place in the study of partially ionized plasmas applied to the physics of the interstellar medium, molecular clouds, the formation of protostellar discs, planetary magnetospheres/ionospheres, exoplanets atmospheres, etc. For instance, molecular clouds are mainly made up of neutral material which does not interact with magnetic fields. However, neutrals are not the only constituent of molecular clouds since there are also several types of charged species which do interact with magnetic fields. Furthermore, the charged fraction also interacts with the neutral material through collisions. These multiple interactions produce many different physical effects which may have a strong influence on star formation and molecular cloud turbulence. A further example can be found in the formation of dense cores in molecular clouds induced by MHD waves. Because of the low ionization fraction, neutrals and charged particles are weakly coupled and ambipolar diffusion plays an important role in the formation process. Even in the primeval universe, during the recombination era, when the plasma, from which all the matter of the universe was formed, evolved from fully ionized to neutral, it went through a phase of partial ionization. Partially ionized plasmas introduce physical effects which are not considered in fully ionized plasmas, for instance, Cowling's resistivity, isotropic thermal conduction by neutrals, heating due to ion/neutral friction, heat transfer due to collisions, charge exchange, ionization energy, etc., which are crucial to fully understand the behaviour of astrophysical plasmas in different environments. Stromgren [7] has reported that ionized hydrogen is limited to certain rather sharply bounded regions in space surrounding, for example, O-type stars and clusters of such stars and that the gas outside these regions is essentially non-ionized. Other examples of the existence of such situations are given by Alfven's [8] theory on the origin of the planetary system, in which a high ionization rate is suggested to appear from collisions between a plasma and a neutral-gas cloud and by the absorption of plasma waves due to ion-neutral collisions such as in the solar photosphere and chromosphere and in cool interstellar clouds [9, 10]. Lehnert [11] has found that both ion viscosity and neutral gas friction have a stabilizing influence on cosmical plasma interacting with a neutral gas. According to Hans [12] and Bhatia [13], the medium may be idealized as a composite mixture of a hydromagnetic (ionized) component and a neutral component,

P. Kumar, H. Mohan

the two interacting through mutual collisional (frictional) effects. A stabilizing effect of collisionals on Rayleigh-Taylor configuration has been shown by [12] and [13]. But the collisional effects are found to be destabilizing for a sufficiently large collisional frequency on Kelvin-Helmholtz configuration by Rao and Kalra [14] and [12]. Chhajlani et. al [15] considered the hydromagnetic Rayleigh-Taylor instability of a composite medium in the presence of suspended particles for an exponentially varying density distribution. The Rayleigh-Taylor instability of a partially ionized plasma in a porous medium in the presence of magnetic field perpendicular to gravity has been considered by Sharma and Sunil [16]. The gravitational instability of a rotating Walters B' viscoelastic partially ionized plasma permeated by an oblique magnetic field in the presence of the effects of Hall currents, electrical resistivity and ion viscosity has been considered by El-Sayed and Mohamed [17]. Hoshoudy [18] has investigated the Rayleigh-Taylor instability in stratified plasma in the presence of combined effect of horizontal and vertical magnetic field. Sharma et. al [19] have investigated the effect of surface tension on hydromagnetic Rayleigh-Taylor instability of two incompressible superimposed fluids in a medium with suspended dust particles in a uniform horizontal magnetic field.

In the present work, we study the simultaneous effects of ion Larmor radius and collisions with neutral atoms on the stability of well-known Rayleigh-Taylor configuration in hydromagnetics. We regard the medium as being a mixture of an infinitely conducting component a neutral component interacting through mutual collisions. We make the assumptions that the individual components by themselves, behave like continuum plasmas and that the effects on the neutral component resulting from magnetic field, pressure and gravity are negligible. The case of a uniform horizontal field and longitudinal perturbations is considered. Next a variational principle is developed to obtain the approximate solutions.

2. FORMULATION OF THE PROBLEM

Here we consider two inviscid, homogeneous, semi-infinitely extending plasmas separated by a plane interface at $z = 0$, each region being permeated with a neutral component of the same density. Initially the configuration is at rest. We give a small disturbance to the system. The linearized perturbation equations for the mixture of the hydromagnetic plasma and a neutral gas moving together in a uniform horizontal magnetic field $\vec{H}(H, 0,0)$ and downward gravitational field $\vec{g}(0, 0, -g)$ are

$$\rho \frac{\partial \vec{q}}{\partial t} = -\nabla \delta \vec{P} + \frac{1}{4\pi}(\nabla \times \vec{h}) \times \vec{H} + \vec{g}(\delta \rho) + \rho_d \nu_c(\vec{q_d} - \vec{q}), \tag{1}$$

$$\frac{\partial \vec{q_d}}{\partial t} = -\nu_c(\vec{q_d} - \vec{q}), \tag{2}$$

$$\frac{\partial}{\partial t}(\delta \rho) = (\vec{q}.\nabla)\rho, \tag{3}$$

$$\frac{\partial \vec{h}}{\partial t} = (\vec{H}.\nabla)\vec{q}, \tag{4}$$

$$\nabla.\vec{q} = 0 \quad \text{and} \quad \nabla.\vec{h} = 0, \tag{5}$$

where ρ and ρ_d are the unperturbed densities for the hydromagnetics and the neutral component, respectively. ν_c denotes the collisional frequency between the two components and $\delta \vec{P}$ denotes the plasma pressure rendered tensorial due to finite ion Larmor radius effect. Here $\delta \rho, \delta \vec{P}, \vec{q}(u, v, w), \vec{q_d}(l, r, s), \vec{h}(h_x, h_y, h_z)$ denote, respectively, the perturbations in density ρ, stress tensor $\vec{P}$, hydromagnetic plasma velocity (initially zero), neutral component velocity (initially zero) and magnetic field $\vec{H}$. Magnetic permeability of the medium is assumed to be unity.

For the magnetic field along x-axis, $\delta \vec{P}$ taking into account the FLR effects has the following components

ON THE STABILITY OF A PARTIALLY IONIZED PLASMA

$$P_{xx} = p, \quad P_{xy} = P_{yx} = -2\rho v \left(\frac{\partial w}{\partial x} + \frac{\partial u}{\partial z} \right),$$

$$P_{xz} = P_{zx} = 2\rho v \left(\frac{\partial u}{\partial y} + \frac{\partial v}{\partial x} \right),$$

$$P_{yz} = P_{zy} = \rho v \left(\frac{\partial v}{\partial y} - \frac{\partial w}{\partial z} \right), \qquad (6)$$

$$P_{yy} = p - \rho v \left(\frac{\partial v}{\partial z} + \frac{\partial w}{\partial y} \right),$$

$$P_{zz} = p + \rho v \left(\frac{\partial v}{\partial z} + \frac{\partial w}{\partial y} \right),$$

where p is the scalar part of the pressure and $\rho v = \frac{NT}{4\omega_H}$; ω_H is the ion-gyration frequency, while N and T denote, respectively, the number density and temperature of ions and K^* is the Boltzmann constant.

Analyzing the disturbances in terms of longitudinal modes, we seek the solutions of equations (1) - (5) in which $x - t$ dependence is given by

$$exp(ikz + nt), \qquad (7)$$

where k denotes the wave number of disturbance and n is the growth rate of disturbance.

Eliminating q_d between equations (1) and (2), and using (6) and (7), equations (1)-(5) can be written as

$$\left[n\rho + \frac{\rho_d v_c}{n + v_c} \right] u = -ik\delta p - 2ikvD(\rho v), \qquad (8)$$

$$\left[n\rho + \frac{\rho_d v_c}{n + v_c} \right] v = -2\rho v(D^2 + k^2)w + vD(\rho Dw) + \frac{ikHh_y}{4\pi}, \qquad (9)$$

$$\left[n\rho + \frac{\rho_d v_c}{n + v_c} \right] w = -D(\delta p) + 2\rho v k^2 v - vD(\rho Dv) + \frac{gw}{n}(DP) + \frac{H}{4\pi}(ikh_z - Dh_x), \qquad (10)$$

$$n\delta\rho = -w(D\rho), \qquad (11)$$

$$n\vec{h} = ikH\vec{q}, \qquad (12)$$

$$iku + Dw = 0, \qquad (13)$$

and

$$ikh_z + Dh_x = 0, \qquad (14)$$

Where

$$D = \frac{d}{dz}.$$

If we eliminate δp from equations (8) and (10), and use equations (11)-(14), we obtain the following pair of equations in w and v

$$n^2 \left(\rho k^2 w - D(\rho Dw) \right) - gk^2(D\rho)w - \frac{H^2 k^2}{4\pi}(D^2 - k^2)w - vnk^2[2(D^2 + k^2)(\rho v) - D(\rho Dv)]$$

$$+ \frac{v_c}{n + v_c} n^2[\rho_d k^2 w - D(\rho_d Dw)] = 0, \qquad (15)$$

and

P. Kumar, H. Mohan

$$\left[n\rho + \frac{\rho_d v_c}{n + v_c} n + \frac{H^2 k^2}{4\pi n} \right] v = -v[2\rho(D^2 + k^2)w - D(\rho Dw)]. \tag{16}$$

Boundary conditions

On a boundary, vertical motion is not possible, thus

$$w = 0 \tag{17}$$

on a boundary free or rigid.

  If the plasma is bounded by two rigid boundaries which are both ideally conducting, no disturbance within it can change the electromagnetic quantities outside. This merely leads to the boundary condition (17). A boundary condition on v can be prescribed by preluding the presence of surface charge or surface current at the rigid boundaries which are perfectly conducting. Thus we choose

$$v = 0, \tag{18}$$

at a surface bounded by an ideal conduction.

  If the plasma is confined between two free boundaries, the tangential stresses

$$P_{xx} = 2\rho v i k v + \frac{i k H^2 w}{4\pi n}$$

and $P_{yz} = -\rho v Dw$ vanish. Hence

$$v = Dw = 0, \tag{19}$$

at a free boundary. Should there be discontinuities in the density as in the case of two superposed layers of different densities, we require the continuity of the vertical component of velocity, tangential stresses and pressure at interface. Thus

$$w, \ \rho Dw, \ \rho v, \ \rho_d Dw, \ \rho_d v \tag{20}$$

and the total pressure must be continuous as at the interface.

3. DISCUSSION

  Theorem I: A necessary and sufficient condition for δn^2 to be zero to the first order for all small arbitrary variations δw and δv (connected by equation (38)) in w and v which is compatible with the boundary conditions is that w and v should be the solutions of the eigenvalue problem governed by equations (15) and (16).

  Proof: Let n_i and n_j denote the two characteristic values, and let the solutions belonging to these characteristics values be distinguished by the subscripts i and j. Multiplying equation (15) for i by w_j and integrating with respect to z over the whole vertical extent of the plasma (denoted by $\int_L$), we obtain with the help of equation (16) and boundary conditions,

$$n_i^2 \int_L \rho \left(w_i w_j + \frac{1}{k^2} Dw_i Dw_j \right) dz + \frac{v_c}{n_i + v_c} n_i^2 \int_L \rho_d \left(w_i w_j + \frac{1}{k^2} Dw_i Dw_j \right) - g \int_L (D\rho) w_i w_j dz$$

$$+ \frac{H^2 k^2}{4\pi} \int_L \left(w_i w_j + \frac{1}{k^2} Dw_i Dw_j \right) dz + n_i n_j \int_L \rho v_i v dz + \frac{v_c n_i n_j}{n_j + v_c} \int_L \rho_d v_i v_j dz + \frac{H^2 k^2 n_i}{4\pi n_j} \int_L v_i v_j dz$$

$$= 0. \tag{21}$$

  Taking $i = j$ and suppressing the subscripts, we obtain the following variational formulation of the problem

$$n^2[I_1 + I_4 + I_6 + I_7] - gI_2 + I_3 + I_5 = 0, \tag{22}$$

where

ON THE STABILITY OF A PARTIALLY IONIZED PLASMA

$$I_1 = \int_L \rho \left[w^2 + \frac{1}{k^2} (Dw)^2 \right] dz, \tag{23}$$

$$I_2 = \int_L (D\rho) w^2 dz, \tag{24}$$

$$I_3 = \frac{H^2 k^2}{4\pi} \int_L \left[w^2 + \frac{1}{k^2} (Dw)^2 \right] dz, \tag{25}$$

$$I_4 = \int_L \rho v^2 dz, \tag{26}$$

$$I_5 = \frac{H^2 k^2}{4\pi} \int_L v^2 dz, \tag{27}$$

$$I_6 = \frac{\nu_c}{n + \nu_c} \int_L \rho_d \left[w^2 + \frac{1}{k^2} (Dw)^2 \right] dz, \tag{28}$$

$$I_7 = \frac{\nu_c}{n + \nu_c} \int_L \rho_d v^2 dz. \tag{29}$$

Consider a change δn^2 on n^2 of an arbitrary variation δw and δv in w and , respectively to satisfy the boundary conditions (17) and (18) of the eigen-value problem, we have to the first order, from 22

$$\delta n^2 (I_1 + I_4 + I_6 + I_7) + n^2 (\delta I_1 + \delta I_4 + \delta I_6 + \delta I_7) - g\delta I_2 + \delta I_3 + \delta I_5 = 0, \tag{30}$$

where $\delta I_s (s = 1 \, to \, 7)$ are the corresponding variations in $I_s (s = 1 \, to \, 7)$. After one or more integrations by parts, we find that these latter variations are given by

$$\frac{1}{2} \delta I_1 = \int_L \left[\rho w - \frac{1}{k^2} D(\rho Dw) \right] \delta w \, dz, \tag{31}$$

$$\frac{1}{2} \delta I_2 = \int_L (D\rho) w \delta w \, dz, \tag{32}$$

$$\frac{1}{2} \delta I_3 = \frac{H^2 k^2}{4\pi} \int_L \left(w - \frac{1}{k^2} D^2 w \right) \delta w \, dz, \tag{33}$$

$$\frac{1}{2} \delta I_4 = \int_L \rho v \delta v \, dz, \tag{34}$$

$$\frac{1}{2} \delta I_5 = \frac{H^2 k^2}{4\pi} \int_L v \delta v \, dz, \tag{35}$$

$$\frac{1}{2} \delta I_6 = \frac{\nu_c}{n + \nu_c} \int_L \left[\rho_d w - \frac{1}{k^2} D(\rho_d Dw) \right] \delta w \, dz \tag{36}$$

and

$$\frac{1}{2} \delta I_7 = \frac{\nu_c}{n + \nu_c} \int_L \rho_d \delta v \, dz. \tag{37}$$

Furthermore, δw and δv are connected by the relation

$$\delta n \left[\rho - \frac{H^2 k^2}{4\pi n^2} + \frac{\rho_d \nu_c^2}{(n + \nu_c)^2} \right] v + n \left[\rho + \frac{H^2 k^2}{4\pi n^2} + \frac{\rho_d \nu_c}{n + \nu_c} \right] \delta v = -\nu [2\rho(D^2 + k^2) \delta w - D(\rho Dw)]. \tag{38}$$

P. Kumar, H. Mohan

If we substitute for I_s and $\delta I_s (s = 1\ to\ 7)$ in equation (30) and make use of equation (38), we obtain after some further integrations by parts,

$$\delta n^2 \left[I_1 + \frac{1}{n^2} I_5 + I_6 \right]$$
$$+ \frac{2}{k^2} \int_L \left[n^2\{\rho k^2 w - D(\rho Dw)\} - gk^2(D\rho)w + \frac{v_c}{n+v_c} n^2\{\rho_d k^2 w - D(\rho_d Dw)\} - \frac{H^2 k^2}{4\pi}(D^2 - k^2)w \right.$$
$$\left. - vk^2 n\{2(D^2 + k^2)(\rho v) - D(\rho Dv)\} \right] \delta w\, dz$$
$$= 0. \tag{39}$$

We observe that the quantity occurring as a factor of δw under the integral sign vanishes if and only if equation (15) is satisfied. Thus a necessary and sufficient condition for δn^2 to be zero to the first order for all small arbitrary variations δw and δv (connected by equation (38)) in w and v which is compatible with the boundary conditions is that w and v should be the solutions of the eigenvalue problem governed by equations (15) and (16). A variational procedure of solving for the characteristic values is, therefore, possible.

Theorem II: If oscillatory modes exist they should be stable.

Proof: From equation (21), we have

$$n_i \int_L \left(w_i w_j + \frac{1}{k^2} Dw_i Dw_j \right) dz - \frac{g}{n_i} \int_L (D\rho) w_i w_j\, dz + \frac{H^2 k^2}{4\pi n_i} \int_L \left(w_i w_j + \frac{1}{k^2} Dw_i Dw_j \right) dz + n_j \int_L \rho v_i v_j\, dz$$
$$+ \frac{H^2 k^2}{4\pi n_j} \int_L v_i v_j\, dz + \frac{v_c n_i}{n_i + v_c} \int_L \rho_d \left(w_i w_j + \frac{1}{k^2} Dw_i Dw_j \right) dz + \frac{v_c n_i}{n_j + v_c} \int_L \rho_d v_i v_j\, dz = 0. \tag{40}$$

Interchanging i and j and noting that the above integrals are symmetric in i and j, we obtain

$$n_j \int_L \rho \left(w_i w_j + \frac{1}{k^2} Dw_i Dw_j \right) dz - \frac{g}{n_j} \int_L (D\rho) w_i w_j\, dz + \frac{H^2 k^2}{4\pi n_j} \int_L \left(w_i w_j + \frac{1}{k^2} Dw_i w_j \right) dz + n_i \int_L \rho v_i v_j\, dz$$
$$+ \frac{H^2 k^2}{4\pi n_i} \int_L v_i v_j\, dz + \frac{v_c n_j}{n_j + v_c} \int_L \rho_d \left(w_i w_j + \frac{1}{k^2} Dw_i Dw_j \right) dz + \frac{v_c n_i}{n_i + v_c} \int_L \rho_d v_i v_j\, dz = 0. \tag{41}$$

Let us consider two solutions characterized by n and n^*, the complex conjugate of n. We expect that the corresponding solutions will also be the complex conjugates of each other. Hence if $n_i = n, n_i = n^*$, then $w_i = w, w_j = w^*, v_i = v\ and\ v_j = v^*$.
Then, from (40) and (41) by addition and subtraction, we have

$$Re(n) \left[\bar{I}_1 + \bar{I}_5 - \frac{g}{|n|^2} \bar{I}_2 + \frac{H^2 k^2}{4\pi|n|^2} \bar{I}_3 + \frac{H^2 k^2}{4\pi|n|^2} \bar{I}_4 + \frac{v_c^2(\bar{I}_6 + \bar{I}_7)}{|n|^2 + 2v_c R_e(n) + v_c^2} \right] = \frac{-v_c|n|^2(\bar{I}_6 + \bar{I}_7)}{|n|^2 + 2v_c R_e(n) + v_c^2}, \tag{42}$$

and

$$Im(n) \left[\bar{I}_1 - \bar{I}_5 + \frac{g}{|n|^2} \bar{I}_2 - \frac{H^2 k^2}{4\pi|n|^2} (\bar{I}_3 - \bar{I}_4) + \frac{v_c^2(\bar{I}_6 - \bar{I}_7)}{|n|^2 + 2v_c R_e(n) + v_c^2} \right] = 0, \tag{43}$$

where

$$\bar{I}_1 = \int_L \rho \left[|w|^2 + \frac{1}{k^2} |Dw|^2 \right] dz, \quad \bar{I}_2 = \int_L (D\rho)|w|^2 dz, \quad \bar{I}_3 = \int_L \left[|w|^2 + \frac{1}{k^2} |Dw|^2 \right] dz,$$
$$\bar{I}_4 = \int_L |v|^2 dz, \quad \bar{I}_5 = \int_L \rho|v|^2 dz, \quad \bar{I}_6 = \int_L \rho_d \left[|w|^2 + \frac{1}{k^2} |Dw|^2 \right] dz, \tag{44}$$
$$\bar{I}_7 = \int_L \rho|v|^2 dz.$$

Integrals $\bar{I}_s (s = 1\ to\ 7)$ are all positive.

ON THE STABILITY OF A PARTIALLY IONIZED PLASMA

If n is complex, $Im(n) \neq 0$, hence (43) gives

$$\bar{I}_1 - \bar{I}_5 + \frac{g}{|n|^2}\bar{I}_2 - \frac{H^2k^2}{4\pi|n|^2}(\bar{I}_3 - \bar{I}_4) + \frac{v_c^2(\bar{I}_6 - \bar{I}_7)}{|n|^2 + 2v_c R_e(n) + v_c^2} = 0, \tag{45}$$

so that (42) gives

$$2Re(n)\left[\bar{I}_1 + \frac{H^2k^2}{4\pi|n|^2}\bar{I}_4 + \frac{v_c^2\bar{I}_6}{|n|^2 + 2v_c R_e(n) + v_c^2}\right] = -\frac{v_c|n|^2(\bar{I}_6 + \bar{I}_7)}{|n|^2 + 2v_c R_e(n) + v_c^2}. \tag{46}$$

From equation (46) it follows that $R_e(n)$ is negative, which implies that if oscillatory modes exist they should be stable, thus ruling out possibility of overstability.

4. DISCUSSION ON THE CASE OF TWO SEMI-INFINITELY EXTENDING PLASMAS OF CONSTANT DENSITIESSEPARATED BY A HORIZONTAL PLANE

We consider the case when two semi-infinitely extending plasma layers of constant densities ρ_1 and ρ_2, and dust particle densities ρ_{d_1} and ρ_{d_2} are separated by a horizontal boundary at $z = 0$. The subscripts 1 and 2 distinguish the lower and upper plasma layers, respectively.

We choose the following trial function for $w(z)$,

$$w(z) = \begin{cases} Ae^{+kz} & z < 0; \\ Ae^{-kz} & z > 0, \end{cases} \tag{47}$$

which is consistent with the boundary conditions (17) - (19). Here the same constant has been chosen to ensure the continuity of w at $z = 0$.

The value of v in the two regions can be calculated from equation (16) and noting that ρ is constant, we have

$$v(z) = \begin{cases} Z_1 e^{+kz} & z < 0; \\ Z_2 e^{-kz} & z > 0, \end{cases} \tag{48}$$

where

$$Z_{1,2} = \frac{-3vk^2nA}{n^2\left[1 + \frac{\alpha_0 v_c}{n+v_c}\right] + k^2 V_{1,2}^2}, \tag{49}$$

$$V_1^2 = \frac{H^2}{4\pi\rho_1} \ and \ V_2^2 = \frac{H^2}{4\pi\rho_2}. \tag{50}$$

We assume that $\frac{\rho_{d_1}}{\rho_1} = \frac{\rho_{d_2}}{\rho_2} = \alpha_0$ as the simplifying assumption does not obscure any of the essential features of the problem.

To evaluate the integrals $I_s(s = 1 \ to \ 7)$ in equation (22), we divide the region of integration into three parts $(i) -\infty < z < -\varepsilon$ $(ii) \ \varepsilon < z < \infty$ $(iii) -\varepsilon < z < \varepsilon$ and then pass it over to the limit $\varepsilon \to 0$. On substituting their values in equation (22), we obtain the following dispersion relation between h and k,

$$n^2 - gk(\alpha_2 - \alpha_1) + k^2 V_A^2 + \frac{\alpha_0 v_c}{n+v_c}n^2(\alpha_1 + \alpha_2) + \frac{g}{2}v^2k^4n^2\left\{\frac{\alpha_1}{n^2\left[1 + \frac{\alpha_0 v_c}{n+v_c}\right] + k^2 V_1^2} + \frac{\alpha_2}{n^2\left[1 + \frac{\alpha_0 v_c}{n+v_c}\right] + k^2 V_2^2}\right\} = 0, \tag{51}$$

where

$$V_A = \left\{\frac{H^2}{2\pi(\rho_1 + \rho_2)}\right\}^{1/2} \tag{52}$$

P. Kumar, H. Mohan

can be termed as mean Alfven velocity and

$$\alpha_{1,2} = \frac{\rho_{1,2}}{\rho_1 + \rho_2}.$$ (53)

Letting

$$n = \frac{g}{V_A} n^*, \qquad k = \frac{g}{V_A^2} k^*$$

and omitting the asterisks for simplicity, so that the equation (51) takes the following dimensionless form

$$A_9 n^9 + A_8 n^8 + A_7 n^7 + A_6 n^6 + A_5 n^5 + A_4 n^4 + A_3 n^3 + A_2 n^2 + A_1 n + A_0 = 0,$$ (54)

$$A_9 = 4, \quad A_8 = 12A, A_7 = 4A^2 + \frac{2k^2 B}{\alpha_1 + \alpha_2} + 4\{k^2 - k(\alpha_2 - \alpha_1)\} + 2Lk^4 B,$$

$$A_6 = 2k^2 B \left\{ \frac{1}{\alpha_1 \alpha_2} + Lk^2 \right\}(A + v_c') + 4A^3 + \frac{2k^2 AB}{\alpha_1 \alpha_2} + (8A + 4v_c')\{k^2 - k(\alpha_2 - \alpha_1)\},$$

$$A_5 = \frac{2ABk^2}{\alpha_1 \alpha_2}(A + 2v_c') + \frac{k^4}{\alpha_1 \alpha_2} + 2Lk^4\left(k^2 + Bv_c'^2\right) + \left(4A^2 + \frac{2k^2 B}{\alpha_1 \alpha_2} + 8Av_c'\right)\{k^2 - k(\alpha_2 - \alpha_1)\},$$

$$A_4 = \frac{k^4}{\alpha_1 \alpha_2}(A + 2v_c') + 2Ak^2 v_c'\left(\frac{AB}{\alpha_1 \alpha_2} + Lk^2 v_c' B + 3Lk^4\right) + \left\{\frac{2Bk^2}{\alpha_1 \alpha_2}(A + 2v_c') + 4A^2 v_c'\right\}\{k^2 - k(\alpha_2 - \alpha_1)\},$$

$$A_3 = \frac{k^4 v_c'}{\alpha_1 \alpha_2}(1 + 2A) + 6Lk^6 v_c'^2 + \left\{\frac{2Bk^2 v_c'}{\alpha_1 \alpha_2}(2A + v_c') + \frac{k^4}{\alpha_1 \alpha_2}\right\}\{k^2 - k(\alpha_2 - \alpha_1)\},$$

$$A_2 = \frac{k^4 v_c' A}{\alpha_1 \alpha_2} + 2Lk^6 v_c'^3 + \frac{k^4 v_c'}{\alpha_1 \alpha_2}(3 + 2ABv_c')\{k^2 - k(\alpha_2 - \alpha_1)\},$$

$$A_1 = \frac{k^4 v_c'}{\alpha_1 \alpha_2}(1 + 2v_c')\{k^2 - k(\alpha_2 - \alpha_1)\},$$

$$A_0 = \frac{k^4 v_c'^2}{\alpha_1 \alpha_2}\{k^2 - k(\alpha_2 - \alpha_1)\},$$

$$A = (1 + \alpha_0)v_c', \quad B = \alpha_1 + \alpha_2, \quad v_c' = v_c \frac{V_A}{g},$$ (55)

and

$$L = \frac{v^2 g^2}{V_A^6}$$

is a non-dimensional number measuring the relative importance of FLR effects and magnetic field.

For the potentially stable configuration $(\alpha_2 < \alpha_1)$, all the coefficients of equation (54) are positive, if

$$k > k^*,$$ (56)

where

$$k^* = \alpha_2 - \alpha_1.$$ (57)

So no positive real root or complex root with negative real part exists. **Therefore, the medium is stable even in the presence of collisions for disturbances of all wave numbers as it is if there are none.**

For the potentially unstable configuration $(\alpha_2 > \alpha_1)$, the absolute term in equation (54) is negative, if

$$0 < k < k^*.$$ (58)

ON THE STABILITY OF A PARTIALLY IONIZED PLASMA

Therefore (54) possesses at least one real root which is positive leading to an instability of the configuration even if there are collisions with dust particles.

Also we see that k^* is independent of *L*, a measure of FLR effect. Hence we conclude that for longitudinal perturbations, the stability criterion is independent of magnetic viscosity.

REFERENCES

[1] S. Chandrasekhar, *Hydrodynamic and Hydromagnetic Stability*, UK: Clarendon Press, Oxford, 1981.

[2] R.C. Sharma, and K.N. Sharma, "Finite Larmor radius effects on thermosolutal instability of a plasma," *Phys. Fluids,* vol. 24, pp. 2242-2244, 1981.

[3] R.C. Sharma, and N. Rani, "Finite Larmor radius and compressibility effects on thermosolutal instability of a plasma," *Z. Naturforsch.*, vol. 41A, pp. 724-728, 1986.

[4] R.C. Sharma, and K. Prakash, "Thermal instability in plasma with finite Larmor radius," *Z. Naturforsch.*, vol. 30A, pp. 461-465, 1975.

[5] P.D. Ariel, "Effect of finite Larmor radius on the gravitational instability of a conducting plasma layer of finite-thickness surrounded by a non-conducting matter," *Astrophys. Space Sci.*, vol. 141, pp. 141-149, 1988.

[6] P.D. Ariel, "Rayleigh-Taylor instability of a plasma with finite ion Larmor radius effects," *Astrophys. Space Sci.*, vol. 196, pp. 153-166, 1992.

[7] B. Stromgren, "The physical state of interstellar hydrogen," *Astrophys. J.*, vol. 89, pp. 526-528, 1939.

[8] H. Alfven, *On the Origin of the Solar System*, Oxford: Oxford University Press, 1954.

[9] J.H. Piddington, "Electromagnetic field equation for a moving medium with hall conductivity," *Mon. Not. R. Astron. Soc.*, vol. 114, pp. 638-650, 1954.

[10] B. Lehnert, "Plasma physics on cosmical and laboratory scale," *Suppl. Nuovo Cimento*, vol. 13, pp. 59-62, 1959.

[11] B. Lehnert, R. Inst. Technol. Stockholm Rep. Nos. TRITAEPP-70-05.06, *Proceedings of the V European Conference on Controlled Fusion and Plasma Physics*, Grenoble, France, August 21-25, 1972.

[12] H.K. Hans, "Larmor radius and collisional effects on the combined Taylor and Kelvin instabilities in a composite medium," *Nucl. Fusion*, vol. 8, pp. 89-92, 1968.

[13] P.K. Bhatia, "Collisional effects on the Rayleigh-Taylor instability in a composite medium," *Nucl. Fusion*, vol. 10, pp. 383-386, 1970.

[14] S.S. Rao, and G.I. Kalra, "Hydromagnetic Kelvin instability in the presence of neutral particles," *Canad. J. Phys.*, vol. 45, pp. 2779-2785, 1967.

[15] R.K. Chhajlani, R.K. Sanghvi, and P. Purohit, "Rayleigh-Taylor instability of a stratified magnetized medium in the presence of suspended particles," *Z. Naturforsch.*, vol. 39a, pp. 939-944, 1984.

[16] R.C. Sharma, and Sunil, "Rayleigh-Taylor instability of a partially ionized plasma in a porous medium in presence of a variable magnetic field," *Z. Naturforsch.*, vol. 47a, pp. 1227-1231, 1992.

[17] M.F. El-Sayed, and R.A. Mohamed, "Gravitational instability of rotating viscoelastic partially ionized plasma in the presence of an oblique magnetic field and hall current," *ISRN Mechanical Engng.*, Article ID 597172, 8 pages, 2011.

[18] G.A. Hoshoudy, "Rayleigh-Taylor instability in magnetized plasma," *World J. Mechanics*, vol. 4, pp. 260-272, 2014.

[19] P.K. Sharma, A. Tiwari, R.P. Prajapati, and R.K. Chhajlani, "Rayleigh-Taylor instability in dusty magnetized fluids with surface tension flowing through porous medium," *Thermal Sci.*, vol. 20, pp. 119-130, 2016.

A COMPARISON OF WEIBULL AND RAYLEIGH DISTRIBUTION FUNCTIONS WITH MOMENT METHOD: A CASE STUDY OF OSMANİYE REGION IN TURKEY

Yusuf Alper KAPLAN[1,*] ID, Gülizar Gizem ÜNALDI[2] ID

[1, 2] Osmaniye Korkut Ata University, Department of Energy Systems Engineering, Osmaniye, Turkey

ABSTRACT

In this study, wind energy potential of Osmaniye region is assessed statistically by using the hourly wind speed data of Turkish State Meteorological Service between 2009 and 2013. This study introduced the evaluation of Weibull Distribution Function and Rayleigh Distribution Function for Osmaniye Region. Weibull function is utilized for the situations such as there exist no information about wind speed distribution measurement or frequency distribution. Moment Method is used to calculate the Weibull and Rayleigh parameters. Moment Method, Weibull and Rayleigh Distribution Functions are explained in detail in this paper. Additionally, the Relative Percentage Error (RPE) statistical test is used to compare the efficiency of these distribution functions. The calculated power density of all used distribution function is a major key issue for suitability of wind energy. The evaluation of parameters and wind power distribution have a crucial role in producing electricity from wind power. The calculated power densities of all used distribution functions were compared with wind power density derived from measured wind data. This paper reveals the effectiveness of Weibull and Rayleigh Distribution Functions by using Moment Method for Osmaniye region of Turkey.

Keywords: Wind Energy, Weibull Distribution, Rayleigh Distribution, Moment Method.

1. INTRODUCTION

Nowadays, the need of energy has been increasing day by day with the population growth and the advancements of technology [1]. It can be said that energy is consumed rapidly globally and as a result of this consumption, the energy demand increases day by day. Hence, the search of new energy resources becomes vital for the entire world. Energy is the most significant factor which affects economic structure of a country. As is known, energy is seen as not only the internal dynamics of the countries but also a strategic case which affects international relations, including political as well as military conflicts. Energy is also a primary element of economic and social development in the world [2].

The world has begun to focus on resources that will cause less harm to the environment and to the people in order to satisfy the energy need that cannot be prevented and these sources are called as sustainable energy resources. It is explained that the use of renewable energy sources which are environmentally sensitive, do not cause global warming and climate change are friendly to the world and significantly reduce foreign dependency in the economy. The utilization of these renewable energy resources should be increased instead of the conventional energy which are used in our contemporary life to fulfill energy demand. One of the most common and useful renewable energy resource can be thought as wind power.

Wind energy has been used in irrigation, wheat-grinding, vessels and many other fields because it is an environment-friendly future energy resource. Furthermore, wind energy is used for providing the energy requirement that will be the most important problem of the future world. Currently, wind energy is seen as a positive alternative to fossil fuels and also a way to assist the expansion of local economies in future. The world will use renewable energy instead of using fossil fuels in order to satisfy the demands of the world's energy [3], [4].

The wind power density is an important indicator to determine the potential of wind resources and to describe the amount of wind energy at various wind speed values in a particular location. The knowledge of wind power density is also useful to evaluate the performance of wind turbines and nominate the optimum wind turbines. Wind power density resembles the level of accessible energy at the site which can be converted to electricity by using wind turbines. There are two approaches to calculate wind power density. In the first approach which is more accurate, the wind power density is computed based on measured wind speed data. However, as an alternative method, the wind power density can also be calculated using a proper distribution function.

Among several probability distribution functions suggested in the literature for different applications of wind energy, the Weibull function is unquestionably one of the most popular and broadly used statistical distributions. The main merits of the

Y.A. Kaplan, G.G. Ünaldı

Weibull function have been explained properly in Section 3.1. Furthermore, it should be mentioned that simplicity, flexibility, adaptability and favourable capability to fit with wind data are among the major advantages of this function. Therefore, Weibull distribution function is adopted in this study for wind power density calculation [5].

Kantar and Usta [6] analyzed the use of the minimum cross entropy principle in the estimation of wind speed distribution and wind power density functions. Moreover, they compared the Weibull PDF (probability density function) with the MinxEnt (minimum cross-entropy principle) PDFs. Akdag and Dinler [7] reviewed different methods, i.e. the graphical, maximum likelihood, moment methods and energy pattern method. Bilgili and Sahin [8] investigated wind energy density in the southern and southwestern region of Turkey by using the Weibull and Rayleigh probability density functions. Rocha et al. [9] deal with the evaluation and comparison of different numerical methods for the assessment of efficiency in determining the parameters for the Weibull distribution function, using wind speed data collected in Camocim and Paracuru cities. Freitas et al. [10] introduced a new approach for the analyzing of numerical methods used in calculating the Weibull distribution parameters for the prediction of wind energy source. Chang [11] reviewed the six kinds of numerical methods commonly used for estimating Weibull parameters. Bilir et al. [12] collected wind data for a one-year period between June 2012 and June 2013. Wind speed data, collected for two different heights (20 m and 30 m) from a measurement station installed in Atılım University campus area (Ankara, Turkey), were recorded using a data logger as one minute average values. They determined shape (k) and scale (c) parameter of Weibull using five different methods. Bidaoui et al. aim to evaluate and discuss the energy wind potential of five major cities in Northern Morocco. The theoretical analysis is based on stochastic models of Weibull and Rayleigh using Probability Density Function approach. Various statistical indicators such as the determination coefficient (R^2), Chi square error (χ^2), root mean square error (RMSE) and mean bias error (MBE) are considered. Then, a numerical simulation of the potential electrical power is carried out using the Enercon E103/2350 wind turbine model. Consequently, the results show that Weibull is more accurate than Rayleigh, especially for Tetuan and Al-Hoceima cities [13]. Azhar et al. have selected four sites of coastal region of Balochistan (Gwadar, Pasni, Jiwani and Ormara) and taken data for these selected sites from Pakistan Metrological Department for a period of five years (2010–2014) and they have done the statistical analysis of wind data by Weibull and Rayleigh probability distribution. Weibull and Rayleigh distribution functions have been derived from the available wind data, its parameters are estimated. The annual cycle of Weibull functions is fitted on yearly basis; it is found that the Weibull distribution that is fitting to the measured yearly probability distributions is better and suitable than the Rayleigh distribution for the five-year period (2010–2014) [14]. Sumair et al. purpose that to estimate wind potential using Normal probability density function. A comparison of five probability distributions namely Normal, Gamma, Chi-Squared, Weibull, and Rayleigh was done using three performance evaluation criteria. Four years (2015–2018) hourly wind data at 50 m height at five stations near the coastline of Pakistan was used. It was found that normal distribution gives the best fit at each of these stations and against each evaluation criterion followed by Weibull distribution while Rayleigh distribution gives the poorest fit [15]. Akpınar analyzed the wind energy potential of the Sinop region by using the Turkish State Meteorological Station's hourly wind speed data between the years of 2005-2014. The two- parameter Weibull and one-parameter Rayleigh probability distribution functions were used to determine the wind energy potential of the region. The probability distribution functions were derived from the cumulative function and used to calculate the mean wind speed and the variance of the actual data. In conclusion, The Weibull distribution function was found to be more appropriate than the Rayleigh distribution function [16].

This study aims to determine the wind energy potential in Osmaniye by using Weibull and Rayleigh Distribution Functions. Five-year data of the wind speed which is measured at 10-meter height from the General Directorate of State Meteorology is used to evaluate the wind energy of region. Based on the hourly-measured wind speed data, the convenient of Weibull and Rayleigh Distribution Function with measured real data statistically analyzed for the region. Although the data used in the study are 2009-2013, it is a current study within the scope of calculating wind power densities of the Weibull Distribution Function and Rayleigh Distribution Functions. By comparing the accuracy of the distribution functions, it makes possible to guide future studies. In addition to the purpose of this study is to reveal the comparison and success between Weibull and Rayleigh Distribution Functions for evaluation of wind energy in Osmaniye region.

2. WIND ENERGY POTENTIAL

The industrial growth of any country depends on creating a balance between energy production and its consumption. The production of energy depends on the availability of renewable and non-renewable energy resources. Non-renewable energy resources are in a continuous state of depletion and their scarcity is much felt in countries which are less developed. Furthermore, the adverse effects of fossil-fuel consumption for the energy production results in environmental deterioration. Therefore, the usage of renewable energy resources not only helps in reducing the fossil-fuel consumption but also reduces the green-house effect. The renewable energy resources are constantly replenished, naturally means sustainable and eco-friendly energy sources are available to humanity. This makes them one of the widely studied source of energy that are rapidly replacing conventional energy sources [17]. One of the most popular and having a high preferability resource is wind energy.

A COMPARISON OF WEIBULL AND RAYLEIGH DISTRIBUTION FUNCTIONS WITH MOMENT METHOD: A CASE STUDY OF OSMANİYE REGION IN TURKEY

Wind energy is a clean and emission-free type that has been previously known, developed continuously and can compete with fossil fuels. Since it has no emission, it does not directly generate greenhouse gases and does not contribute directly to global warming. There exist no energy cost and operating costs are low. It is a type of energy that does not depend on other countries and is very efficient in certain regions. These positive features of wind energy are effective for increment of interest in this type of energy. Especially electrical energy production has come to the fore in recent times. Wind power is a low-density energy that abounds in the air. Wind has a natural potential because of its kinetic energy. The part of this potential that can be transformed scientifically and technically to energy is 'wind energy technical potential' whereas the part that can be considered economically is 'wind energy economic potential'. Easily affected by topography, surface structure and obscure obstacles, wind energy is predicted more difficultly than solar energy. Wind turbines produce energy in a certain wind speed range. Thus, the recognition of the wind regime of a region where wind energy systems will be established is of prime importance. The improvements in aircraft propellers and airfoils have triggered the evolution of wind turbines [1], [18].

Figure 1 shows the installed wind power capacity in the world from 2009 to 2019. It is seen from the figure that the total installed capacity of the world was 236.803 GW with more than 20% growth rate in the annual market at the end of 2011. More than 70 GW of new wind power capacity was installed around the world in 2013, bringing the total installed capacity up to 318.919 GW. This represents a year-on-year growth of 29.41 %. At the end of 2014, wind power installed capacity reached 371.336 GW in the world. Finally, the installed wind power in the world reached over approximately 650.8 GW as of the end of 2019 [19].
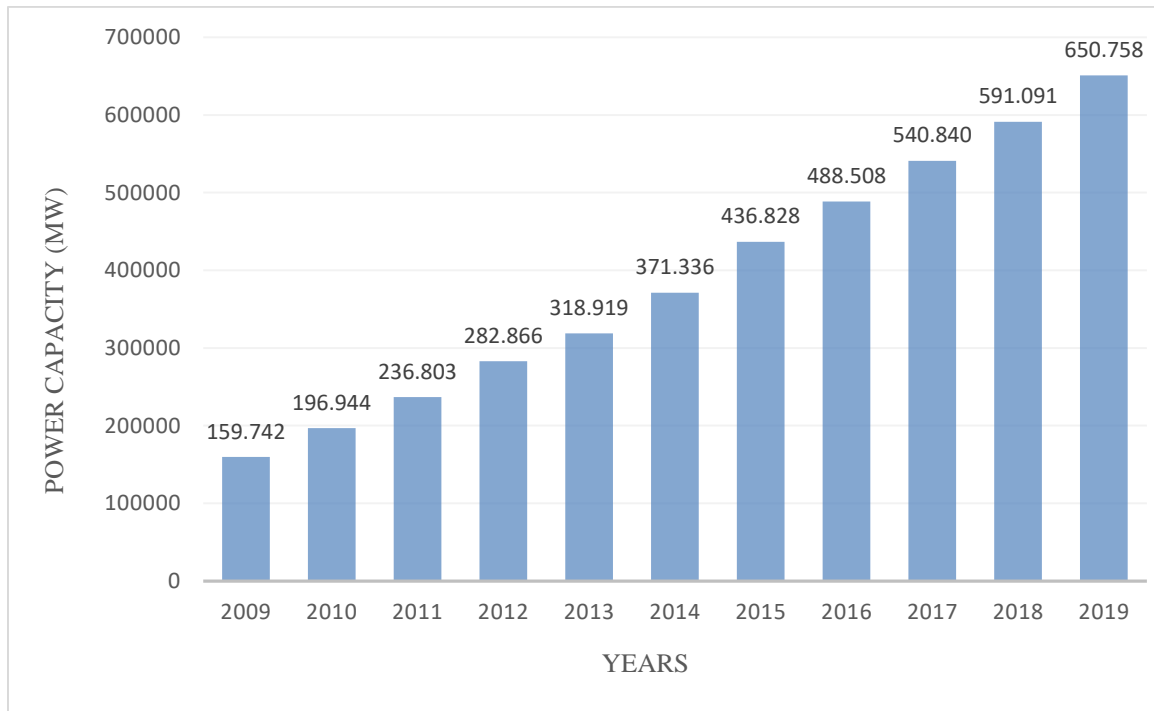

Figure 1. Installed Wind Power Capacity in the World

Turkey is one of the richest countries in terms of wind energy potential because the annual average speed of wind is greater than 7.5 m/s. According to the Turkey wind energy potential atlas prepared in 2007, at least 48.000 MW wind power is available in the regions where the annual wind speed is 7 m/s or over in Turkey [1]. Figure 2 shows that the installed wind power in Turkey year by year. In 2012, wind power capacity is increased with an amount of 506 MW and total installed wind power capacity is 2312 MW. In 2013, 646 MW of new wind power installed and total installed wind power has reached 2958 MW. Turkey added 804 MW of new wind power in 2014 for a total capacity of 3762 MW [20]. Finally, the installed wind power in Turkey reached 8056 MW as of the end of 2019. Turkey's installed capacity has grown by nearly 500 MW per year since 2010 and the national transmission company expects annual installations to reach 1,000 MW per year from 2019 onwards [21], [22].
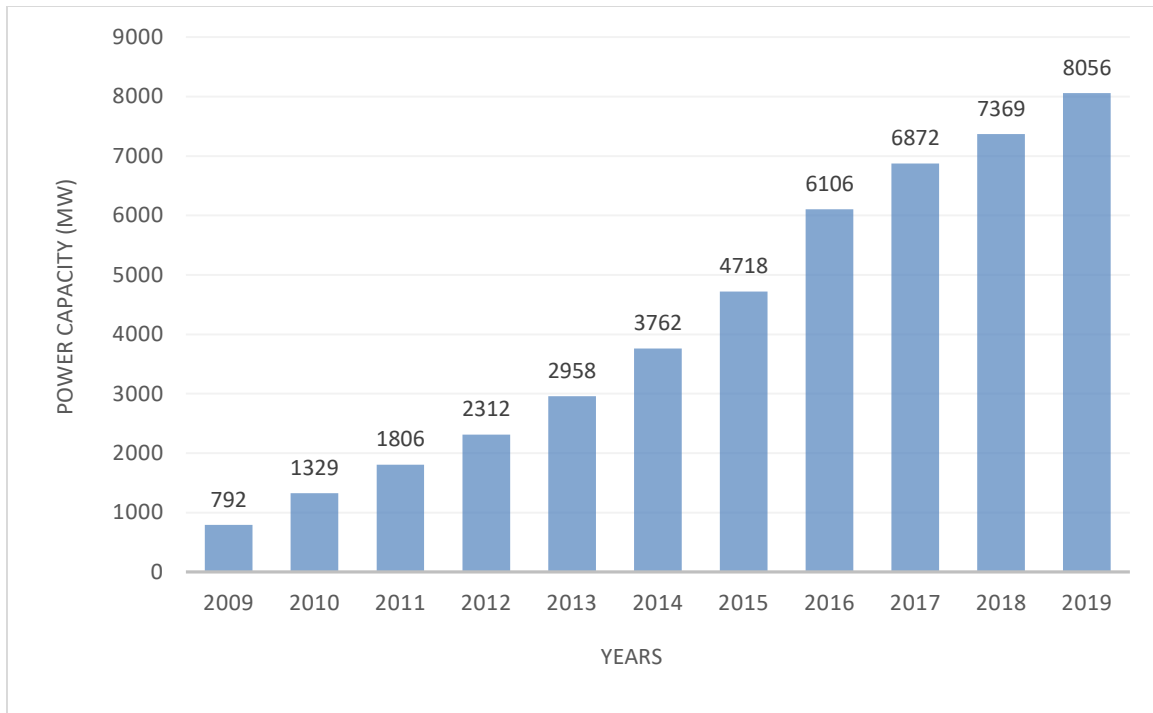
Figure 2. Installed Wind Power Capacity in Turkey

2.1. The wind characteristic of Osmaniye region

Osmaniye is a Turkish province located in southern of Turkey. It is shown in the Figure 3 that Osmaniye is in the Çukurova region of Turkey, the area of Osmaniye Province is 3,767 km² and Osmaniye is at an elevation of 125 meters (410.1 feet). This study aims to determine the wind energy potential in Osmaniye. It is collected the five years data of the wind speed measured at 10-meter height from the General Directorate of State Meteorology. Based on the hourly-measured wind speed data, the wind energy potential of this region has been statistically analyzed by using Weibull and Rayleigh Distribution Functions.
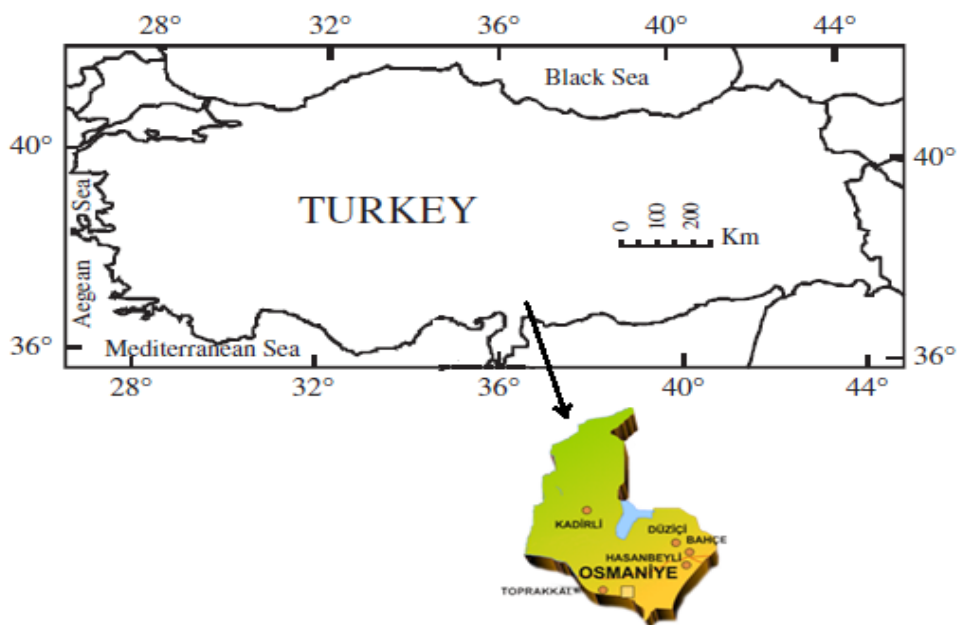

Figure 3. The map of Osmaniye

A COMPARISON OF WEIBULL AND RAYLEIGH DISTRIBUTION FUNCTIONS WITH MOMENT METHOD: A CASE STUDY OF OSMANİYE REGION IN TURKEY

Figure 4 shows the density of wind directions according to wind frequency. The dominant wind direction of Osmaniye region is found by using a five-year wind data.
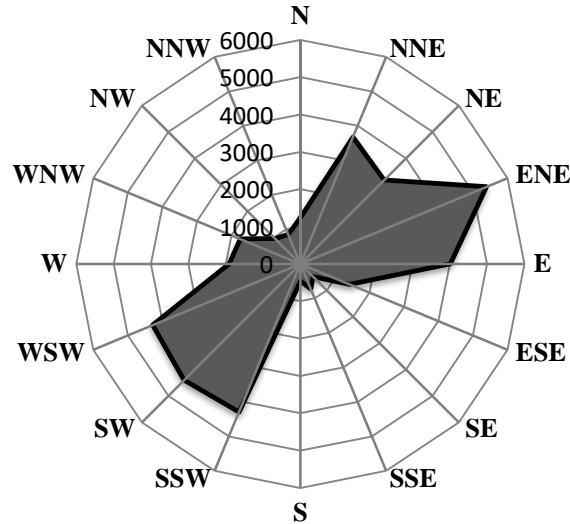

Figure 4: The variation of the wind directions.

3. STATISTICAL ANALYSIS

In practice, there exist various methods to determine the wind energy potential of a region. Wind speed distribution measurement or frequency distribution is used in order to determine the wind potential of a specific region if possible. If not, wind speed distribution can be presented by other analytic distribution functions. Weibull distribution function is one of these functions. Due to its simple and flexible application as well as giving results close to actual data, Weibull distribution is widely accepted in the wind energy analysis [23]. Two-parameter Weibull and Rayleigh distribution functions are the most popular of all. The Rayleigh distribution is less flexible than the Weibull as it is one-parameter. However, the calculation of parameters is easier in the Rayleigh distribution.

3.1.   Weibull distribution function

The Weibull distribution is a distribution first introduced by Waloddi Weibull in 1951 to estimate the lifespan of machines. Today, it is widely used in statistical models in life-time data analysis and engineering. Depending on the values of the format parameter, the Weibull distribution, which also has Rayleigh and exponential distributions in some cases, is widely used in the models to be established for the data set related to failure rates. As it is known, continuous random variables are used to define random events in which the variable can take any value in a certain range. The Weibull distribution is also a continuous and at the same time flexible distribution and provides theoretically suitable solutions in many applications. In life analysis, logarithmic models are generally used instead of parametric models. In this sense, the Weibull distribution is also a logarithmic model.

The Weibull Distribution Function provides a close approximation to the probability laws of many natural phenomena. This function has been used to represent wind speed distributions for application in wind turbines studies for a long time. For more than half a century the Weibull Distribution Function has attracted the attention of statisticians working on theory and methods as well as various fields of statistics [24]. The wind data analysis of a region is prepared by the prediction of the region's potential performance through the pre-measured values. Hourly wind speed and wind direction details are observed in a place and statistical results are calculated for modelling the frequency and probability of the obtained results [8, 25]. First, as is seen in Table 1, the periodical frequency (the blowing number) and probability of wind speed are determined. Average wind speeds are grouped periodically in the second column of Table 1. The third column shows average wind speed for each speed ratio. The blowing number or frequency of each speed ratio is given in the fourth column.

The general expression of the two-parameter Weibull is given by,

Y.A. Kaplan, G.G. Ünaldı

$$p(v) = \left(\frac{k}{c}\right)\left(\frac{v}{c}\right)^{k-1} \exp\left[-\left(\frac{v}{c}\right)^k\right] \tag{2}$$

The cumulative function of wind speed can be attained by computing the integral of the probability density function is given by,

$$P(v) = 1 - \exp\left[-\left(\frac{v}{c}\right)^k\right] \tag{3}$$

Where $p(v)$ is the observed probability density function, $P(v)$ is the cumulative probability density function, shape (k) and scale (c) parameter of Weibull distribution function [26], [27].

Table 1. Periodical frequency and probability of hourly wind speeds

i	v_i (m/s)	v_{avg} (m/s)	f_i	$p(v_i)$	$P(v_i)$
1	0-1	0,5	9637	0,255467	0,255467
2	1-2	1,5	12295	0,325928	0,581396
3	2-3	2,5	5813	0,154097	0,735493
4	3-4	3,5	3141	0,083265	0,818758
5	4-5	4,5	2489	0,065981	0,884739
6	5-6	5,5	2113	0,056014	0,940752
7	6-7	6,5	1189	0,031519	0,972272
8	7-8	7,5	559	0,014819	0,98709
9	8-9	8,5	255	0,00676	0,99385
10	9-10	9,5	103	0,00273	0,99658
11	10-11	10,5	77	0,002041	0,998622
12	11-12	11,5	39	0,001034	0,999655
13	12-13	12,5	9	0,000239	0,999894
14	13-14	13,5	4	0,000106	1

Probability density of each speed ratio is given in following equation,

$$p(v_i) = \frac{f_i}{\sum_{i=1}^{N} f_i} \tag{1}$$

Here, f_i is frequency of occurrence of each speed class and N is number of hours in the period of time considered. $P(v_i)$ is the cumulated probability density which is illustrated in the sixth column of the Table 1.

The two-parameter Weibull distribution function is described for wind speed as follow Eq. (2) and as a cumulative distribution function given by Eq. (3) [26], [28]:

Actual probability density function and cumulative probability distributions derived from the long-term wind speed data of Osmaniye during 2009 to 2013 period are depicted in Figure 5.

A COMPARISON OF WEIBULL AND RAYLEIGH DISTRIBUTION FUNCTIONS WITH MOMENT METHOD: A CASE STUDY OF OSMANİYE REGION IN TURKEY
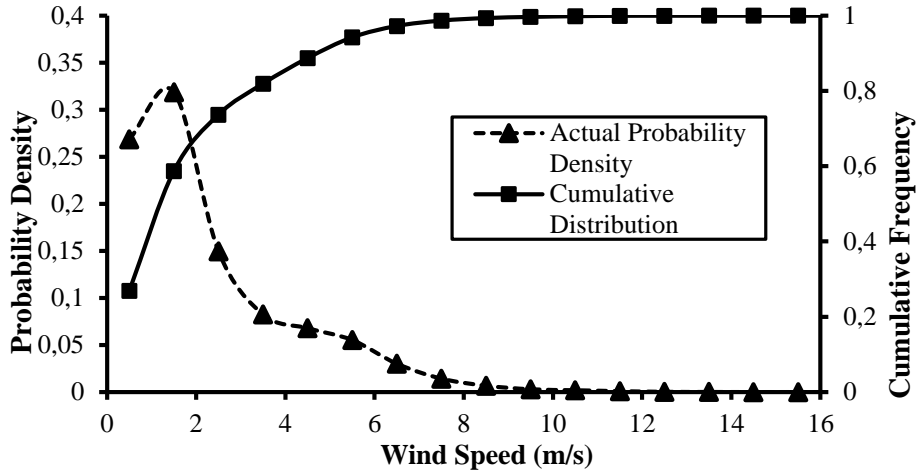

Figure 5: The wind speed probability density and cumulative distribution data of Osmaniye

The average wind speed 'V_m' and wind power density 'P_w' of Weibull Distribution Function can be estimated by the following equations:

$$V_m = c\Gamma\left(1 + \frac{1}{k}\right) \tag{4}$$

$$P_w = \frac{1}{2}\rho c^3 \Gamma\left(1 + \frac{3}{k}\right) \tag{5}$$

Here, Γ shows the gamma function.

$$\Gamma(x) = \int_0^\infty e^{-u} u^{x-1} du \quad \text{and} \quad \Gamma(1+x) = x\Gamma(x) \tag{6}$$

3.2. Rayleigh distribution function

Rayleigh distribution is yet another statistical approach used for determining the wind speed distribution data. Depending on the reason of Rayleigh Distribution Function has single parameter, it behaves less flexible than Weibull Distribution Function; however, its parameters are easier to calculate. Also, it is known that when the average annual wind speed is greater than 4.5 m/s, the wind speed distribution approaches the Rayleigh distribution. In other words, the Rayleigh model is a special and simplified case of the Weibull model. It is obtained when the shape factor c of the Weibull model is assumed to be equal to 2. The probability density and the cumulative distribution functions of the Rayleigh model are given by [29], [30]:

$$f_R(v) = \left(\frac{2v}{c^2}\right) \exp\left\{-\left(\frac{v}{c}\right)^2\right\} \tag{7}$$

The Rayleigh cumulative distribution function is explained as follow:

$$F_R(v) = 1 - \exp\left\{-\left(\frac{v}{c}\right)^2\right\} \tag{8}$$

Average wind speed for the Rayleigh distribution is defined by Eq. (9) and power density by Eq. (10).

$$v_m = c\sqrt{\pi/4} \tag{9}$$

$$P_R = \frac{3}{\pi}\rho v_m^3 \tag{10}$$

Y.A. Kaplan, G.G. Ünaldı

One of the most distinct advantages of the Rayleigh distribution is that the probability density and the cumulative distribution functions could be obtained from the mean value of the wind speed [31]. Figure 6 illustrates the variation of Weibull, Rayleigh and observed wind speed frequencies of Osmaniye region for measured wind data.
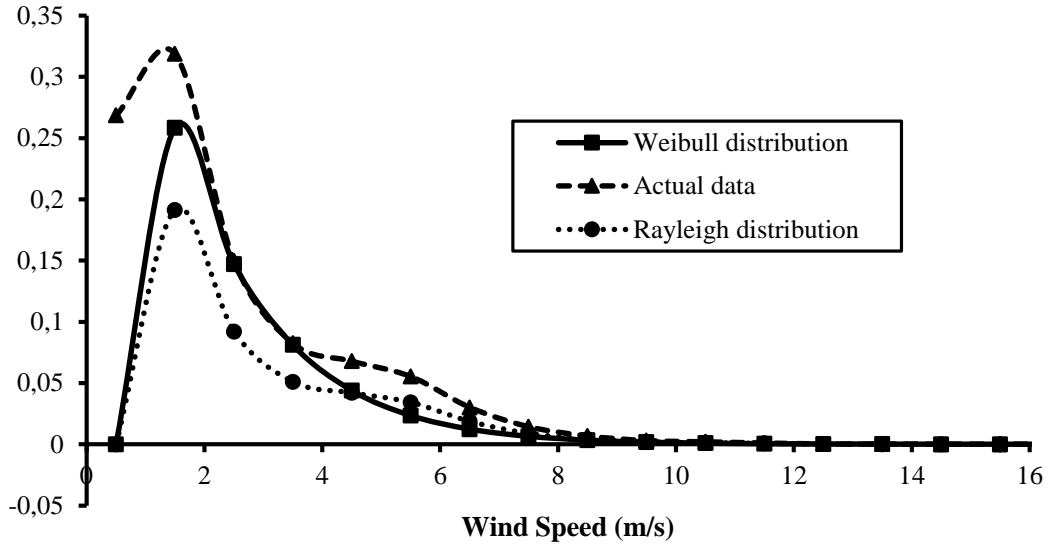

Figure 6: Weibull, Rayleigh and observed wind speed frequencies of Osmaniye

4. DETERMINATION OF WEIBULL PARAMETERS

There exist many different methods to determine the *k* and *c* parameters for used distribution functions. These parameters have a substantial role to calculate the average speed and power densities. In the literature, details on the use and application of four different mathematical methods, which are frequently used for the calculation of Weibull variables are Graphical Method, Most Likelihood Method, Least Squares Method and Moment Method. From all these methods, the Moment Method is used in this study to determine the scale and shape parameters.

4.1. Moment method

Moment method is one of the oldest method is used to determine Weibull distribution parameters. Moment method is a method that data distribution allows to solve the relationship between average and standard deviation values between the shape parameters using numerical methods for determining the scale of 1 to 10 and the shape parameter. Shape and scale parameters can be expressed as in Eq. (11) and Eq. (12) [9], [24].

$$k = \left(\frac{\sigma}{v_m}\right)^{-1,086} \tag{11}$$

Here Γ is Gamma function.

$$c = \frac{Vm}{\Gamma\left(1+\frac{1}{k}\right)} \tag{12}$$

Here, v_i is the measured wind speed σ, shows Standard deviation and v_m is average speed.

$$v_m = \frac{1}{n}\sum_{i=1}^{n} v_i \tag{13}$$

A COMPARISON OF WEIBULL AND RAYLEIGH DISTRIBUTION FUNCTIONS WITH MOMENT METHOD: A CASE STUDY OF OSMANİYE REGION IN TURKEY

$$\sigma = \sqrt{\frac{1}{n} \sum_{i=1}^{n} (Vi - Vm)^2} \qquad (14)$$

5. RESULTS AND DISCUSSION

In this study, two distribution functions are compared that it was compatible with actual data. The long term wind data must be measured in order to determine the wind potential of the selected area. The shape and scale parameters are separately calculated for each year. The Moment Method is used to determine the parameters of distribution functions, the calculated parameters are given in Table 2.

Table 2. Weibull and Rayleigh parameters for Moment Method

Moment Method	Weibull Parameters				Rayleigh Parameters			
	k	c(m/s)	V_M(m/s)	P_W(W/m²)	k	c(m/s)	V_M(m/s)	P_R(W/m²)
2009	1,3180	2,6514	2,4421	29,8923	2,00	2,7556	2,4415	17,0326
2010	1,2270	2,5727	2,4066	32,6371	2,00	2,7156	2,4060	16,3016
2011	1,2961	2,3207	2,1446	20,8568	2,00	2,4200	2,1441	11,5366
2012	1,4147	2,3641	2,1512	18,1422	2,00	2,4274	2,1507	11,6428
2013	1,2290	2,4413	2,2828	27,7674	2,00	2,5759	2,2823	13,9129
2009-2013	1,2656	2,4657	2,2902	26,5242	2,00	2,5841	2,2895	14,0462

The average wind speed 'V_M' and wind power density 'P_M' can be computed by the following equations for real time series data:

$$V_M = \frac{1}{n} \sum_{i=1}^{n} v_i \qquad (15)$$

$$P_M = \frac{1}{2} \rho \overline{V^3} \qquad (16)$$

To determine the efficiency of the used methods and to find the best method of mentioned methods, the Relative Percentage Error (MPE) test can be used. The equation of RPE test is given in following equation [32].

$$RPE = \left[\frac{P_{w,R} - P_M}{P_M} \right] * 100 \qquad (17)$$

The RPE statistical results of all methods for five years are given in Table 3.

Table 3. The RPE statistical results

RPE TEST	V_M(m/s)	P_M(W/m²)	P_W(W/m²)	P_R(W/m²)	RPE (Weibull)	RPE (Rayleigh)
2009	2,44	30,91	29,89	17,03	-3,30	-43,02
2010	2,41	33,12	32,64	16,30	-1,45	-50,06
2011	2,14	21,19	20,86	11,54	-1,56	-44,68
2012	2,15	21,62	18,14	11,64	-16,10	-38,83
2013	2,28	27,46	27,76	13,91	1,092	-49,90
2009-2013	2,29	27,04	26,52	14,05	-1,92	-47,02

According to the obtained results Weibull Distribution Function gave more accurate results than the Rayleigh Distribution Function. Based on five-year measured wind data it has been observed that the Weibull Distribution Function result is highly close to the actual data. It can be said that Weibull Distribution Function presented acceptable results [32]. It is observed that the Rayleigh Distribution Function fails to generate a result parallel to the actual data.

Y.A. Kaplan, G.G. Ünaldı

The utilization of Weibull and Rayleigh distributions in the expression of probability distributions of wind speeds is frequently used in the literature as an approach proved to be successful. It can be said that there exist high preferability for both functions according to their easiness to calculate and suitableness for wind evaluating shape and scale parameters. However, it is clearly seen that Weibull Distribution Function resulted more accurately than Rayleigh Distribution Function. In this study, by using the available wind data the reliability and the quality of wind speed for Osmaniye region are evaluated and the value of Weibull and Rayleigh parameters 'k' and 'c' were determined by using Moment Method. In this work, Weibull Distribution Function and Rayleigh Distribution Function are compared for wind data analysis of Osmaniye region. This study is a preliminary study for the determination of wind potential before making investment in wind energy for this region. The coherence of wind speeds with the Weibull and Rayleigh distribution functions have been examined by using wind speed data for the year 2009 to 2013. For all years the wind power density derived from using measured actual wind data were compared with wind power densities estimated from Weibull Distribution Function and the wind power density estimated from Rayleigh Distribution Function. According to obtained wind power densities, it was found that the closest result was obtained by Weibull Distribution Function. Moreover, it can be said that the Rayleigh Distribution Function is not suitable for estimating the wind power of this region. The wind power estimating issue is considered today one of the most important topics of renewable energy research. In future studies, the scope of this study can be expanded and detailed with using other numerical methods to determine wind energy potential of this region.

6. CONCLUSION

In aim to accomplish the purpose of this study, the data set which were used are hourly wind speed data of Osmaniye region between 2009 and 2013. This study introduced the evaluation of Weibull and Rayleigh Distribution Functions. Additionally, the method that is used for parameters in order to evaluate Weibull Distribution Function and Rayleigh Distribution Function is Moment Method. On the purpose of compare the efficiency of Weibull Distribution Function and Rayleigh Distribution Function, a statistical analysis is used called Relative Percentage Error. The calculation of parameters and wind power distribution are the cornerstones of the wind power producing process. Consequently, according to the Figure 6 and the results of RPE test, it is clearly observed that Weibull Distribution Function fits more accurately to actual data than Rayleigh Distribution Function. Furthermore, when Table 3 is analysed, it is concluded that the average of 2009-2013 RPE value is considerably smaller for Weibull Distribution Function in comparison with Rayleigh Distribution Function.

REFERENCES

[1] Kaplan Y.A., "Overview of Wind Energy in the World and Assessment of Current Wind Energy Policies in Turkey", Renewable and Sustainable Energy Reviews, 43 C, pp. 562-568, (2015)

[2] Kaplan Y.A., San I., "Current Situation of Wind Energy in the World and Turkey, Green Energy Conference-VI" (IGEC-VI), Eskisehir, Turkey, (2011)

[3] Çapika M, Yılmaz AO., Çavusoglu I., "Present situation and potential role of renewable energy in Turkey", Renewable Energy; 46, pp: 1-13, (2012)

[4] Gabbasa M, Sopian K, Yaakob Z, Zonooz M, Fudholi A, Asim N., "Review of the energy supply status for sustainable development in the Organization of Islamic Conference" Renewable and Sustainable Energy Reviews;28 pp:18–28, (2013)

[5] Mohammadi, Kasra, et al. Assessing different parameters estimation methods of Weibull distribution to compute wind power density. *Energy Conversion and Management*, 2016, 108: 322-335.

[6] Kantar Y.M., Usta I., "Analysis of wind speed distributions: wind distribution function derived from minimum cross entropy principles as better alternative to Weibull function", Energy Convers Manage, 49, pp. 962–973 (2008)

[7] Akdağ S.A., Dinler A., "A new method to estimate Weibull parameters for wind energy applications", Energy Convers Manag, 50, pp 1761-1766 (2009)

[8] Bilgili M. ve Şahin B., "The finding of weibull parameters at the determination of Wind Power density", New and Renewable Energy / Energy Management Symposium, Kayseri, 229-234, (2005)

[9] Rocha P. A. C. R. Sousa R. C. D. Andrade C. F.D, and Silva M. E. V. D. "Comparison of seven numerical methods for determining Weibull parameters for wind energy generation in the northeast region of Brazil", Applied Energy, 89, pp 395–400, (2012)

[10] Freitas de Andrade C., Maia Neto H. F., Costa Rocha P. A., Vieira da Silva M. E., "An efficiency comparison of numerical methods for determining Weibull parameters for wind energy applications: A new approach applied to the northeast region of Brazil", Energy Convers Manage, 86 (10) pp. 801–808 (2014)

A COMPARISON OF WEIBULL AND RAYLEIGH DISTRIBUTION FUNCTIONS WITH MOMENT METHOD: A CASE STUDY OF OSMANİYE REGION IN TURKEY

[11] Chang T. P., "Performance comparison of six numerical methods in estimating Weibull parameters for wind energy application". Appl Energy, 88, pp. 272–282 (2011)

[12] Bilir L. İmir M. Devrim Y. Albostan A. "Seasonal and yearly wind speed distribution and wind power density analysis based on Weibull distribution function" , IntJ.Hydrogen Energy http://dx.doi.org/10.1016/j.ijhydene.2015.04.140, (2015)

[13] Bidaoui, Hicham, et al. Wind speed data analysis using Weibull and Rayleigh distribution functions, case study: five cities northern Morocco. *Procedia Manufacturing*, 2019, 32: 786-793.

[14] Azhar, Noreen, et al. Wind Data Analysis of Coastal Region of Balochistan (Pakistan) by Weibull and Rayleigh Method. *Indian Journal of Science and Technology*, 2019, 12: 26.

[15] Sumair, Muhammad, et al. Application of five continuous distributions and evaluation of wind potential at five stations using normal distribution. *Energy Exploration & Exploitation*, 2020, 0144598720939373.

[16] Akpinar, Ebru Kavak. Statistical Analysis of Wind Speed Distribution With Sinop-Turkey Application. *Journal of Thermal Engineering*, 2019, 5.4: 277-292.

[17] Shoaib, Muhammad, et al. Assessment of wind energy potential using wind energy conversion system. *Journal of cleaner production*, 2019, 216: 346-360.

[18] Maheshwari M., Chandrasekaran RS., Babu D., "Optimization of Electrical Power Using Solar and Wind Energy Systems", Proceedings of7'h International Conference on Intelligent Systems and Control (ISCO 2013), (2012)

[19] GWEC (Global Wind Energy Council), Global Wınd 2019 Report

[20] EWEA (European Wind Energy Association), Wind in power 2010 European statistics, February 2011

[21] Simsek HA, Simsek N., "Recent incentives for renewable energy in Turkey", Energy Policy;63, pp: 521–530 (2013)

[22] Baris K, Kucukali S., "Availibility of renewable energy sources in Turkey: Current situation, potential, government policies and the EU perspective", Energy Policy, 42, pp: 377–391, (2012)

[23] Caglar, Ahmet. Investigation of Wind Characteristics for Antalya Region by Using Weibull Distribution. *Cumhuriyet Science Journal*, 2017, 38.4: 156-164.

[24] Azad A.K., Rasul M.G., Alam M.M., Uddin S.M.A., Mondal S.K., "Analysis of Wind Energy Conversion System Using Weibull Distribution", Procedia Engineering., 90, pp. 725–732, (2014)

[25] Kım.J.-Yum.B., "Selection between Weibull and Lognormal Distributions: A Comparative Simulation Study" Computational Statistics&Data Analysis, 53(2), pp: 477-485, (2008)

[26] Kose R., Arif M.O., Erbas O., Tugcu A.., "The analysis of wind data and wind energy potential in Kutahya, Turkey", Renewable and Sustainable Energy Reviews, 8, pp. 277–288, (2004)

[27] Yıldırım U., Gazibey Y., Güngör A., "Wind Energy Potential of Niğde", Journal of Niğde University, 1(2), pp: 37-47, (2012)

[28] Ahmet Shata SA, Hanitsch R. "Evaluation of wind energy potential and electricity generation on the coast of Mediterranean Sea in Egypt". Renew Energy, 31, pp: 1183–202, (2006)

[29] Gokcek M., Bayulken A., Bekdemir S., "Investigation of wind characteristics and wind energy potential in Kirklareli, Turkey", Renewable Energy, 32, pp: 1739–1752, (2007)

[30] Zhou W, Yang H, Fang Z. "Wind power potential and characteristics analysis of the Pearl River Delta Region." Renew Energy, 31, pp: 739–53, (2006)

[31] Celik A.N., "A statistical analysis of wind power density based on the Weibull and Rayleigh models at southern region of Turkey", Renewable Energy, 29, pp. 593–604, (2003)

[32] Sabzpooshani M, Mohammadi K. "Establishing new empirical models for predicting monthly mean horizontal diffuse solar radiation in city of Isfahan, Iran" Energy; 69(5), pp 71–77 (2014)